Instability Wave Models of Turbulent Jets from Round and Serrated Nozzles

Thesis by

Kristján Guðmundsson

In Partial Fulfillment of the Requirements

for the Degree of

Doctor of Philosophy

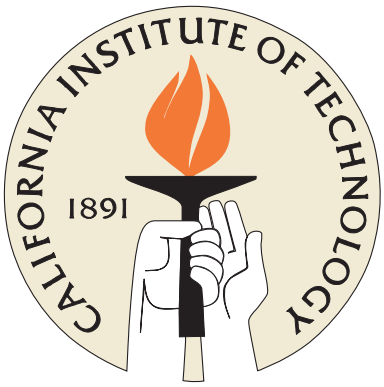

California Institute of Technology

Pasadena, California

2010

(Defended November 17, 2009)

Ég tileinka þessa ritgerð mínum ástkæru foreldrum, Eygló and Guðmundi.

Acknowledgments

What a ride! My time at Caltech has been nothing short of amazing. First, I would like to convey my gratitude to my advisor, Prof. Tim Colonius. Tim has a tremendous intuition when it comes to computational physics. His ways of thinking was and remains a source of inspiration in my own work. I can only hope that some of these traits rubbed off on me!

I would also like to thank the members of my Ph.D. committee: Profs. Tim Colonius (chair), Fazle Hussain, Anthony Leonard, and Joe Shepherd. Fazle deserves a special mention for traveling from Houston, Texas, specifically to attend my thesis defense! But this is not all: Fazle spent a lot of time at Caltech during 2009 and we met frequently to discuss the work presented in this thesis. His physical insights are uncanny and I am particularly grateful to him for asking me tough questions, thereby pushing me to think in new ways about my work.

I would also like to express my gratitude to my lab-mates: Eric Johnsen, Guillaume Bres, Kunihiko Taira, Jeff Krimmel, Jennifer Franck, Won Tae Joe, Keita Ando and Vedran Coralic. I will cherish the many nights and weekends we spent in the lab together. In particular I'll remember fondly the nights Sam and I spent discussing physics (drinking), as well as the countless wings Eric and I downed at Guss's in South Pasadena.

During my last year at Caltech, Drs. Arnab Samanta and Daniel Fuster joined the lab as postdocs. We've had many good times in the line at Ernies! I'd especially like to thank Arnab for many inspiring discussions on fluid mechanics and various other topics of lighter weight.

I would like to mention some of the friends I met during my stay at Caltech, particularly during my first years: Hannes, Angel, Vala, Nick, Jerrod, Xiao, Lisa, and Óliver. The fun we had. And of course the latest additions to Caltech's repertoire of Icelanders: Arnar Björn and Benjamin.

I cannot give sufficient appreciation to my parents, Eygló Kristjánsdóttir and Guðmundur Óskar Emilsson. Without their encouragement and support I'm not sure I'd have finished my degree. In fact, I'm not sure I'd even have finished high-school, as I had planned to drop out to "work for a year." This move was swiftly blocked by mom and dad.

Lastly and most importantly I would like to thank my love Ciji for her endless support and patience throughout the whole process. She's made countless sacrifices so that I'd be able to meet my goals at Caltech and for that I'll be ever grateful.

Abstract

In this thesis we study pressure fluctuations associated with large-scale coherent structures in turbulent round and serrated jets. Linear disturbances to the turbulent mean flow of the round jet are modeled via linear stability analysis and the Parabolized Stability Equations (PSE). We show that PSE provides better agreement with near-field microphone-array data at low frequencies than previous models based on linear stability theory. We examine the extent to which microphone data is contaminated by fluctuations uncorrelated with large-scale structures. By filtering out the uncorrelated fluctuations, via the proper orthogonal decomposition (POD), better agreement between data and theory is obtained. We next extend the linear stability analysis of round jets to include the effects of azimuthal inhomogeneities of serrated jets. We solve the resulting system of equations and find new modes, associated with the streamwise vorticity of the serrated-jet mean flow. All unstable modes of the serrated jet are stabilized, potentially explaining the noise reduction achieved by such jets. We also compare these predictions to POD-filtered microphone measurements, generally finding good agreement.

Contents

List of Figures

List of Tables

Nomenclature

α	Streamwise wavenumber (complex valued in the spatial framework)
γ	Ratio of specific heats
$\mathbf{Q}$	Vector of heat fluxes
$\mathbf{q}$	Vector of field variables
$\mathbf{V}$	Vector of viscous terms
ω	Angular frequency (complex valued in the temporal framework)
Φ	Viscous dissipation function (scalar)
ϕ	Angle measured from downstream direction (see figures 1.2 and 2.1)
ρ	Density
τ_{ij}	Viscous stress tensor
a	Speed of sound
c_p	Specific heat at constant pressure
D	Nozzle diameter
f	Frequency
m	Azimuthal wavenumber
M_∞	Acoustic Mach number (U_{jet}/a_∞)

N_l	The number of lobes on the serrated jet
N_{ring}	Number of microphone rings
p	Pressure
Pr	Prandtl number ($\mu_\infty c_p/k_\infty$)
r	Radial coordinate
Re	Reynolds number ($U_{jet}D/\nu_{jet}$)
St	Strouhal number (fD/U_{jet})
T	Temperature
t	Time
u_i	Velocity in direction **i**
U_{jet}	Mean streamwise velocity on nozzle centerline
x	Axial coordinate
DNS	Direct Numerical Simulation
LNS	Linearized Navier-Stokes
LST	Linear stability analysis
POD	Proper Orthogonal Decomposition
PSE	Parabolized Stability Equations
SPL	Sound Pressure Level

Subscripts

∞	Ambient conditions
jet	Centerline conditions at nozzle exit

Operators

δ_{ij} Kronecker delta ($\delta_{ij} = 1$ if $i = j$, zero else)

∇ Divergence

∇^2 Laplacian

$\overline{z}$ Time-average of z

z' Fluctuating component of z

z^* Complex conjugate of z

Superscripts

$*$ Dimensional variable (also complex conjugate)

Chapter 1

Introduction

1.1 Motivation

The turbojet engine heralded a new era in commercial and military aviation. Inefficient and noisy compared to today's turbofan engine, the turbojet enabled faster flight than had previously been possible. The increased noise levels fueled interest in noise reduction technologies and research into the jet noise generation and radiation process became increasingly active. This culminated in the birth of a new field, *Aeroacoustics*, widely credited to Sir James Lighthill (Lighthill, 1952).

Great strides have been made in noise reduction both via theory and experiment, the most significant of which has been the advent of the turbofan engine in which a large proportion of the air-flow bypasses the central turbojet, flowing around it inside an outer duct at a much lower speed. This reduces the average exhaust speed required to produce a given thrust, significantly increasing fuel efficiency and retarding noise emission. Other approaches to noise reduction have also been pursued, most of which involve the passive or active manipulation of the thin boundary layer near the nozzle lip. These devices generally alter the jet turbulence such that peak-noise levels (which occur at low-frequencies and aft-angles; see figures 1.1 and 1.2) are lowered. The noise reduction at low frequency is usually accompanied by a slight noise increase, due to heightened near-nozzle turbulence levels, at higher frequencies. This topic is explored further in chapter 4.

Early design for noise reduction was largely an empirical effort. As computing power has increased, the realm of computable (in a reasonable time-frame) processes has gotten larger by leaps

and bounds; simulations now play a vital role in most all design efforts. Direct numerical simulations of realistic jets (*i.e.*, having asymptotically high Reynolds numbers) are challenging if not impossible, even with today's computing resources. As pointed out by Colonius & Lele (2004), aeroacoustic noise prediction is particularly difficult, largely due to wide separations in length scales (of acoustic waves and their sources) as well as in energy, the radiated acoustic energy being a minute fraction of the flow energy. Modeling efforts such as Large Eddy Simulation, intended to capture the most energetic scales, provide promising results (Bodony & Lele, 2005, 2008).

Phenomenological understanding of the jet noise process, allowing more accurate, theory-based modeling assumptions, is crucial to further development in this area. In particular, the radiation of sound by the large-scale coherent structures in shear flows is incompletely understood. To what extent can these structures and their radiation be ascribed to (and predicted by) the Kelvin-Helmholtz instability of the mean flow, particularly for turbulent jets? This is the central question of this thesis. In addition to scientific interest, improved understanding of the behavior and origins of large-scale coherent structures might allow for improved control laws for noise reduction, such as defining a metric for the optimization of a chevron nozzle geometry, or the fast, approximate prediction of noise from coherent turbulence.

1.2 Features of Jet Noise

Figure 1.1 illustrates features of jet engine exhaust relevant to sound generation and propagation. For simplicity we ignore the effects of co-flow; the figure shows a turbojet, rather than the turbofan commonly used in practice. The turbofan has an additional shear layer shrouding the inner shear layer. The outer shear layer refracts sound generated in the core but also represents an additional source of sound. These additional effects are qualitatively similar to the core processes on which we focus henceforth. We also assume the absence of shock-associated noise, which can be important at supersonic conditions.

Aerodynamic generation of sound refers to that generated by the unsteady motions within the flow. Such fluctuations are found throughout the airstream exiting an engine. The boundary layer in-

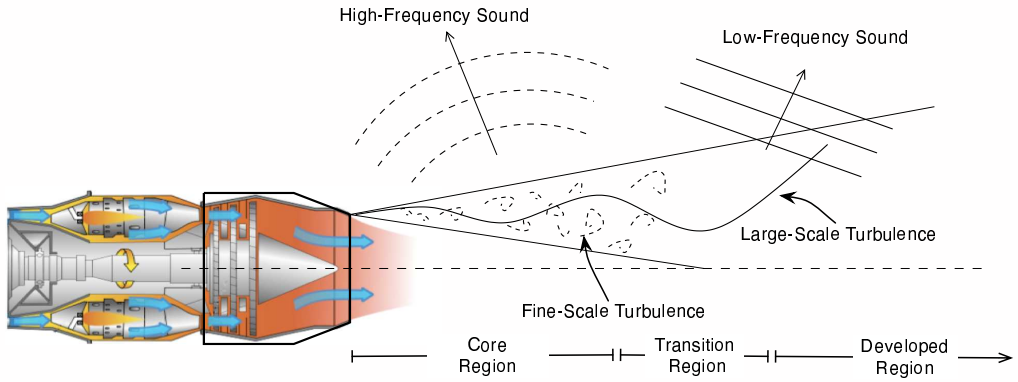

Figure 1.1: A qualitative illustration of turbojet exhaust and sound-related processes. The diverging lines represent the edges of the jet shear layer.

side the nozzle contains unstable motions (instabilities) of viscous origin, while the flow away from the wall contains entropic (hot spots) and vortical fluctuations generated during combustion and passage through the turbine stages. As the flow exits the nozzle, the boundary layer relaxes to an axisymmetric shear layer, susceptible to Kelvin-Helmholtz instability. Such instabilities are exited by the turbulent fluctuations present at the exit and grow into large-scale turbulence structures, illustrated in figure 1.1. These structures radiate primarily in the downstream direction and are responsible for the peak levels of sound (Mollo-Christensen, 1967; Moore, 1977; Troutt & McLaughlin, 1982). At the same time, fine-scale turbulent fluctuations grow in intensity and radiate sound. Their radiation is less directive than that from large-scale structures and peaks at a higher frequency. Figure 1.2 illustrates pressure measurements taken along an arc in the far-field of a $M_\infty = U_{jet}/a_\infty = 1.5$, heated ($T_{jet}/T_\infty = 2.7$) jet. These measurements have been Fourier-transformed in time and azimuthal angle θ; the figure shows axisymmetric (*i.e.*, having azimuthal wavenumber $m = 0$) fluctuations of frequency $St = fD/U_{jet} = 0.25$. Radiation peaks at low angles ϕ to the axis where it is highly directive. At higher angles (near the sideline) the curve flattens out, a testament to the isotropic nature of radiation to these angles. Note that the peak fluctuations in this case are roughly $25dB$ or 270 times greater in power than those near the sidelines. This directivity is further exaggerated at still higher Mach numbers and diminished at lower Mach numbers (see figure 1.3).

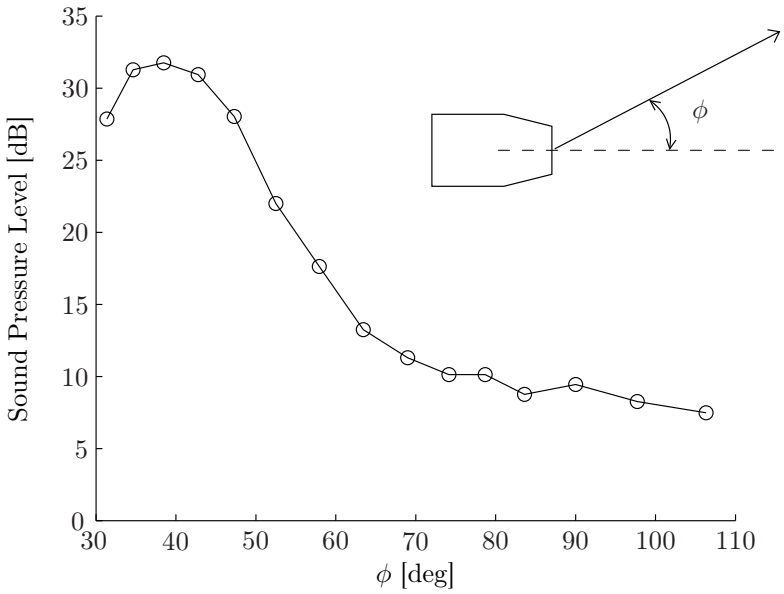

Figure 1.2: Acoustic power measurements of a heated $M_\infty = 1.5$ jet with temperature ratio $T_{jet}/T_\infty = 2.7$. Azimuthal mode $m = 0$ and frequency $St = 0.25$. Data obtained from measurements of Suzuki & Colonius (2006).

1.3 Theoretical Background

1.3.1 Aeroacoustics of Jets

There are several excellent and exhaustive review articles in the literature on aeroacoustics and jet noise. Examples include Crighton (1975), Ffowcs-Williams (1977), Lilley (1991), Tam (1995), and Tam (1998), to name but a few. Major reviews of computational aeroacoustics are given by Colonius & Lele (2004) and Wang *et al.* (2006). In what follows we recount some important concepts and developments.

In the 1950's, Lighthill (1952, 1954) developed his theory of Aeroacoustics: the study of sound generated *"...as a byproduct of an airflow, as distinct from sound generated by the vibration of a solid."* Lighthill's insight was that, for sound waves of small amplitude, and in the absence of a resonant mechanism[1], sound generation can be studied separately from its propagation. He formalized this by linearizing the Navier-Stokes equations about a known mean flow and separating

[1]Two examples of such resonance are self-sustaining oscillations in flows over open cavities (*e.g.*, Rowley *et al.*, 2002) and the thermo-acoustic instability of the Rijke tube (*e.g.*, Balasubramanian & Sujith, 2008).

operators according to their character; propagation on one side, everything else (the sources) on the other:

$$\mathcal{L}\mathbf{q} = \mathcal{S}(\mathbf{q}). \tag{1.1}$$

The linear operator $\mathcal{L}$ is referred to as the propagator, $\mathcal{S}$ represents the nonlinear sources of sound and $\mathbf{q}$ is the vector of flow variables. This separation between source and propagation is now known as the *Acoustic Analogy*: the resultant acoustic field is equivalent to that which would be realized in a quiescent medium (see below) in the presence of an externally applied stress, contained within $\mathcal{S}$. We note that equation (1.1) is an exact relation and so is the acoustic analogy; the question becomes one of the veracity of source modeling[2].

Lighthill studied the propagation of sound in a quiescent medium with embedded quadrupole sources, in which case equation (1.1) becomes (*Lighthill's equation*)

$$\frac{\partial^2 \rho}{\partial t^2} - a_\infty^2 \nabla^2 \rho = \frac{\partial^2 T_{ij}}{\partial x_i \, \partial x_j}, \tag{1.2}$$

where ρ is the density and T_{ij} is *Lighthill's turbulence stress tensor*, given by

$$T_{ij} = \rho u_i u_j + (p - \rho a_\infty^2)\delta_{ij} - \tau_{ij}, \tag{1.3}$$

where a_∞ is the ambient speed of sound; p and u_i are the pressure and velocity in direction $\mathbf{i}$, respectively; δ_{ij} is the Kronecker delta; and τ_{ij} is the viscous stress tensor.

Using dimensional analysis, Lighthill showed that the acoustic power radiated by a flow with typical velocity U_{jet} should be proportional to U_{jet}^8. Lighthill also showed that, due to the effects of (quadrupole) source convection, the radiation is augmented by a factor of $|1 - M_\infty \cos\phi|^{-5}$, where $M_\infty = U_{jet}/a_\infty$ is the acoustic Mach number and ϕ is the angle between the stationary observer and the source at the time of sound emission (see figure 1.2). The augmenting factor represents the Doppler effect, causing enhanced radiation in the direction of the flow and reduced radiation

[2]It should be noted that the source description is not unique, *i.e.*, the sources should be regarded as *equivalent sources*.

in the other (waves "pile up" ahead of the source). Ffowcs-Williams (1963) investigated the effects of source convection and found that, at supersonic convection speeds, the Doppler factor alters the U_{jet}^8 radiation power dependence to U_{jet}^3. These two power laws have been described as the most important results of the classical acoustic analogy theory (Tam, 1998).

As mentioned above, Lighthill's formulation of the acoustic analogy embedded sources in an otherwise quiescent medium. This is an appropriate assumption to make in a uniform stream containing turbulent fluctuations. In a real jet, however, the sound generated within the core is affected by the shear layer upon passage through it. This can be visualized by imagining a wave front traveling within, and in parallel to the shear layer. Portions of the wave front situated closer to the centerline will travel faster than outer portions as they are embedded in a higher-speed flow. Such fronts are therefore deflected outwards. This effect is further enhanced in heated jets due to the radial decay of sound speed[3]. This results in the so-called cone of silence: a region close to the downstream direction (at small ϕ) into which sound generated within the jet core cannot propagate.

To account for the refraction by the mean flow, the propagator $\mathcal{L}$ must be modified from the homogeneous version in equation (1.2). Lilley (1974) suggested that the appropriate propagator is the set of the linearized Euler equations, which include radial inhomogeneities in the mean flow. This approach gained popularity and became known as the Modified Acoustic Analogy. Goldstein (1984) suggested a different approach in which no attempt is made to separate the sources of sound from its subsequent propagation. Here the full equations are linearized from the outset about a known mean flow and an initial value problem is solved. This approach, while taking a different viewpoint, usually leads to similar predictions to those of the modified acoustic analogy. Goldstein (2003) later generalized Lighthill's acoustic analogy by showing that there is an exact analogy between the fluctuations in any real flow and the linear inviscid fluctuations about an arbitrary base flow produced by externally imposed stress and energy flux perturbations (as opposed to Lighthill's quadrupoles).

Further complicating is the presence of solid bodies, such as the nozzle. The interaction between the nozzle and the shear layer can serve as an additional source of sound, referred to as *excess noise*

[3]The reverse is true for cooled jets, although this case is not of practical importance.

(Crighton, 1972). Using vortex-sound theory (Möhring, 1978), Bridges & Hussain (1992) calculated the *extinction angle* (a single angle into which no sound can radiate; not the same as the cone of silence), and hypothesized that the observed differences between theoretical and experimental values thereof were due to the presence of the nozzle in the experimental jet. Bridges & Hussain (1995) later showed that the nozzle-flow interaction forms a dipole whose radiated sound can have comparable power to the quadrupole sound in the free-stream.

As hinted at in the above, the radiated sound from a flow depends sensitively on its sources as well as the medium through which it passes as it travels from source to observer. Prior to the 1970's, the prevailing view of turbulence was one of an agglomeration of incoherent, fine-scale fluctuations. The radiated field, the result of the interaction of such motions, should then exhibit similar incoherence. This is not the case, as discovered by Mollo-Christensen (1967), who found that pressure fluctuations outside a fully turbulent jet appear in well-defined wave-packets. Presumably this implies that at least a part of the source-field is indeed coherent. Crow & Champagne (1971), spurred on by earlier hints of orderly structures, studied jet turbulence and found "vortex puffs" that appeared in a coherent manner when forced at their most unstable frequency. This was the case even at Reynolds numbers as high as $Re = (UD/\nu)_{jet} = 10^5$. Further evidence was provided by Brown & Roshko (1974) and Winant & Browand (1974) who studied planar mixing layers of different densities and velocities. We note that the appearance of large-scale structures in laminar jets had been studied and described long before the work of Crow & Champagne. Such jets develop instability as the Reynolds number is increased; the axisymmetric shear layer rolls up into vortices before transition to turbulence. The persistence of such structures through transition was however not accepted until the 1970's.

The modified acoustic analogy is in theory capable of predicting noise from both large- and fine-scale turbulent motions. However, this requires complete knowledge of the source terms which in practice is not available, particularly for the large-scale turbulence. This explains why methods based on the modified acoustic analogy have been most successful in predicting sideline noise. There is however a considerable body of work dealing with theoretical models of large scale coherent

structures. This is the subject of the next section.

1.3.2 Instability Models of Large-Scale Coherent Structures

Roughly speaking, a flow is said to be unstable when small disturbances introduced into the flow can grow over time. This notion can be infused with rigour via the introduction of a metric for growth. A flow can then be stable with respect to one metric but unstable with respect to another (*e.g.*, not all Lyapunov-stable configurations are asymptotically stable). Such distinctions are however not necessary in the present context.

Flow instabilities generally occur as the result of an imbalance between external forces, inertia, and viscous stresses (Drazin & Reid, 1969) and every type of flow instability is capable of producing large-scale coherent structures (Hussain, 1983). Free shear flows such as the jet are susceptible to the Kelvin-Helmholtz instability and most attempts at providing theoretical models for the development of large-scale coherent structures in such flows are based upon this. The resulting fluctuations are then typically computed via linear stability analysis (see section 2.3.1), where the mean flow is assumed to be parallel, or nearly so.

Turbulence statistics in parallel flows are stationary, both with respect to streamwise distance x and time t. For such cases the solution is separable and exhibits complex-exponential dependence on these coordinates, with complex wavenumber α and frequency ω respectively[4]. Free shear layers are of course not parallel, but for small spreading rates the parallel-flow assumption is reasonable.

One of the first investigations on the linear stability of jets was that of Batchelor & Gill (1962). They determined the stability of a jet in the two extremes: very near the nozzle, and far downstream in the developed region (see figure 1.1). They modeled the near nozzle shear layer as a cylindrical vortex sheet and the far jet as a parabola (no potential core). As expected, they found the vortex sheet to be unstable to disturbances of all frequencies St and azimuthal wavenumbers m, while they proved that the far jet is only unstable to disturbances with $m = 1$. They were however unable to predict the formation of vortex puffs (rings), reported that same year by Reynolds (1962) in his study

[4] α and ω are respectively complex and real for spatially growing waves while the converse is true for temporally growing waves. In general they can both be complex; see section 2.3.1.

of a low Reynolds number ($Re < 300$) jet. Crow & Champagne performed linear stability analysis to supplement their experimental study. They solved both the temporal and spatial stability problems and successfully predicted the phase-velocity of the most unstable wave using the temporal approach, while the spatial prediction did not match experiment. This lead them to conclude that the spatial approach is not appropriate. However, as pointed out by Mattingly & Chang, Crow & Champagne based their analysis on a top-hat profile (a vortex sheet), which does not faithfully represent a typical transverse velocity profile of a real jet. This was also the reason why the analysis of Batchelor & Gill did not anticipate the formation of the vortex rings. Mattingly & Chang based their analysis on experimentally determined velocity profiles of a $Re = 300$ jet. To partially incorporate the effects of streamwise variation in the flow, they solved the spatial stability problem at successive cross-sections throughout the jet. Near the nozzle they find the $m = 0$ mode to be most unstable, followed closely by $m = 1$. This is reversed further downstream, in agreement with the results of Batchelor & Gill. Mattingly & Chang find good agreement between theory and experiment in terms of growth rates, axial wavelengths, and intensity of fluctuations (where the eigenfunction is compared to measurements).

As mentioned above, Mattingly & Chang performed their analysis at various cross-sections of the jet. This approach, referred to as the *locally-parallel* assumption, takes advantage of the fact that while the statistics might vary between widely separated points, relative to the wavelength of the disturbance in question, they do not vary much locally. Higher-order expansions such as multiple-scales analysis and the parabolized stability equations, discussed in section 2.3.2 and chapter 3, further take into account such variations. Crighton & Gaster (1976) used multiple-scales analysis and found good agreeance with the measurements of Crow & Champagne. This work was however limited to axisymmetric and incompressible disturbances, while disturbances with $m = 1$ play a significant role in the shear layer instability of a jet, particularly in the developed region. This had been predicted by Batchelor & Gill and was verified experimentally by Mattingly & Chang and further by Moore (1977).

The existence of large-scale coherent structures and, in particular, their persistence through

transition was widely accepted in the late 1970's. Their modeling via the linear instabilities of the turbulent mean flow profiles had enjoyed success, particularly in predicting the wavelength of the most unstable disturbance, typically occurring at Strouhal numbers between 0.3 and 0.4 (depending on the flow condition). While the relevance of these flow structures to the radiated sound seemed reasonable, little work had been done to elucidate such connections or indeed make predictions. This is the topic of the next section.

1.3.3 Noise Generation by Large-Scale Coherent Structures

One consequence of Lighthill's analysis (Lighthill, 1952) was the U_{jet}^8 power law for low-speed jets. This has been experimentally verified, but only for very clean jets; the law fails at relatively low exit disturbance levels. This is due to flow instabilities that get excited by the broadband noise at the exit and subsequently grow, altering the jet turbulence away from that assumed by Lighthill. It is thus clear that coherent motions affect the radiated sound indirectly, even in the case that they themselves do not radiate sound.

It is equally clear that the radiation efficiency of a source is heavily dependent upon its convection speed. Figure 1.3 shows far-field pressure measurements for two equally heated jets; one having $M_\infty = 0.5$ and the other $M_\infty = 1.5$. Enormous differences are found in peak power: the peak levels on the two measurements are roughly $38dB$ apart (the ratio is 6300). Also apparent is variation in directivity: the max/min power ratio is $25db$ for the high-speed jet, and $13dB$ for the other. Apparently the directivity of radiation, as well as the power, is strongly dependent upon U_{jet} (and a_∞, fixed here).

Troutt & McLaughlin (1982) studied a $M_\infty = 2.1$ jet and found that the large-scale structures are responsible for the peak noise at this condition and that they radiate primarily in the downstream direction. Via ray-tracing, they further found that the sound generated by these structures originates in the region where they saturate in amplitude and subsequently decay. They hypothesize that the dominant sources of large-scale sound are Mach wave radiation and the breakdown of the associated structures as they lose their coherence via nonlinear interactions. Mach wave radiation is associated

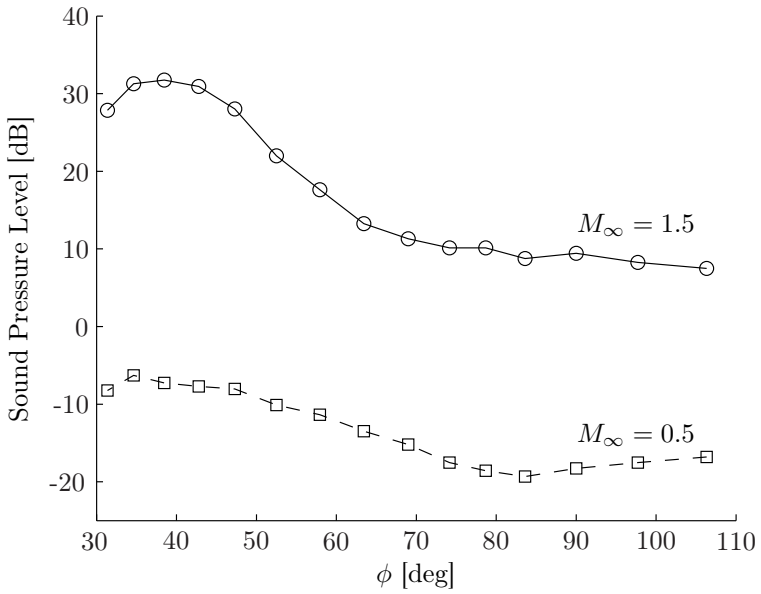

Figure 1.3: Acoustic power measurements for two heated jets at $M_\infty = 0.5$ and 1.5; temperature ratio $T_{jet}/T_\infty = 2.7$. Azimuthal mode $m = 0$ and frequency $St = 0.25$. Data obtained from measurements of Suzuki & Colonius (2006).

with supersonically convecting disturbances and as such does not appear in subsonic flows (but see below). The latter mechanism does, however, and it has been suggested (Hussain, 1983, 1986) that this may be the dominant source of sound, at least at subsonic conditions.

Despite the absence of Mach wave radiation from subsonic flows, such flows share many similarities with supersonic flows in terms of sound radiation. Laufer & Yen (1983) studied a low Mach number jet and found the associated radiation to originate from the nonlinear saturation of large-scale structures and to be highly directional in character, just as was found at supersonic conditions. Crighton & Huerre (1990) later explored this theoretically, finding the directivity to be associated with the non-compactness[5] of the source region. In fact, they found *super-directivity*: the directivity pattern depends exponentially on $\cos(\phi)$, where ϕ is measured from the downstream direction.

The highly directive nature of the noise of large-scale coherent structures, contrasted with the isotropic nature of that of the smaller scales, hints at the possibility that the spectra of the two components might be separated. To this end, Tam *et al.* (1996) analyzed a large database of measured jet noise spectra. They did indeed find two distinct spectra; that dominating at sideline angles

[5] A source region of spatial extent L is acoustically compact if $L \ll \lambda$ where λ is the largest radiated wavelength.

($\phi = 90°$, say), and that at low angles ($\phi = 30°$, say). The two spectra have qualitative and quantitative differences: the sideline spectrum is relatively flat and peaks at higher frequencies while the downstream spectrum has a distinct peak at lower frequencies. Further, they also found that the spectra collapse across different operating conditions when scaled with their respective peak frequencies. Perhaps most interesting was their finding that the Mach number did not matter: the two components exist for both subsonic and supersonic jets, suggesting that the mechanisms for noise generation may be the same. Thus, while the effectiveness of radiation from large-scale structures at lower speeds might be reduced, it occurs via a similar mechanism: Mach wave radiation persists through the sonic point.

The acoustic analogy and modified versions thereof have enjoyed the greatest success in predicting turbulent mixing noise produced by fine-scale turbulence. This is due to the nature of the quadrapole source modeling for each type of motion: the nearly isotropic and broadband incoherent motions are statistically simpler than the anisotropic and narrow-band coherent motions, easily correlated over distances comparable to the transverse support of the jet (although this depends on forcing conditions). The locally-parallel linear instability wave, while a valid approximation in the near-field, has no far-field. To obtain predictions based on this solution it must be matched with an outer solution (to the wave equation), valid in the far field. Tam & Morris (1980) did this for a supersonic planar layer, additionally using the multiple-scales approach to model the effects of mean-flow divergence. They obtained qualitative agreement with experimental data, particularly in terms of directivity. Tam & Burton (1984) performed a similar analysis for an axisymmetric supersonic jet and obtained favourable comparisons with experiments. Higher order approximations, involving the Parabolized Stability Equations (PSE, see section 2.3.2) result in further improvements.

Subsonic conditions however still represent a challenge for instability-based methods as the far-field is absent from the solution, even for the PSE. The near-field is well modeled, though, allowing the inner instability solution to be coupled with projection methods (*e.g.*, via a Kirchhoff-surface) (Cheung & Lele, 2009) to deliver reasonable far-field approximations.

1.4 Thesis Outline

In chapter 2 we summarize the computational methodology as well as the data-processing procedures employed in this thesis.

As described in section 1.3.2, large-scale coherent structures in jets have traditionally been modeled based on the Kelvin-Helmholtz instability of the jet shear layer. Such efforts have been successful, particularly for forced jets at relatively low Reynolds number (*e.g.*, Mattingly & Chang, 1974). At unforced conditions (*i.e.*, for "natural jets"), such disturbances are correlated over shorter spatial and temporal length scales. This is exaggerated at higher Reynolds numbers where, additionally, the fractional energy with large scale coherent structures is diminished due to increased production of fine-scale turbulence. This renders the decomposition of turbulence ambiguous at best and meaningless at worst.

But this is only the case in the region of intense turbulence, such as in the shear layer. As recognized by Suzuki & Colonius (2006), pressure fluctuations from different sources (*e.g.*, instability waves and quadrupoles) have different spatial decay characteristics. While such disturbances might not be separated in a unique manner at one location, they might be at another, due to one decaying faster than the other. In particular, Suzuki & Colonius recognized that, outside the shear layer, there is a region (the "linear hydrodynamic region") where hydrodynamic pressure fluctuations, associated with instability waves, dominate the pressure field. This is illustrated in figure 3.1.

Using a caged microphone array, Suzuki & Colonius made measurements in the linear hydrodynamic region and compared them to predictions based on locally-parallel linear stability analysis. They obtained excellent agreement near the most unstable frequency. In chapter 3 we apply the Parabolized Stability Equations to the same problem and demonstrate significant advantages over the locally-parallel solution. In addition, we decompose the microphone measurements using the Proper Orthogonal Decomposition and show how agreement can be extended even beyond the potential core in some cases.

Nozzle serrations generate streamwise vorticity, promoting the mixing of the jet fluid with the ambient and shortening the potential core. They also reduce noise at low frequencies and aft angles,

but increase noise at high frequencies. Sound radiated at low frequencies and aft-angles is associated with large-scale coherent structures convecting within the jet. The streamwise vorticity, induced by the serrations, interrupts the noise generation by large-scale structures, perhaps by retarding their initial growth. It therefore seems reasonable to assume that linear stability analysis can offer some understanding of the effects of serrations on coherent motions in the flow, particularly in light of the demonstrated success of such analysis for round jets (chapter 3). In chapter 4 we extend the locally-parallel framework for axisymmetric jets to serrated jets, such as those produced by chevron nozzles. We explore the effects of azimuthal asymmetry on linear stability characteristics and also compare predictions to caged-array measurements.

In chapter 5 we summarize the conclusions drawn from our work.

1.5 Publications

The following journal articles and conference proceedings are based on the work described in this thesis:

1.5.1 Journal Publications

1. K. Gudmundsson and T. Colonius. 2010 "Instability Wave Models for the Near Field Fluctuations of Turbulent Jets," in preparation *J. Fluid Mech.*

2. K. Gudmundsson and T. Colonius. 2010 "The Effects of Nozzle Serrations on the Linear Stability of Turbulent Jets," in preparation, *J. Fluid Mech.*

1.5.2 Conference Proceedings

1. R.H. Schlinker, R.A. Reba, J.C. Simonich, T. Colonius, K. Gudmundsson and F. Ladeinde. "Towards prediction and control of large-scale turbulent structure supersonic jet noise," *The ASME Turbo Expo 2009*, Orlando, Florida, June 2009. *ASME Paper 2009-60300.*

2. K. Gudmundsson and T. Colonius. "Parabolized stability equation models for turbulent jets

and their radiated sound," *The 15th AIAA/CEAS Aeroacoustics Conference*, Miami, Florida, May 2009. *AIAA Paper 2009-3380*.

3. R.H. Schlinker, J.C. Simonich, D.W. Shannon, R.A. Reba, T. Colonius, K. Gudmundsson and F. Ladeinde. "Supersonic jet noise from round and chevron nozzles: experimental studies," *The 15th AIAA/CEAS Aeroacoustics Conference*, Miami, Florida, May 2009. *AIAA Paper 2009-3257*.

4. K. Gudmundsson and T. Colonius. "Spatial stability analysis of chevron jet profiles," *The 13th AIAA/CEAS Aeroacoustics Conference*, Rome, Italy, May 2007. *AIAA Paper 2007-3599*.

5. K. Gudmundsson and T. Colonius. "Linear stability analysis of chevron jet profiles," *ASME Joint U.S.-European Fluids Engineering Summer Meeting*, Miami, Florida, July 2006. *ASME Paper 2006-98485*.

Chapter 2

Computational Models and Experimental Data

2.1 The Governing Equations

The flows investigated in this study are governed by the compressible Navier-Stokes equations. We non-dimensionalize independent variables as

$$x = \frac{x^*}{D}; \quad r = \frac{r^*}{D}; \quad t = \frac{t^* a_\infty}{D}, \tag{2.1}$$

where stars denote dimensional variables, D denotes the nozzle diameter, x and r respectively denote the streamwise and radial coordinates, t denotes time, and a_∞ denotes speed of sound in the ambient. The coordinate system is illustrated in figure 2.1. Dependent variables are non-dimensionalized as

$$u = \frac{u^*}{a_\infty}; \quad \rho = \frac{\rho^*}{\rho_\infty}; \quad p = \frac{p^*}{\rho_\infty a_\infty^2}; \quad T = \frac{c_p T^*}{a_\infty^2}, \tag{2.2}$$

where ρ_∞ denotes ambient density, u denotes any of the velocities u_x, u_r or u_θ, T denotes temperature, c_p represents specific heat at constant pressure; and p denotes pressure.

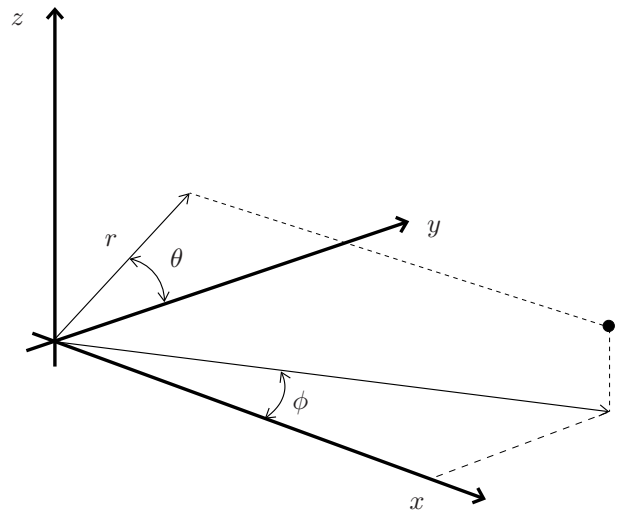

Figure 2.1: The coordinate system used in this thesis.

So scaled, the governing equations, including the equation of state for an ideal gas, are given by

$$\rho\frac{Du_x}{Dt} = -\frac{\partial p}{\partial x} + \frac{1}{Re}V_x, \tag{2.3}$$

$$\rho\left(\frac{Du_r}{Dt} - \frac{u_\theta^2}{r}\right) = -\frac{\partial p}{\partial r} + \frac{1}{Re}V_r, \tag{2.4}$$

$$\rho\left(\frac{Du_\theta}{Dt} + \frac{u_r u_\theta}{r}\right) = -\frac{1}{r}\frac{\partial p}{\partial \theta} + \frac{1}{Re}V_\theta, \tag{2.5}$$

$$\rho\left(\frac{DT}{Dt} + (\gamma-1)T\,\nabla\cdot\mathbf{u}\right) = \frac{\gamma}{Re}\Phi + \frac{\gamma}{Re\,Pr}\nabla\cdot\mathbf{Q}, \tag{2.6}$$

$$\frac{D\rho}{Dt} + \rho\,\nabla\cdot\mathbf{u} = 0, \tag{2.7}$$

$$p = \frac{\gamma-1}{\gamma}\rho T, \tag{2.8}$$

where γ is the ratio of specific heats, taken as 1.4 in the current simulations. The Reynolds number is defined as $Re = U_{jet}D/\nu_{jet}$ and the Prandtl number as $Pr = \mu_\infty c_p/k_\infty = 0.72$. We neglect temperature dependence of viscosity as the experimental jets in our study are either near-isothermal or modestly heated. ∇ is the divergence operator, given by

$$\nabla\cdot\mathbf{f} = \frac{\partial f_x}{\partial x} + \frac{1}{r}\frac{\partial (r f_r)}{\partial r} + \frac{1}{r}\frac{\partial f_\theta}{\partial \theta}, \tag{2.9}$$

where $\mathbf{f} = (f_x, f_r, f_\theta)$. The convective derivative is given by

$$\frac{D}{Dt} = \frac{\partial}{\partial t} + u_x \frac{\partial}{\partial x} + u_r \frac{\partial}{\partial r} + \frac{u_\theta}{r} \frac{\partial}{\partial \theta}. \tag{2.10}$$

$\mathbf{V}$, Φ, and $\mathbf{Q}$ represent the viscous terms, viscous dissipation, and heat fluxes, respectively. The first two are written in terms of the symmetric viscous stress tensor τ, which in cylindrical coordinates is given by

$$\begin{aligned}
\tau_{xx} &= 2\mu M_\infty \left(\frac{\partial u_x}{\partial x} - \frac{1}{3}\Theta \right), && (2.11)\\
\tau_{rr} &= 2\mu M_\infty \left(\frac{\partial u_r}{\partial r} - \frac{1}{3}\Theta \right), && (2.12)\\
\tau_{\theta\theta} &= 2\mu M_\infty \left(\frac{1}{r}\frac{\partial u_\theta}{\partial \theta} + \frac{u_r}{r} - \frac{1}{3}\Theta \right), && (2.13)\\
\tau_{xr} &= \mu M_\infty \left(\frac{\partial u_r}{\partial x} + \frac{\partial u_x}{\partial r} \right), && (2.14)\\
\tau_{x\theta} &= \mu M_\infty \left(\frac{\partial u_\theta}{\partial x} + \frac{1}{r}\frac{\partial u_x}{\partial \theta} \right), && (2.15)\\
\tau_{r\theta} &= \mu M_\infty \left(\frac{\partial u_\theta}{\partial r} + \frac{1}{r}\frac{\partial u_r}{\partial \theta} - \frac{u_\theta}{r} \right), && (2.16)
\end{aligned}$$

where $\Theta = \nabla \cdot \mathbf{u}$ is the dilatation. The viscous terms in $\mathbf{V}$ are then given by

$$\begin{aligned}
V_x &= \nabla \cdot (\tau_{xx}, \tau_{xr}, \tau_{x\theta}), && (2.17)\\
V_r &= \nabla \cdot (\tau_{xr}, \tau_{rr}, \tau_{r\theta}) - \frac{\tau_{\theta\theta}}{r}, && (2.18)\\
V_\theta &= \nabla \cdot (\tau_{x\theta}, \tau_{r\theta}, \tau_{\theta\theta}) + \frac{\tau_{r\theta}}{r}, && (2.19)
\end{aligned}$$

and the scalar dissipation function Φ by

$$\begin{aligned}
\Phi &= \tau_{xx}\frac{\partial u_x}{\partial x} + \tau_{xr}\frac{\partial u_r}{\partial x} + \tau_{x\theta}\frac{\partial u_\theta}{\partial x} && (2.20)\\
&+ \tau_{xr}\frac{\partial u_x}{\partial r} + \tau_{rr}\frac{\partial u_r}{\partial x} + \tau_{r\theta}\frac{\partial u_\theta}{\partial x}\\
&+ \frac{\tau_{x\theta}}{r}\frac{\partial u_x}{\partial \theta} + \frac{\tau_{r\theta} - u_\theta/r}{r}\frac{\partial u_r}{\partial \theta} + \frac{\tau_{\theta\theta} + u_r/r}{r}\frac{\partial u_\theta}{\partial \theta}.
\end{aligned}$$

The heat flux $\mathbf{Q}$ in equation (2.6) is given by Fourier's law:

$$\mathbf{Q} = \mu M_\infty \left(\frac{\partial}{\partial x}, \frac{\partial}{\partial r}, \frac{1}{r}\frac{\partial}{\partial \theta} \right) T \tag{2.21}$$

2.2 Linearization

The Navier-Stokes equations, equations (2.3) through (2.6), accurately describe the evolution of continuous Newtonian fluids. This covers most cases of practical interest, including the generation and propagation of sound under the flow conditions considered in this work. A common approach in the analysis of such nonlinear systems is *linearization*, in which small perturbations to a time-invariant (equilibrium) state are scrutinized for stability. We decompose the solution $\mathbf{q}$ as

$$\mathbf{q}(\mathbf{x}, t) = \overline{\mathbf{q}}(\mathbf{x}) + \mathbf{q}'(\mathbf{x}, t), \tag{2.22}$$

where $\overline{\mathbf{q}}$ and $\mathbf{q}'$ respectively denote the time-invariant and (low-energy) fluctuating states. Questions regarding the evolution of small perturbations to the equilibrium state may then be addressed via the solution ($\mathbf{q}'$) of the linearized Navier-Stokes equations. If the linear solution is unstable then the nonlinear solution is also unstable. Linear stability does not necessarily imply nonlinear stability, however, as nonlinear bifurcations to other states may occur.

The results of stability analysis are sensitive to the choice of mean flow. If the mean flow is thought to be laminar then solutions to the boundary-layer equations (*e.g.*, the Blasius boundary-layer) can be used. This is not the case here as the present jets are highly turbulent (see Reynolds number in table 2.1) and the effects of this on the mean flow must be accounted for. To this end, one could use equilibrium-solutions to the Navier-Stokes equations, but these are not available for the turbulent jets in our study, as they have Reynolds-numbers far beyond the capabilities of present methods and equipment. We can however compute the mean flow from experimental measurements

of such flows. This is particularly attractive as nonlinear effects are then partially included via their effect on the time-invariant state. This partially explains the effectiveness of the linear simulations in this work, discussed in the subsequent chapters.

Under the normalization introduced in equation (2.2), the decomposition in equation (2.22) becomes

$$u_x = \overline{u}_x + u'_x, \tag{2.23}$$

$$u_r = \overline{u}_r + u'_r, \tag{2.24}$$

$$u_\theta = u'_\theta \quad \text{(no mean swirl; } \overline{u}_\theta = 0\text{)}, \tag{2.25}$$

$$T = \frac{1}{\gamma - 1} + T', \tag{2.26}$$

$$\rho = 1 + \rho', \tag{2.27}$$

$$p = \frac{1}{\gamma} + p' \tag{2.28}$$

We proceed by substituting this decomposition into equations (2.3) through (2.8) and subtracting the mean:

$$\overline{\rho}\left(\frac{\overline{D}u'_x}{\overline{D}t} + \frac{\partial \overline{u}_x}{\partial x}u'_x + \frac{\partial \overline{u}_x}{\partial r}u'_r + \frac{1}{r}\frac{\partial \overline{u}_x}{\partial \theta}u'_\theta\right) = -\frac{\partial p'}{\partial x} + \frac{1}{Re}V'_x + f_x, \tag{2.29}$$

$$\overline{\rho}\left(\frac{\overline{D}u'_r}{\overline{D}t} + \frac{\partial \overline{u}_r}{\partial x}u'_x + \frac{\partial \overline{u}_r}{\partial r}u'_r + \frac{1}{r}\frac{\partial \overline{u}_r}{\partial \theta}u'_\theta\right) = -\frac{\partial p'}{\partial r} + \frac{1}{Re}V'_r + f_r, \tag{2.30}$$

$$\overline{\rho}\left(\frac{\overline{D}u'_\theta}{\overline{D}t} + \frac{\overline{u}_r u'_\theta}{r}\right) = -\frac{1}{r}\frac{\partial p'}{\partial \theta} + \frac{1}{Re}V'_\theta + f_\theta, \tag{2.31}$$

$$\overline{\rho}\left(\frac{\overline{D}T'}{\overline{D}t} + (\gamma - 1)\left(\overline{T}\,\nabla \cdot \mathbf{u}' + T'\,\nabla \cdot \overline{\mathbf{u}}\right)\right) = \frac{\gamma}{Re}\Phi' + \frac{\gamma}{Re\,Pr}\nabla \cdot \mathbf{Q}' + f_T, \tag{2.32}$$

$$\frac{\overline{D}\rho'}{\overline{D}t} + \overline{\rho}\,\nabla \cdot \mathbf{u}' + \rho'\,\nabla \cdot \overline{\mathbf{u}} = f_\rho, \tag{2.33}$$

$$p' = \frac{\gamma - 1}{\gamma}(\overline{T}\rho' + \overline{\rho}T'), \tag{2.34}$$

where the linearized convective derivative is given by

$$\frac{\overline{D}}{\overline{D}t} = \frac{\partial}{\partial t} + \overline{u}_x\frac{\partial}{\partial x} + \overline{u}_r\frac{\partial}{\partial r}. \tag{2.35}$$

Here we have collected all nonlinear fluctuating terms (*e.g.*, $u_r' u_\theta'/r$) into the vector $\mathbf{f}$ on the right hand side. Also note that the dissipation function Φ is nonlinear; such terms are included in f_T, with the linear part contained in Φ'. In this work we restrict our attention to linear disturbances and so do not discuss $\mathbf{f}$ further.

2.3 Modeling of Large-Scale Fluctuations

The system given in equations (2.29) through (2.34) is as exact as the nonlinear system in equations (2.3) through (2.8). This is because the nonlinear terms $\mathbf{f}$ are still present; only upon setting this term to zero do we obtain a truly linear system, the solution to which can be considered an adequate approximation to the full system, granted small amplitudes. Despite the great simplification resulting from the linearization step we wish to make further modeling approximations, exploiting our physical understanding to obtain as simple a problem as possible. This is not only for computational expedience but also to test our hypothesis as to the form of dominant fluctuations. This is the subject of the next two sections.

2.3.1 Normal Modes

Parallel mean flows are hypothetical flows in which all streamlines are parallel and aligned with the streamwise coordinate x. In such cases the mean flow vector is given by

$$\overline{\mathbf{q}}(\mathbf{x}) = (\overline{u}_x(r,\theta), 0, 0, \overline{\rho}(r,\theta), \overline{T}(r,\theta)). \tag{2.36}$$

It follows that the mean flow is only sheared in the radial and azimuthal directions. The analysis of disturbances to such mean flows is generally referred to as *linear stability analysis*, or LST for short. For simplicity we drop the prime on fluctuating variables in what follows, retaining the over-line to

denote the mean variable. The linearized equations become

$$\overline{\rho}\left(\frac{\overline{D}u_x}{\overline{D}t}+\frac{\partial\overline{u}_x}{\partial r}u_r+\frac{1}{r}\frac{\partial\overline{u}_x}{\partial\theta}u_\theta\right) = -\frac{\partial p}{\partial x}+\frac{1}{Re}V_x, \tag{2.37}$$

$$\overline{\rho}\frac{\overline{D}u_r}{\overline{D}t} = -\frac{\partial p}{\partial r}+\frac{1}{Re}V_r, \tag{2.38}$$

$$\overline{\rho}\frac{\overline{D}u_\theta}{\overline{D}t} = -\frac{1}{r}\frac{\partial p}{\partial\theta}+\frac{1}{Re}V_\theta, \tag{2.39}$$

$$\overline{\rho}\left(\frac{\overline{D}T}{\overline{D}t}+(\gamma-1)\overline{T}\,\nabla\cdot\mathbf{u}\right) = \frac{\gamma}{Re}\Phi+\frac{\gamma}{Re\,Pr}\nabla\cdot\mathbf{Q}, \tag{2.40}$$

$$\frac{\overline{D}\rho}{\overline{D}t}+\overline{\rho}\,\nabla\cdot\mathbf{u} = 0, \tag{2.41}$$

$$p = \frac{\gamma-1}{\gamma}(\overline{T}\rho+\overline{\rho}T), \tag{2.42}$$

where the linearized convective derivative is further simplified to

$$\frac{\overline{D}}{\overline{D}t}=\frac{\partial}{\partial t}+\overline{u}_x\frac{\partial}{\partial x}. \tag{2.43}$$

We can write the system defined by equations (2.37) through (2.41) in matrix form as

$$\frac{\partial\mathbf{q}}{\partial t}+\mathbf{A}(\overline{\mathbf{q}})\frac{\partial\mathbf{q}}{\partial r}+\mathbf{B}(\overline{\mathbf{q}})\frac{\partial\mathbf{q}}{\partial x}+\mathbf{C}(\overline{\mathbf{q}})\frac{\partial\mathbf{q}}{\partial\theta}+\mathbf{D}(\overline{\mathbf{q}})\,\mathbf{q}=0, \tag{2.44}$$

where we have now dropped terms relating to viscosity and heat conduction. This is because we're ultimately interested in the inviscid instabilities of the mean flow profiles under question.

Since the matrices **A** through **D** in equation (2.44) do not depend on time or the axial coordinate, it follows that the solution is separable in these directions and is of the form

$$\mathbf{q}(\mathbf{x},t)=\tilde{\mathbf{q}}(r,\theta)\,e^{i\alpha x}\,e^{-i\omega t}, \tag{2.45}$$

where α and ω are potentially complex constants, the negative sign on ω being a matter of convention. If $\overline{\mathbf{q}}$ is also homogeneous in the azimuthal direction (*i.e.*, $\partial_\theta\overline{\mathbf{q}}=0$) then $\tilde{\mathbf{q}}(r,\theta)$ can be further decomposed so that

$$\mathbf{q}(\mathbf{x},t)=\hat{\mathbf{q}}(r)\,e^{i\alpha x}\,e^{im\theta}\,e^{-i\omega t}, \tag{2.46}$$

where only integral values of m are permissible (so that the solution is 2π-periodic in θ). For general $\mathbf{q}$ equation (2.46) becomes a double integral over ω-α space, summed over all m's. However in a linear context each of these waves evolves independently, allowing the study of individual components as we do in equation (2.46). Azimuthal inhomogeneities in $\overline{\mathbf{q}}$ are considered in chapter 4.

Substituting equation (2.46) into equation (2.44) we obtain

$$\mathbf{A}\frac{d\,\hat{\mathbf{q}}}{dr} + (-i\omega\mathbf{I} + i\alpha\mathbf{B} + im\mathbf{C} + \mathbf{D})\,\hat{\mathbf{q}} = 0. \tag{2.47}$$

The parameters $\alpha = \alpha_r + i\alpha_i$ and $\omega = \omega_r + i\omega_i$ are as yet unknown and one or the other must be specified in order that a solution be obtained. The specified parameter is generally chosen to be real, and the unknown parameter will in general be complex.

In *temporal* stability analysis we choose the streamwise wavenumber α_r, setting $\alpha_i = 0$, and solve for the angular frequency ω. The solution will then grow in time at a fixed location if the growth-rate ω_i is positive. Rearranging equation (2.47), we obtain

$$\left(\mathbf{A}\frac{d}{dr} + i\alpha\mathbf{B} + im\mathbf{C} + \mathbf{D}\right)\hat{\mathbf{q}} = i\omega\hat{\mathbf{q}}, \tag{2.48}$$

an eigenvalue problem, with $i\omega$ being the eigenvalues and $\hat{\mathbf{q}}$ the eigenvectors.

In *spatial* stability analysis we choose the angular frequency ω_r, setting $\omega_i = 0$, and solve for the streamwise wavenumber α_r and growth-rate α_i. The solution will then grow in the streamwise direction at a fixed time if $-\alpha_i > 0$. Again rearranging equation (2.47), we obtain

$$\left(\mathbf{A}\frac{d}{dr} + i\omega\mathbf{I} + im\mathbf{C} + \mathbf{D}\right)\hat{\mathbf{q}} = -i\alpha\mathbf{B}\hat{\mathbf{q}}, \tag{2.49}$$

so that we now have a generalized eigenvalue problem.

In either the spatial or temporal approach the eigenvalue-eigenvector pairs are referred to as the normal modes of the linearized equations. These modes, if unstable, are assumed to dominate the large-scale dynamics of small-amplitude perturbations in weakly spreading flows. In convectively

unstable flows such as free shear layers, disturbances grow as they are convected downstream with the flow, but not at a fixed location (see excellent review by Ho & Huerre, 1984). The spatial approach is therefore the appropriate choice for such flows and is adopted in the current work.

While equation (2.49) is well suited to illustrate the eigenvalue-nature of the problem, it is not in the format best suited for its solution. Rather, we eliminate all variables but pressure from the system to obtain a single ODE, the Rayleigh equation:

$$\frac{1}{r}\frac{d}{dr}\left(r\frac{d\hat{p}}{dr}\right) - \left(\frac{2\partial_r \overline{u}_x}{\alpha\,\overline{u}_x - \omega} + \frac{\partial_r \overline{\rho}}{\overline{\rho}}\right)\frac{d\hat{p}}{dr} - \left(\frac{m^2}{r^2} + \alpha^2 - \overline{\rho}(\alpha\overline{u}_x - \omega)^2\right)\hat{p} = 0. \tag{2.50}$$

The mean shear $\partial_r \overline{u}_x$ vanishes as $r \to 0$ and $r \to \infty$ so that this becomes

$$\frac{1}{r}\frac{d}{dr}\left(r\frac{d\hat{p}}{dr}\right) - \left(\frac{m^2}{r^2} + \alpha^2 - \overline{\rho}(\alpha\,\overline{u}_x - \omega)^2\right)\hat{p} = 0. \tag{2.51}$$

Equation (2.51) is Bessel's equation, whose solutions are the Bessel functions of the first and second kind and linear combinations thereof. The boundary conditions for equation (2.50) follow from this:

$$\text{as } r \to 0 \qquad \hat{p}(r) \sim J_m\left(\sqrt{\overline{\rho}(M_\infty\,\alpha - \omega)^2 - \alpha^2}\,r\right), \tag{2.52}$$

and

$$\text{as } r \to \infty \qquad \hat{p}(r) \sim H_m^2\left(\sqrt{w^2 - \alpha^2}\,r\right), \tag{2.53}$$

where J_m and H_m^2 are the m-th order Bessel function of the first kind, and Hankel function of the second kind, respectively. The two-point boundary problem formed by equation (2.50) and equations (2.52) and (2.53) is solved via a shooting procedure, described in detail in appendix A. Briefly, given an input frequency ω and an initial guess α_0, equation (2.50) is integrated from the axis (using equation (2.52) as a starting condition) into the far field where we check whether equation (2.53) is satisfied. If it is not, changes are made to the guess and the process is repeated until convergence is obtained. Special care has to be taken near the critical layer at $r = r_c$, where $\alpha\,\overline{u}_x(r_c) - \omega = 0$. This is a regular singular point of equation (2.50) and is only a problem when

computing neutral or near-neutral modes, where the growth-rate α_i vanishes. The path of integration must then be deformed to avoid the singularity. This procedure is described in section A.1.2.

The shooting procedure is relatively fast and therefore suitable when a succession of values $\alpha(\omega)$ are desired along a curve ω, as the starting guess $\alpha_0(w+\Delta\omega)$ will generally be close to $\alpha(\omega)$, resulting in rapid convergence. There are other cases however when we care less about speed and more about obtaining the entire eigenvalue spectrum for each ω. Depending on the initial guess, the shooting procedure will generally converge to the most unstable eigenvalue, leaving others hard to find.

We therefore also solve equation (2.50) *directly*: the eigenvalue problem is discretized and solved via a matrix eigenvalue solver. In this case we rearrange the Rayleigh equation into a cubic generalized eigenvalue problem:

$$(f_3\alpha^3 + f_2\alpha^2 + f_1\alpha^1 + f_0)\hat{p} = 0. \tag{2.54}$$

This system is linearized before application of the eigenvalue solver. This is described in section A.2.1, where the coefficients f_j can also be found.

Figure 2.2 shows a typical eigenspectra for the analytical mean flow profile given in equation (3.1), computed via the direct method. This profile is axisymmetric and, for the profile parameters chosen in this example ($R = 0.5; u_c = 1; \delta = 0.1$), has only one inflection point and so only one unstable mode, shown in the figure. This example also illustrates another property of the Rayleigh equation: if $(\alpha, \hat{p})$ is a solution then the complex conjugate $(\alpha^*, \hat{p}^*)$ is as well. Note the neutral mode (having $\alpha_i = 0$) in figure 2.2. This mode is not a shear layer mode but a vortical mode, contained entirely within the jet core. This mode is passively advected with the flow at phase-speed $c_p = M_\infty$. Figure 2.3 shows typical eigenfunctions $\hat{p}$, $\hat{u}_x$, and $\hat{u}_r$, based on the same conditions. $\hat{p}(r)$ is computed directly from the Rayleigh equation, while the other two are computed via substitution of $\hat{p}(r)$ back into the original system (2.37-2.42). These eigenfunctions exhibit the expected behavior away from the shear layer, as indicated by the asymptotics in equations (2.52) and (2.53).

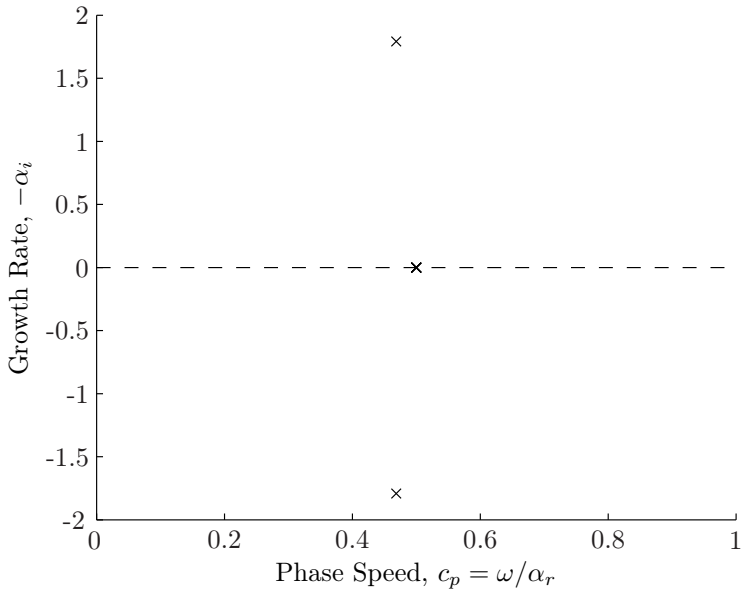

Figure 2.2: Typical eigenspectra of equation (3.1) calculated via the direct method. Only one unstable mode exists for this flow profile. The neutral mode is not a shear layer mode but a vortical mode, entirely contained within the jet core. This is for $m = 0$, $St = 0.35$ and $M_\infty = 0.5$.

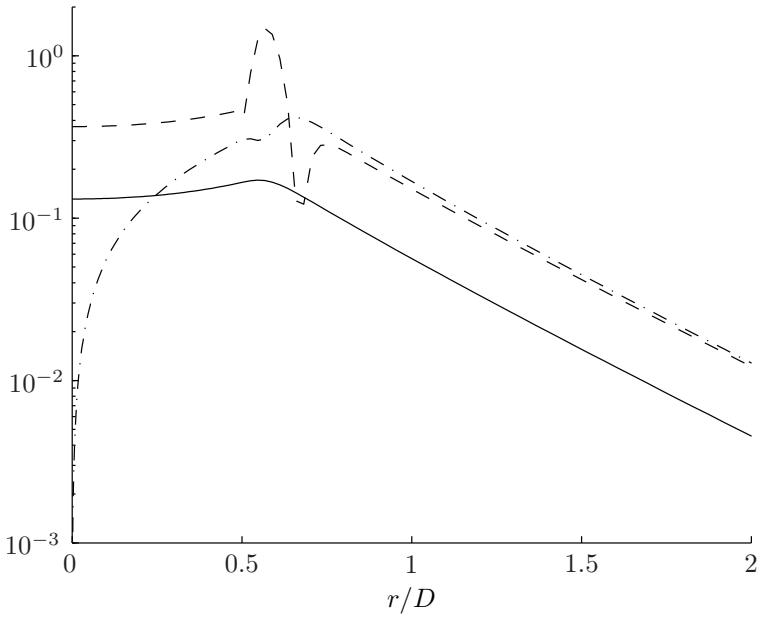

Figure 2.3: Radial decay of typical LST eigenfunctions of equation (3.1): ——, $|\hat{p}(r)|$; – – –, $|\hat{u}_x(r)|$; –·–·–, $|\hat{u}_r(r)|$. This is for $m = 0$, $St = 0.35$ and $M_\infty = 0.5$.

2.3.2 The Parabolized Stability Equations

Strictly speaking, the decomposition described in the previous section is only valid for parallel flows. Free shear layers are not parallel however. They have a finite spread rate $\varepsilon = \Delta\delta/\Delta x$, where δ is some measure of shear layer thickness. Any statistic s depending on δ will then vary in proportion to the spread rate as

$$\frac{\partial}{\partial x} s(\delta(x)) = \varepsilon s'(\delta(x)). \tag{2.55}$$

Over a distance Δx such statistics will then vary as much as $O(\varepsilon\Delta x)$. Flows with modest spread rates can then be considered to be approximately locally-parallel: the LST of the previous section can be repeated at successive cross sections of the flow to approximate the "global" eigenfunction (see section 3.2.2). This approach has been quite successful in reproducing experimental trends, as described in section 1.3.2.

The accuracy of locally-parallel concept depends not only on the spread rate of the flow but also on the wavelength $\lambda = 2\pi/\alpha_r$ of the disturbance in question: how large is $\varepsilon\lambda$? λ scales approximately inversely with frequency ω so that the locally-parallel approximation is acceptable at sufficiently high ω and increasingly strained for smaller ω.

It thus stands to reason that predictions of LST would be improved by explicitly acknowledging mean-flow divergence by retaining such terms in the linearized equations. The Parabolized Stability Equations (PSE) do just this. Here the equations are linearized about a mean flow

$$\overline{\mathbf{q}}(\mathbf{x}) = (\overline{u}_x(x,r), \overline{u}_r(x,r), 0, \overline{\rho}(x,r), \overline{T}(x,r)), \tag{2.56}$$

where the x-dependence implies that $\partial_x \overline{\mathbf{q}} \neq 0$ at all x, opposite to that in LST. As we are no longer assuming streamwise homogeneity, a separation of the form of equation (2.46) is no longer possible. However, the mean flow is still homogeneous in θ and t so that

$$\mathbf{q}(\mathbf{x}, t) = \tilde{\mathbf{q}}(x, r)\, e^{im\theta}\, e^{-i\omega t}. \tag{2.57}$$

Building on ideas from multiple-scales analysis, Bertolotti & Herbert (1991) suggested the function $\tilde{\mathbf{q}}(x,r)$ be separated into a function varying streamwise at a similar rate as the mean flow and a rapidly varying function capturing the wave-like behavior of the large-scale structure:

$$\mathbf{q}(\mathbf{x},t) = \hat{\mathbf{q}}(x,r)\, e^{i\int^x \alpha(\xi)\, d\, xi}\, e^{im\theta}\, e^{-i\omega t}. \tag{2.58}$$

This assumption represents the parabolization of the linearized equations and allows a marching solution, the x-coordinate becoming time-like. We note however that the resulting equations for the $\hat{\mathbf{q}}$ are not completely parabolic, as discussed by Li & Malik (1996, 1997). This results in constraints on the smallest allowable marching-step Δx,

$$\Delta x \geq \frac{1}{|\alpha_r|}. \tag{2.59}$$

Substituting the decomposition given by equation (2.58) into equations (2.29) - (2.34) we obtain in symbolic form the system of equations governing the evolution of shape-functions $\hat{\mathbf{q}}(x,r)$:

$$\left(\mathbf{A}(\overline{\mathbf{q}},\alpha,\omega) + \mathbf{B}(\overline{\mathbf{q}})\right)\, \hat{\mathbf{q}} + \mathbf{C}(\overline{\mathbf{q}})\, \frac{\partial \hat{\mathbf{q}}}{\partial x} + \mathbf{D}(\overline{\mathbf{q}})\, \frac{\partial \hat{\mathbf{q}}}{\partial r} = \frac{1}{Re}\mathbf{E}(\overline{\mathbf{q}})\, \hat{\mathbf{q}}. \tag{2.60}$$

Expressions for the operators $\mathbf{A}$ through $\mathbf{E}$ may be found in appendix B.

We discretize this system using fourth-order central differences in the radial direction, closing the domain with the characteristic boundary conditions of Thompson (1987). While previous studies (Herbert, 1994) have shown that boundary conditions based on asymptotic decay rates from LST are sufficient, we find the characteristic formulation to be more robust, allowing a smaller computational domain. The streamwise derivative is approximated via first-order implicit Euler differences. The solution $\hat{\mathbf{q}}_{j+1}$ at x_{j+1} is then obtained from that at x_j via the solution of

$$\left(\Delta x \left(\mathbf{A} + \mathbf{B} + \mathbf{D}\frac{d}{dr} - \frac{1}{Re}\mathbf{E}\right) + \mathbf{C}\right)_{j+1} \hat{\mathbf{q}}_{j+1} = \mathbf{C}_{j+1}\hat{\mathbf{q}}_j. \tag{2.61}$$

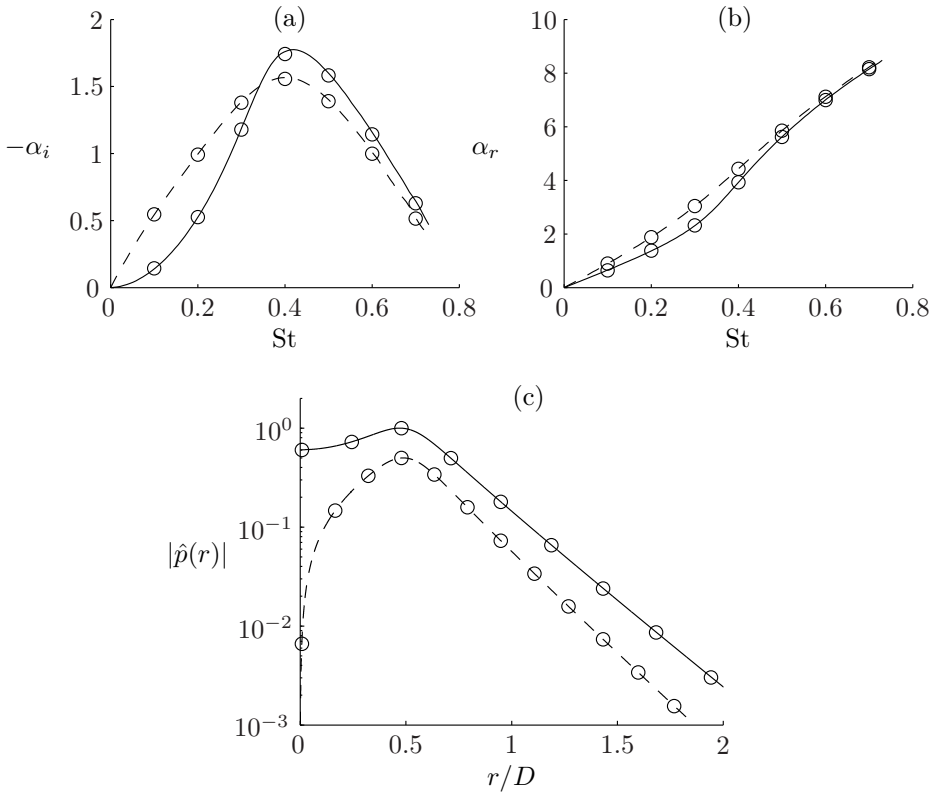

Figure 2.4: (a) Spatial growth-rates, (b) wavenumbers, and (c) eigenfunctions obtained via (——) LST and (○) PSE. Solid and dashed lines respectively correspond to azimuthal modes $m = 0$ and 1. Mean flow based on a parallel tanh profile with $M_\infty = 0.5$.

Note that if $\partial_x \overline{\mathbf{q}} = \overline{u}_r = 0$ we recover the linear stability equations. This serves as a useful check of the PSE implementation, as shown in figure 2.4.

The decomposition in equation (2.58) is ambiguous in that the streamwise development of $\mathbf{q}$ can be absorbed into either the shape-function $\hat{q}(x, r)$ or the wavenumber/growth-rate $\alpha(x)$. The PSE equations (2.60) do not impose any constraints on α; an additional condition must be supplied. In LST the logarithmic streamwise derivative of $\mathbf{q}$ is given by

$$-i\,\partial_x \log \mathbf{q} = \alpha, \tag{2.62}$$

while the corresponding PSE quantity is

$$-i\,\partial_x \log \mathbf{q} = \alpha - i\frac{\partial_x \hat{\mathbf{q}}_x}{\hat{\mathbf{q}}}. \tag{2.63}$$

The ambiguity in α can be resolved by observing that the PSE definition thereof should be a natural extension of the one in parallel flow. This cannot be accomplished pointwise but only in an integral sense, as equation (2.63) depends on the transverse coordinate r. We multiply equation (2.63) by $\hat{\mathbf{q}}^*\hat{\mathbf{q}}\,r$, integrate over the radial domain and divide by the integrated energy of $\hat{\mathbf{q}}$:

$$\frac{\int_0^\infty -i|\hat{\mathbf{q}}|^2\partial_x \log(\mathbf{q})\,r\,dr}{\int_0^\infty |\hat{\mathbf{q}}|^2\,r\,dr} = \alpha - i\frac{\int_0^\infty \hat{\mathbf{q}}^*\partial_x\hat{\mathbf{q}}\,r\,dr}{\int_0^\infty |\hat{\mathbf{q}}|^2\,r\,dr}. \tag{2.64}$$

If we can now choose α such that

$$\int_0^\infty \hat{\mathbf{q}}\frac{\partial\hat{\mathbf{q}}^*}{\partial x}\,r\,d\,r = 0, \tag{2.65}$$

the definition of α for the PSE becomes

$$\alpha = -i\frac{\int_0^\infty -i|\hat{\mathbf{q}}|^2\partial_x \log\mathbf{q}\,r\,dr}{\int_0^\infty |\hat{\mathbf{q}}|^2\,r\,dr}. \tag{2.66}$$

This includes equation (2.62) as a special case and provides an algorithm for updating α^{j+1} as:

$$\alpha_{n+1}^{j+1} = \alpha_n^{j+1} - \frac{i}{\Delta x}\frac{\int_0^\infty(\hat{\mathbf{q}}_n^{j+1})^*(\hat{\mathbf{q}}_n^{j+1}-\hat{\mathbf{q}}^j)\,r\,dr}{\int_0^\infty|\hat{\mathbf{q}}_n^{j+1}|^2\,r\,dr} \tag{2.67}$$

We now iterate between equation (2.61) and equation (2.67) to advance the solution from x_j to x_{j+1}.

The constraint in equation (2.65) removes any exponential factor from the shape functions $\hat{\mathbf{q}}$, ensuring their slow (algebraic) streamwise variation. This can be seen by viewing the constraint as an inner product:

$$\langle\hat{\mathbf{q}},\partial_x\hat{\mathbf{q}}\rangle = \int_0^\infty \hat{\mathbf{q}}\frac{\partial\hat{\mathbf{q}}^*}{\partial x}\,r\,dr. \tag{2.68}$$

If the projection of $\partial_x\hat{\mathbf{q}}$ onto $\hat{\mathbf{q}}$ is nonzero then $\partial_x\hat{\mathbf{q}} = \gamma\hat{\mathbf{q}} + \boldsymbol{\beta}$, where $\gamma \neq 0$ is a constant and $\boldsymbol{\beta}$ satisfies $\langle\hat{\mathbf{q}},\boldsymbol{\beta}\rangle = 0$. The normalization condition becomes

$$\langle\hat{\mathbf{q}},\gamma\hat{\mathbf{q}}+\boldsymbol{\beta}\rangle = \gamma^*||\hat{\mathbf{q}}||^2 + \langle\hat{\mathbf{q}},\boldsymbol{\beta}\rangle = \gamma^*||\hat{\mathbf{q}}||^2 = 0. \tag{2.69}$$

But $||\hat{\mathbf{q}}|| \neq 0$ so that we must have $\gamma = 0$. In essence, γ has been absorbed into $i\alpha$: $\hat{\mathbf{q}}$ can only change algebraically.

Initial conditions $(\hat{\mathbf{q}}, \alpha)_{x_0}$ optimally come from a solution which includes the local effects of flow spread. Day *et al.* (2001) used asymptotic expansions to this end, but found minor benefits over the LST solution based on the initial profiles $\overline{u}_x(x_0, r)$ and $\overline{\rho}(x_0, r)$. In this work we also use the solution to equation (2.50) as an initial condition. Before starting the marching procedure, we take the additional step of solving system (2.61) without non-parallel terms, but including viscous terms. This allows the linear stability solution to adjust to the effects of viscosity and reduces transients in the marching solution.

2.4 The Proper Orthogonal Decomposition

We briefly outline the POD procedure as introduced in the context of fluid mechanics by Lumley (1967) and used by numerous authors since. Given a set of N instantaneous field measurements of pressure or velocity (or any other variable), $\boldsymbol{u}_k$, what is the "best" low-dimensional representation of these measurements?

Imagine a cloud of randomly placed points (measurements) of zero mean in the (x, y) plane. Since the pairs (x_j, y_j) are randomly distributed, the cloud will be disc-shaped, no bias towards either the x- or the y-axis. In other words, neither axis captures a greater proportion of the signal variance . If we now introduce a relationship between x and y such that the cloud is stretched into an ellipse with the major axis aligned with the x-axis, then the x-axis captures, or explains, a greater portion of the total variance than does the y-axis. Thus, if we are interested in a low-dimensional approximation of the data by discarding either coordinate, we are better off retaining the x-coordinate of each measurement. This idea can be generalized to any linear vector space, the "axes" now becoming functions $\boldsymbol{\phi}$. The POD is an automated way of finding these successive axes of decreasing variance or energy.

Mathematically, the problem is to determine the function $\boldsymbol{\phi}$ having maximal mean-squared projection upon the set of measurements. $\boldsymbol{\phi}$ can then be interpreted as the most likely occurrence, or

the expected value of the $\mathbf{u}_k$, and is a linear combination thereof:

$$\boldsymbol{\phi^j} = \sum_{k=1}^{N} c_k^j \mathbf{u}_k. \tag{2.70}$$

Taking the inner product of equation (2.70) with itself,

$$\begin{aligned} \langle \boldsymbol{\phi}^j, \boldsymbol{\phi}^j \rangle &= \langle \sum_k c_k^j \mathbf{u}_k, \sum_l c_l^j \mathbf{u}_l \rangle \\ &= \sum_k \sum_l c_k^j c_l^{j*} < \mathbf{u}_k, \mathbf{u}_l > \\ &= \sum_l c_l^{j*} (\mathbf{M}\mathbf{c}^j)_l \\ &= \mathbf{c}^{j*} \mathbf{M} \mathbf{c}^j, \end{aligned} \tag{2.71}$$

where $\mathbf{M}_{kl} = \langle \mathbf{u}_l, \mathbf{u}_k \rangle$. We wish to optimize $\langle \boldsymbol{\phi}^j, \boldsymbol{\phi}^j \rangle = ||\boldsymbol{\phi}^j||^2$ over $\mathbf{c}^j$ while keeping the latter finite, $\mathbf{c}^{j*}\mathbf{c}^j = 1$, say. We thus add a Lagrange multiplier λ,

$$||\boldsymbol{\phi}^j||^2 = \mathbf{c}^{j*} \mathbf{M} \mathbf{c}^j - \lambda^j (\mathbf{c}^{j*} \mathbf{c}^j - 1). \tag{2.72}$$

Taking derivatives with respect to $\mathbf{c}^j$ we obtain

$$\mathbf{M}\mathbf{c}^j = \lambda^j \mathbf{c}^j. \tag{2.73}$$

The Lagrange multipliers λ are the eigenvalues, and the coefficients $\mathbf{c}^j$ the eigenvectors of the covariance-matrix $\mathbf{M}$. Note that since $\mathbf{M}$ is Hermitian ($\mathbf{M}_{ij} = \mathbf{M}_{ji}^*$) the eigenvalues λ^j are real and eigenvectors $\mathbf{c}^j$ corresponding to different eigenvalues are orthonormal. $\mathbf{M}$ is also positive definite so that all the eigenvalues are positive. They represent modal-energy as from equation (2.71),

$$||\boldsymbol{\phi}^j||^2 = \mathbf{c}^{j*} \mathbf{M} \mathbf{c}^j = \mathbf{c}^{j*} \lambda^j \mathbf{c}^j = \lambda^j, \tag{2.74}$$

since $\mathbf{c}^{j*}\mathbf{c}^j = 1$. We obtain the POD-modes $\boldsymbol{\phi}^j$ by substituting the eigenvector $\mathbf{c}^j$ into equa-

tion (2.70). The basis functions $\boldsymbol{\phi}^j$ are an optimal representation of the set $\mathbf{u}_k$ in the sense that projection onto other basis of the same dimension will result in greater error. For homogeneous directions it is well known that the Fourier basis is optimal and must therefore equal the POD basis. In this sense, the POD basis be considered a natural extension of the Fourier basis to non-homogeneous directions.

The choice of inner product in equation (2.71) is problem specific and depends on geometry as well as the variables of interest. Different inner products can lead to different energy decomposition by azimuthal mode, for example. This is discussed further in chapter 3 and 4.

2.5 Experimental Data

The experimental jets analyzed in this thesis were probed via stereo Particle Image Velocimetry (PIV) and a caged microphone array. These are described below.

2.5.1 Velocimetry

We investigated two pairs of heated and cold round jets at acoustic Mach numbers M_∞ of 0.5 and 0.9, and a single cold serrated (chevron) jet at $M_\infty = 0.9$. The flow conditions are listed in table 2.1. Velocity data were obtained from stereo PIV measurements conducted by Bridges & Wernet (2003) in the Small Hot Jet Acoustic Rig (SHJAR) at the NASA Glenn Research Center.

Measurements were made both in the streamwise (*i.e.*, x-y) and cross-stream (y-z) planes, with streamwise and cross-stream resolution of $0.04D$ and $0.03D$, respectively. The round jets analyzed in this study were measured in the streamwise plane while the serrated jet was measured in cross-stream planes to capture its azimuthal structure. Mean flow field surveys for the round jets are shown in figure 2.5, and figure 4.3 for the serrated jet. The mean flows consist of an ensemble average of 200 instantaneous measurements taken $0.1s$ apart. These measurements can be considered to be uncorrelated as the time between shots far exceeds the eddy pass-through time (the slowest jet travels roughly $350D$ in $0.1s$).

Set Point	M_∞	T_{jet}/T_∞	Re	PIV for Round/Serrated?
3	0.5	0.96	7×10^5	Yes/No
23	0.5	1.76	2×10^5	Yes/No
7	0.9	0.85	16×10^5	Yes/Yes
27	0.9	1.76	4×10^5	Yes/No

Table 2.1: Flow conditions investigated in this study. Set points are as defined by Tanna (1977).

A detailed review of the PIV-camera setup, flow seeding, and data processing may be found in Bridges & Wernet (2003).

Temperature measurements were not available and were estimated from velocity via the Crocco-Busemann relation,

$$\frac{T}{T_\infty} = -\frac{\overline{u}_x^2}{2} + \left(\frac{1}{\gamma - 1}\left(\frac{T_{jet}}{T_\infty} - 1\right) + \frac{M_\infty^2}{2}\right)\frac{\overline{u}_x}{M_\infty} + \frac{1}{\gamma - 1}. \tag{2.75}$$

Transverse velocity profiles were estimated from the mass-conservation equation.

2.5.2 Pressure Measurements

Pressure measurements were obtained from a caged microphone array, shown in figure 2.6, at NASA Glenn's SHJAR facility. This array consists of thirteen concentric rings arranged on a conically expanding surface with the cone angle (11.2°) set to be slightly greater than the spread-angle of the jet shear layer. Each ring carries six microphones distributed evenly around the perimeter, allowing the accurate resolution of the most energetic azimuthal modes, $m = 0 - 2$. To minimize aliasing, each ring is shifted 30°relative to the adjacent ring. The cone angle is fixed so that the relative angle between the jet and the array varies slightly with the jet operating conditions, the effects of which are discussed in section 3.4.1. The radius of the array was chosen such as to place the microphones in the linear-hydrodynamic regime, where pressure fluctuations are largely hydrodynamic, as shown in figure 3.1 and discussed in section 3.1.

An extensive review of the array design, experimental setup, and data sampling and processing may be found in Suzuki & Colonius (2006).

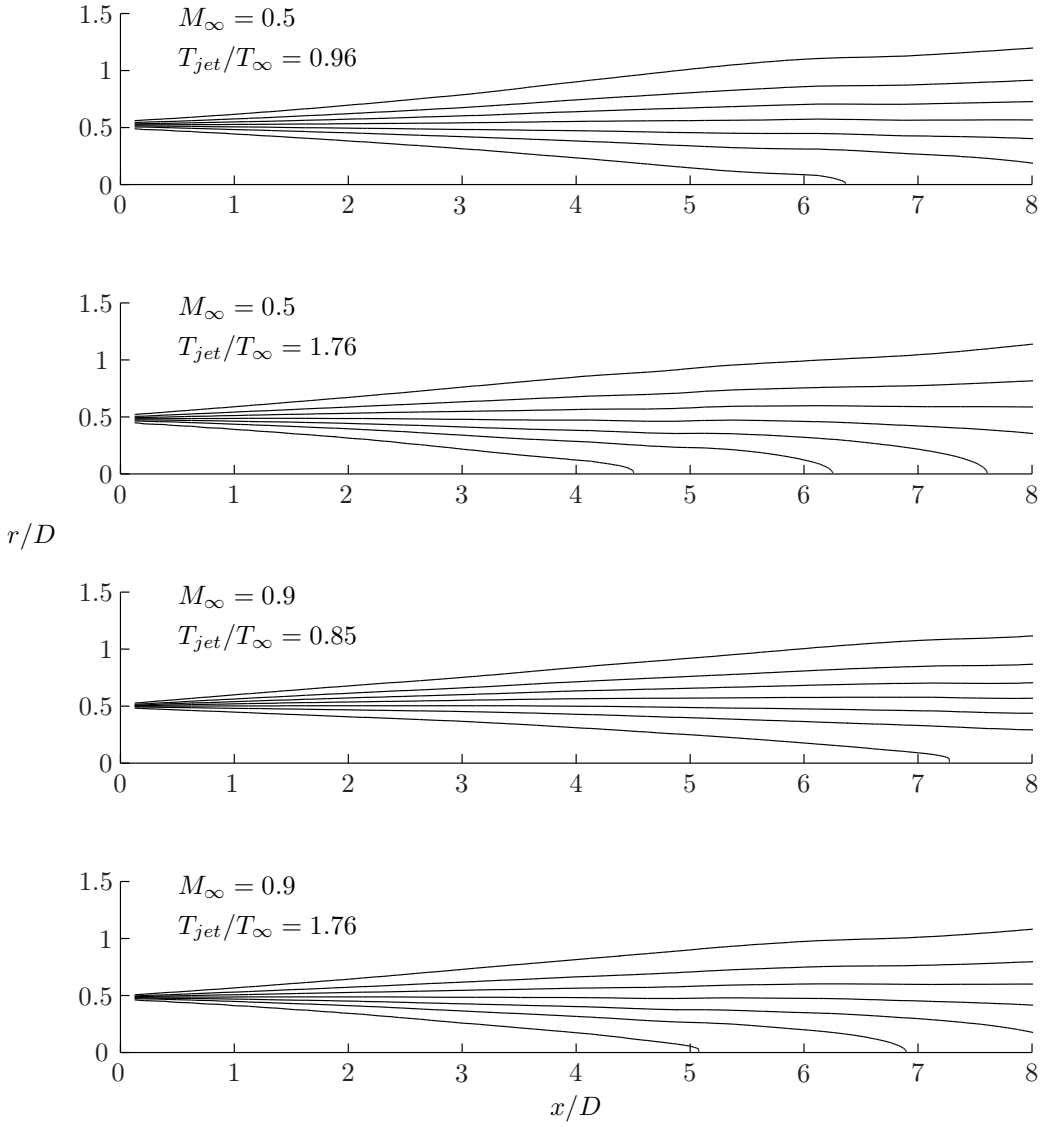

Figure 2.5: Contours of axial velocity $\overline{u}_x/U_{jet}$ for the four jets in table 2.1. Contours are in equal increments from 0.1 through 0.99.

Figure 2.6: The Small Hot Jet Acoustic Rig (SHJAR) and Hydrodynamic Array at the NASA Glenn Research Center.

Chapter 3

Instability Wave Models of Large-Scale Pressure Fluctuations

3.1 Introduction

Large-scale coherent structures in jets have traditionally been modeled based on the Kelvin-Helmholtz instability of the jet shear layer. Such efforts have been successful, particularly for forced jets at relatively low Reynolds numbers (*e.g.*, Mattingly & Chang, 1974). At unforced conditions (*i.e.*, for "natural jets"), such disturbances are correlated over shorter spatial and temporal length scales, making their unbiased detection challenging. This is further confounded at higher Reynolds numbers where the relative energy associated with large-scale coherent structures is diminished due to increased production of fine scale turbulence. This can render the decomposition of turbulence ambiguous at best and meaningless at worst.

But this is only the case in regions of intense turbulence, such as in the shear layer. As noted by Suzuki & Colonius (2006), pressure fluctuations arising from different sources (*e.g.*, instability waves and quadrupoles) have different spatial decay characteristics. While such disturbances might not be separated in a unique manner at one location, they might be at another. This is illustrated in figure 3.1, which shows the radial decay of pressure fluctuations in a turbulent jet. The figure shows two crossover points, the first from a region dominated by nonlinear fluctuation levels to an outer, linear region where pressure levels fall off exponentially with radius. These regions are collectively referred to as the hydrodynamic regime, alluding to the mostly non-propagative character of the

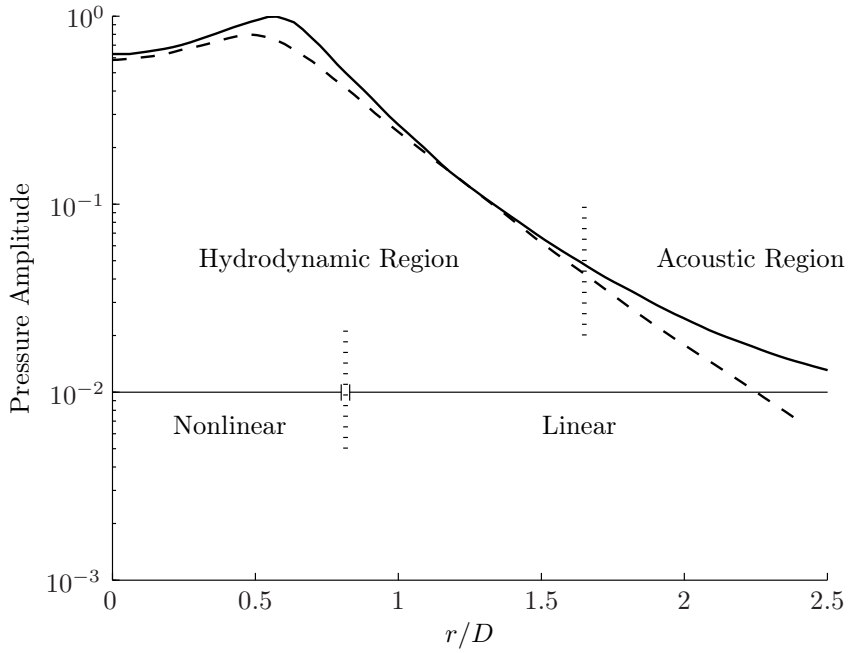

Figure 3.1: Radial distribution of pressure fluctuations of the axisymmetric mode in a turbulent jet. Shown is a hypothetical rms-pressure distribution (——), along with a locally-parallel eigenfunction from linear stability analysis (- - -). Indicated are the regions demarcated by type of dominating pressure fluctuations: nonlinear/linear hydrodynamic (evanescent) and acoustic.

resident fluctuations. The next crossover is from the linear hydrodynamic to the acoustic region in which pressure fluctuations propagate at the ambient speed of sound while decaying in inverse proportion to radius.

Suzuki & Colonius recognized that the signatures of convected large-scale coherent structures should be embedded in, and dominate the linear hydrodynamic region. Placing microphones in this region (where the two lines are aligned in figure 3.1) might thus allow their indirect detection and study. In particular, their amplitude and phase-angle might be deduced by fitting a model to the measured data. Using the caged microphone array described in section 2.5.2, Suzuki & Colonius made such measurements and compared them to a locally-parallel linear stability model. They obtained excellent agreement near the most unstable frequency (see figure 3.8 and discussion in section 3.3.2). The agreement at sub-peak frequencies was not as favourable however, particularly for the axisymmetric mode. This is at least in part due to the nature of the locally-parallel flow assumption (discussed in sections 1.3.2 and 2.3.2) and as such the predictions should be amenable

to improvement via the inclusion of non-parallel effects.

The Parabolized Stability Equations (PSE), introduced by Bertolotti & Herbert (1991), represent a refinement of the locally-parallel approach whereby both non-parallel and non-linear effects can be retained in the analysis of slowly spreading, convectively unstable flows such as boundary layers (Bertolotti & Herbert, 1991; Bertolotti *et al.*, 1992; Chang *et al.*, 1993), planar mixing layers (Day *et al.*, 2001; Cheung & Lele, 2009) and jets (Balakumar, 1998; Yen & Messersmith, 1998; Malik & Chang, 2000; Ray *et al.*, 2009; Gudmundsson & Colonius, 2009).

The PSE have been used successfully to predict the far-field behavior of supersonic laminar jet flows. Subsonic conditions however still represent a challenge for instability-based methods as the far field is absent from the solution, even for the PSE. The near field is well modeled, though, allowing the inner instability solution to be coupled with projection methods (Balakumar, 1998; Cheung & Lele, 2009) to deliver reasonable far field approximations, at least in qualitative terms. Limitations on far field predictions are however not a concern in the current work, as our immediate scope is the near field of large scale coherent structures and their modeling via the Kelvin-Helmholtz instability of the inflectional mean flow profiles.

In section 3.2 we describe some of the data-processing procedures used in this thesis. In section 3.3 we discuss the effects of mean flow divergence, both in terms of stability characteristics and comparison to experiment. In section 3.4 we discuss the nature of the pressure measurements in this study and our application of the proper orthogonal decomposition. In section 3.5 we describe the effects of filtering measurements via the POD, and compare these with the prediction of PSE. Finally, in section 3.6 we summarize our findings.

3.2 Preliminaries

3.2.1 Processing of PIV Data

To avoid numerical issues (stemming from non-smooth measurements) in the solution of the PSE system (2.61) we fit the PIV mean flow with a Gaussian profile similar to that used by Troutt & McLaughlin

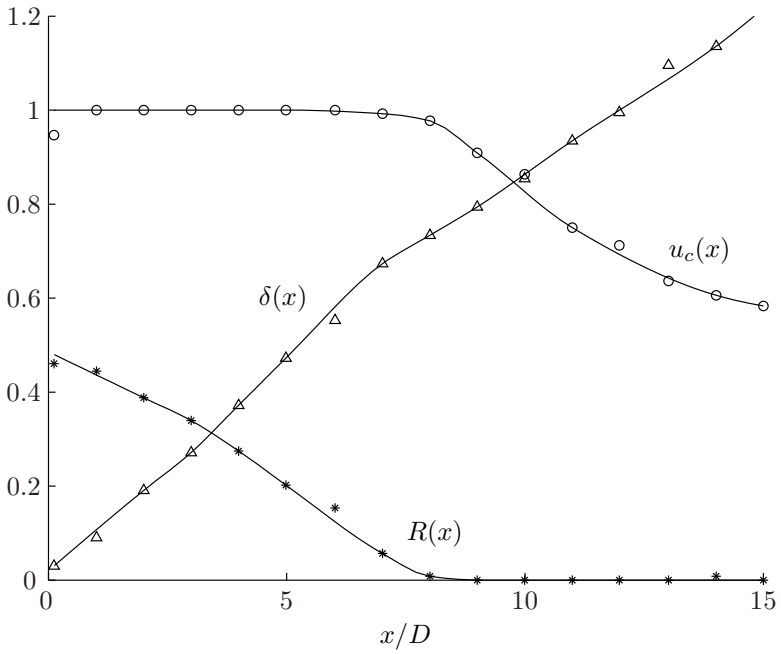

Figure 3.2: Profile parameters $R(x), \delta(x)$ and $u_c(x)$ as determined from PIV measurements (symbols) of the cold $M_\infty = 0.9$ jet and fitted with a cubic polynomial (lines) to ensure smooth axial variation of $\overline{u}_x$.

(1982) and Tam & Burton (1984),

$$\frac{\overline{u}_x}{U_{jet}} = \begin{cases} 1 & \text{if } r < R(x) \\ u_c(x) \exp\left(-\frac{(r-R(x))^2}{\delta(x)^2}\right) & \text{otherwise.} \end{cases} \tag{3.1}$$

The profile parameters $R(x), \delta(x)$, and $u_c(x)$ are determined from the PIV data via least-squares: we define a 3D parameter-grid and search over this space for the best solution. To ensure smooth axial variation of $\overline{u}_x$ we fit the profile parameters with a cubic polynomial, an example of which is shown in figure 3.2 for the cold $M_\infty = 0.9$ jet. Figure 3.3 shows the excellent fits so obtained for this jet; similar results are obtained at other flow conditions. Analogous results can be obtained in the core region with the hyperbolic-tangent function (Suzuki & Colonius, 2006) but this match deteriorates as the jet takes on a Gaussian shape further downstream.

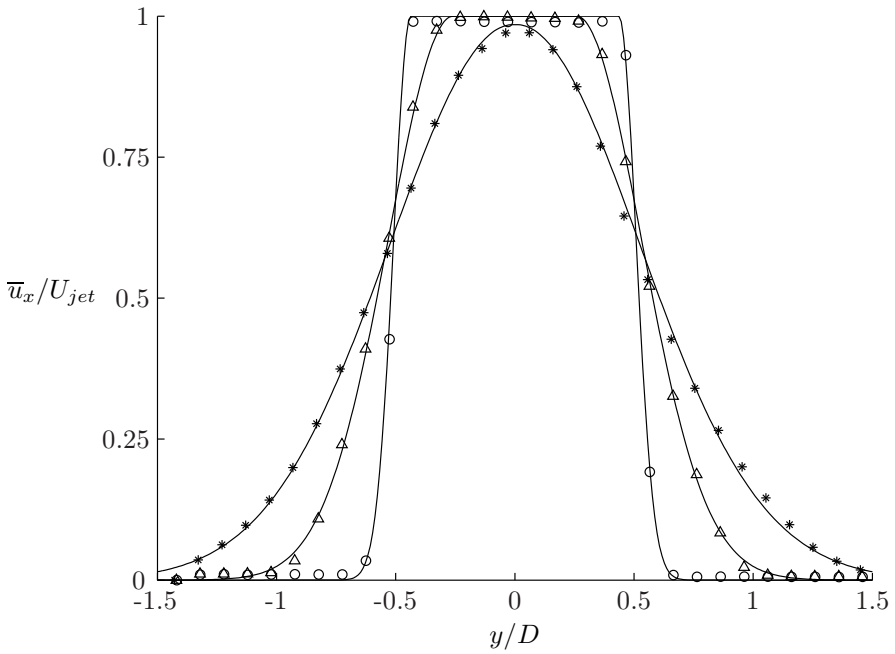

Figure 3.3: PIV measurements (symbols) of axial velocity for the cold $M_\infty = 0.9$ jet, matched with the profile of equation (3.1) (lines). Shown are axial stations $x/D = 1.0$ (○), 4.0 (△), and 8.0 (∗). Every fourth data point is shown.

3.2.2 Normalization of Predictions

In what follows we respectively denote measured and computed quantities with upper and lowercase letters. The time series $P(x, r, \theta, t)$ from the 78-microphone array is decomposed into its azimuthal and temporal harmonics:

$$P(x, r, \theta, t) = \sum_m \int \widetilde{P}_{m\omega}(x, r)\, e^{im\theta}\, e^{-i\omega t}\, d\omega. \tag{3.2}$$

We compare $\widetilde{P}_{m\omega}$ with the PSE equivalent,

$$\widetilde{p}_{m\omega} = A_{m\omega}\, \hat{p}_{m\omega}(x, r) e^{i\int^x \alpha_{m\omega}(\xi)\, d\xi}, \tag{3.3}$$

where the complex number $A_{m\omega}$ represents the initial amplitude and phase of the PSE solution $\hat{\mathbf{q}}$[1].

The system governing the evolution of $\hat{p}_{m\omega}$ is linear and does not depend on, or predict $A_{m\omega}$.

[1]Note that the shape functions are first (arbitrarily) normalized such that $\hat{u}_r$ is real-valued at $r = 1/2$ and $\max_r(\hat{\mathbf{q}}) = 1$.

This we determine from the measured data. Suzuki & Colonius used a beam-forming procedure whereby $A_{m\omega}$ was chosen to maximize the phase-match between the microphone data and their LST prediction. We determine $A_{m\omega}$ via amplitude-matching, choosing $A_{m\omega}$ as that minimizing the error defined as

$$J(A_{m\omega}) = \sum_{j=1}^{N_{ring}} |\widetilde{P}^j_{m\omega} - \widetilde{p}^j_{m\omega}|^2, \tag{3.4}$$

where $\widetilde{P}^j_{m\omega}$ and $\widetilde{p}^j_{m\omega}$ respectively denote measurements and predictions at $x = x_j$, and N_{ring} denotes the number of microphone rings. This results in the estimate

$$A_{m\omega} = \frac{\sum_{j=1}^{N_{ring}} |\widetilde{p}^j_{m\omega}\widetilde{P}^j_{m\omega}|}{\sum_{j=1}^{N_{ring}} |\widetilde{p}^j_{m\omega}|^2}, \tag{3.5}$$

Phase-matching is in general expected to return lower estimates of $A_{m\omega}$ as it attempts to filter out contributions from events uncorrelated with the instability waves in the flow. We choose the simpler amplitude-matching as we are primarily interested in comparing the shapes of measurements and predictions, a favourable match indicating dominance of instability waves in the pressure signal.

The LST solution is computed at various axial stations x, assuming locally-parallel flow. To emulate the PSE expansion in equation (3.3) we construct a "global" LST eigenfunction

$$\widetilde{p}_{m\omega} = A_{m\omega} \frac{\hat{p}_{m\omega}(r,|x)}{\max_r |\hat{p}_{m\omega}(r,|x)|} e^{i\int^x \alpha_{m\omega}(\xi)\, d\xi}, \tag{3.6}$$

where $\hat{p}_{m\omega}(r,|x)$ and $\alpha_{m\omega}(x)$ are respectively the local LST eigenfunction and eigenvalue for mode (m,ω), computed at axial station x.

3.3 Effects of Mean Flow Divergence

Using the cold $M_\infty = 0.5$ jet as an illustrative example, we discuss some of the effects of mean flow divergence in the following sections.

3.3.1 Stability Characteristics

Figure 3.4 shows growth-rates $-\alpha_i$ and streamwise wavenumbers α_r for the cold $M_\infty = 0.5$ jet, computed via both LST and PSE. The initial condition for the PSE simulation is computed using the locally-parallel assumption with viscous terms included (see section 2.3.2), explaining why the two agree closely near the nozzle, with PSE growth-rates being slightly lower due to viscous damping.

Significant differences appear as the two solutions evolve downstream. Most notable is the destabilizing effect of mean flow divergence: growth-rates are increased and the neutral point (where $\alpha_i = 0$) is offset downstream. The degree to which this occurs depends on the azimuthal wavenumber m, with higher-m modes being increasingly affected. Streamwise wavenumbers are similarly increased, although the dependence on azimuthal wavenumber seems reversed as compared to that of the growth-rate. These results are consistent with those of Malik & Chang (2000) who studied a low Reynolds number supersonic jet. Bertolotti *et al.* (1992) also found similar effects in the incompressible Blasius boundary layer.

The Rayleigh equation (2.50) and the more general PSE equations (2.60) differ locally by non-parallel terms such as $\partial_x \overline{u}_x$ and $\overline{u}_r$. They also differ globally in that history effects (the accumulation of upstream influences) are included by the PSE[2]. One might then wonder whether the destabilization and shortening of unstable waves (as α_r is larger) is a local or a global effect. This can be addressed by removing all non-parallel terms from the PSE, retaining only the history effect. The results in figure 3.5 indicate that this alteration has a limited impact, showing that history effects, rather than the local effects of additional shear, are largely responsible for the observed differences between LST and PSE. Figure 3.5 shows an $m = 0$ case at $St = 0.35$ but we note that similar effects are observed at other conditions.

The shape-functions $\hat{p}$ play a vital role in determining the spatial distribution of pressure fluctuations. Figure 3.6 shows a comparison of shape-functions computed via LST and PSE, at $St = 0.35$ and cross-section $x/D = 2$. Significant differences are observed away from the shear layer, both within the jet core and in the far field, particularly for the $m = 0$ mode. This is a direct consequence

[2]The current implementations of the LST and PSE further differ by the inclusion of viscous effects by the latter. This does not bear on the current discussion however.

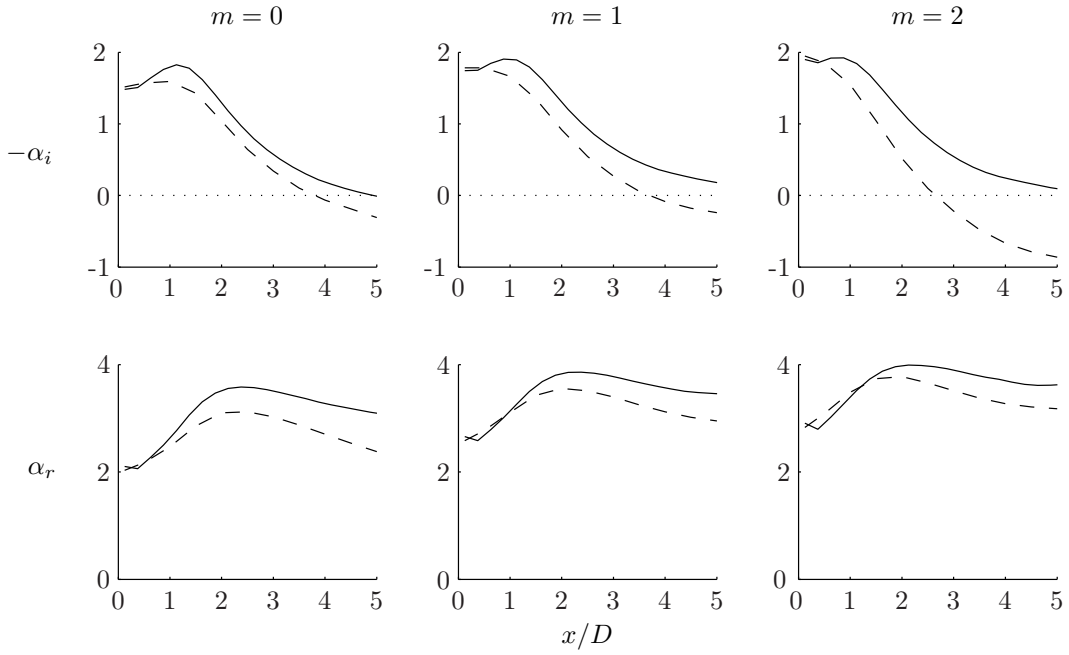

Figure 3.4: growth-rates and wavenumbers for the cold $M_\infty = 0.5$ jet: – – –, LST; ——, PSE. Azimuthal wavenumbers $m = 0$-2 at frequency $St = 0.35$.

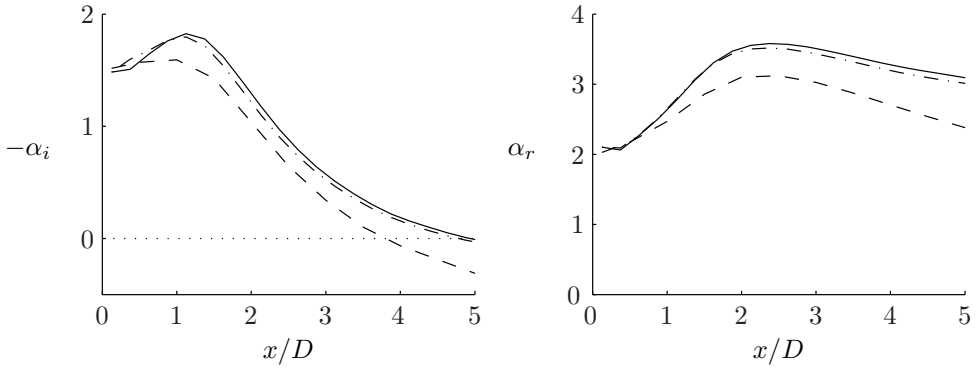

Figure 3.5: Growth-rates $-\alpha_i$ and wavenumbers α_r for the cold $M_\infty = 0.5$ jet: – – –, LST; ——, PSE; –·–·–PSE with non-parallel terms zeroed. Azimuthal wavenumber $m = 0$ at frequency $St = 0.35$.

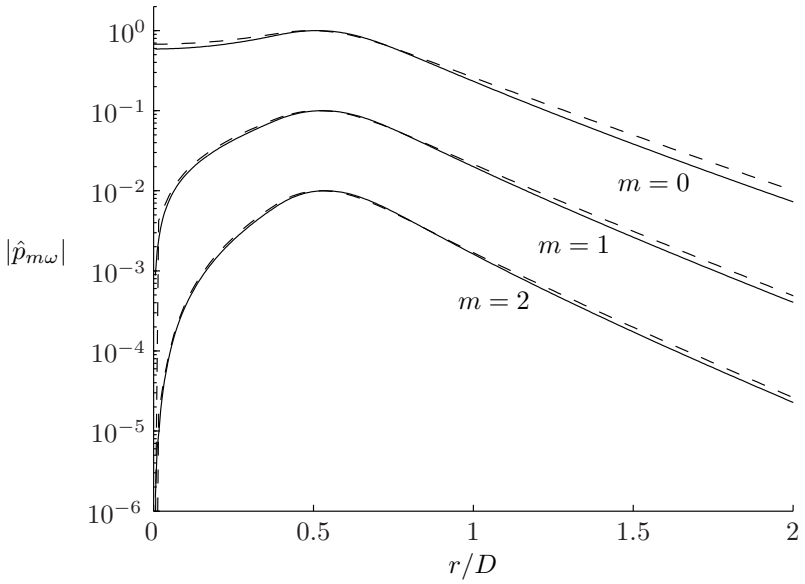

Figure 3.6: Amplitude of eigenfunctions $\hat{p}_{m\omega}$ for the cold $M_\infty = 0.5$ jet, computed via (- - -) LST and (——) PSE, at azimuthal wavenumbers $m = 0$-2, frequency $St = 0.35$ and cross-section $x/D = 2$. Note that $\hat{p}_{m\omega}$ is arbitrarily normalized and is shifted here for readability.

of PSE's larger α_r-estimate, on which the asymptotics in equations (2.52) and (2.53) depend.

The next step in the analysis is to look at the pressure variable $\widetilde{p}_{m\omega}$, defined in equation (3.3). This variable combines the effects of α and $\hat{p}$, giving the physical-space distribution of pressure. Figure 3.7 shows $|\widetilde{p}_{m\omega}|$ computed via the two methods, along two constant radii. Disturbances close to the shear layer (the $r/D = 0.5$ curve) are greatly amplified under the PSE approximation. Further out from the axis, the faster decay of the PSE shape-function partially compensates for the increased growth-rate, particularly for $m = 0$. Also note the different saturation location estimates. LST undershoots these in all cases and increasingly so with higher m. This is a consequence of LST's premature growth-rate decay and passage through the neutral point.

Aside from the more realistic physical modeling of the PSE, the method has some numerical advantages over the LST. The computation of neutral and stable modes in particular is no issue for the PSE. In LST however, special care has to be taken near $\alpha_i = 0$, where $\alpha\,\overline{u}_x(r) - \omega$ can vanish at some $r = r_c$, called the critical layer (Tam & Morris, 1980). r_c is a regular singular point of equation (2.50) and requires a branch cut to be made in the complex r plane to obtain a continuous solution. This procedure, described in section A.1.2, was carried out in the LST computation of

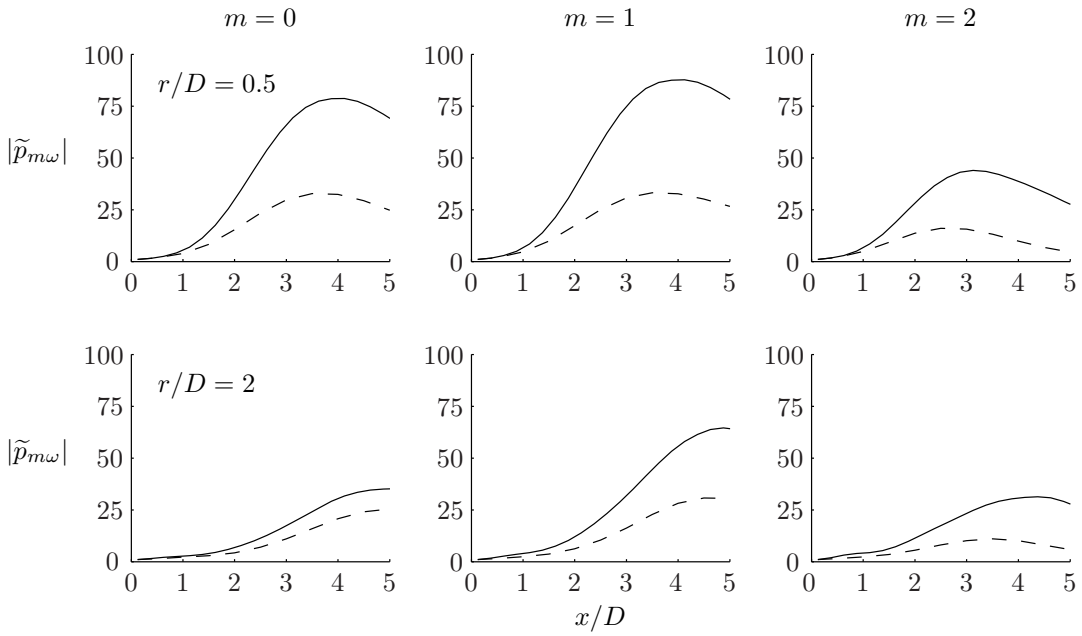

Figure 3.7: Pressure amplitude along constant radii for the cold $M_\infty = 0.5$ jet: - - -, LST; ——, PSE, at frequency $St = 0.35$. All amplitudes scaled so that $|\widetilde{p}_{m\omega}(x_0, r)| = 1$.

neutral and stable modes in this thesis. Even when taking such precautions the calculation cannot be carried on indefinitely in the streamwise direction, as the path deformation required becomes comparable to the jet diameter. This is why LST computations are terminated at $x/D = 5$ in figure 3.8.

3.3.2 Comparison with Experiments

A subset of the LST predictions $\widetilde{p}_{m\omega}$ of Suzuki & Colonius (2006) is reproduced in figure 3.8 and compared with their pressure measurements $\widetilde{P}_{m\omega}$. This figure corresponds to figure 12 in their paper. Note however that the current LST results differ slightly from those of Suzuki & Colonius, for two reasons. Firstly, they use a hyperbolic-tangent function to approximate the PIV mean flow while we use the Gaussian function described in section 3.2.1. The two approaches result in very similar approximations near the nozzle; we choose the more general Gaussian shape as we are interested in extending their predictions beyond the potential core, into the developed region. Secondly, our amplitudes $A_{m\omega}$ are generally higher as we employ amplitude-matching rather than phase-matching.

The latter approach results in lower amplitudes as it attempts to filter out contributions from events uncorrelated with the instability waves in the flow. We choose the simpler amplitude-matching as we are primarily interested in comparing the shapes of measurements and predictions, a favourable match indicating dominance of instability waves in the pressure signal.

Figure 3.8 shows the evolution of pressure amplitude and phase angle for the cold $M_\infty = 0.5$ jet at azimuthal wavenumbers m = 0-2 and frequencies St = 0.25, 0.35, and 0.50. Amplitude predictions generally improve with increasing frequency, at least within the range shown here (but see section 3.5.1). Compared with the data, LST growth-rates seem underpredicted, particularly at low frequencies. The $m = 1$ predictions do fairly well, however, and do not seem to suffer much from the locally-parallel assumption employed in the LST, at least not at and above the most unstable frequency. The axial location of saturation is captured in most cases (note that these measurements are taken on the surface of a cone, causing saturation to occur at an earlier streamwise location than would be recorded on a cylinder as in figure 3.7).

The phase-angle predictions at low frequencies are excellent for all azimuthal wavenumbers. Upstream and downstream of saturation, the phase-angle measurements level off, however, the region of good match becoming increasingly narrower with frequency. This is due to the effects of acoustic disturbances, discussed below.

Figure 3.9 shows the evolution of pressure amplitude for the same flow condition, this time including the predictions of PSE. Drastic improvements are offered by the PSE, particularly at lower frequencies. This is at least in part due to the higher growth-rate estimates of the PSE, as discussed in the previous section. Note however the differing improvements for the different azimuthal modes: $m = 0$ and $m = 2$ are significantly impacted, $m = 1$ only mildly so. The $m = 1$ mode is of course already reasonably well predicted by LST, leaving less room for improvement. But why does the LST do worse for $m = 0$ and $m = 2$, skipping over $m = 1$? Clearly this has to do with mean flow divergence and we suggest the following causes.

The $m = 0$ mode of LST is adversely affected by non-parallelism due to its boundary condition at the axis. As mean flow gradients vanish near the axis, the Rayleigh equation (2.50) is reduced to

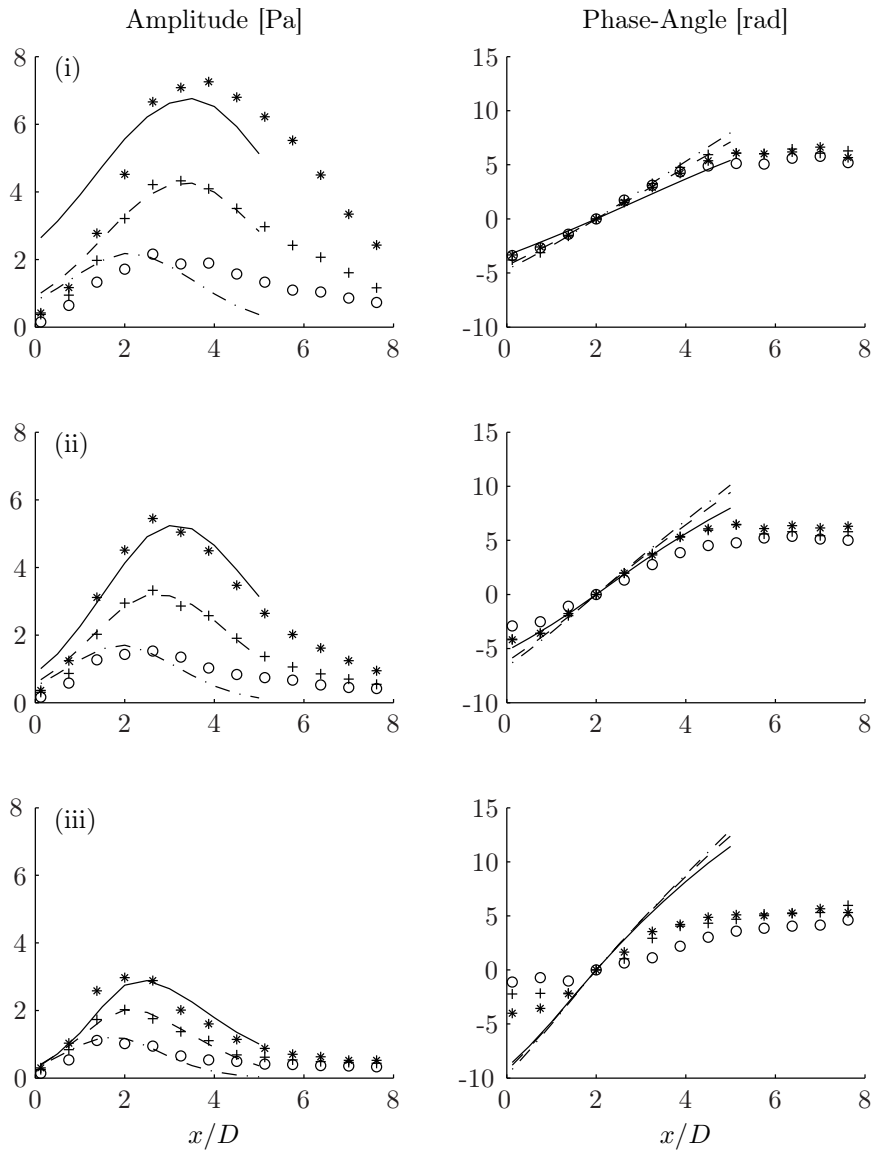

Figure 3.8: Pressure amplitude and phase-angle along the microphone array for the cold $M_\infty = 0.5$ jet. Measurements denoted by symbols and predictions by lines: $*$,——, $m = 0$; $+$, - - -, $m = 1$; $\circ$, -·-·-, at frequencies (i) $St = 0.25$; (ii) $St = 0.35$; (iii) $St = 0.5$.

Bessel's equation,

$$\frac{1}{r}\frac{d}{dr}\left(r\frac{d\hat{p}}{dr}\right) - \left(\frac{m^2}{r^2} + \alpha^2 - \overline{\rho}(\alpha\, M_\infty - \omega)^2\right)\hat{p} = 0. \tag{3.7}$$

As $r \to 0$ this becomes

$$r^2\frac{d^2\hat{p}}{dr^2} + r\frac{d\hat{p}}{dr} - m^2\hat{p} = 0, \tag{3.8}$$

also called Euler's differential equation, with solution $\hat{p} = Cr^{|m|}$ for any constant C. Thus, $m = 0$ is the only non-vanishing mode at the axis[3] (as can be seen in figure 3.6). This mode is sensitive to and scales with the nozzle diameter D, which is much larger than the shear layer thickness δ, at least in the core region. These waves will be longer (have smaller streamwise wavenumbers α_r) and experience greater mean flow variance over a wavelength as compared to the shorter $m \neq 0$ waves (of the same frequency) and hence will be more sensitive to non-parallel effects. These arguments apply more to the wavenumber α_r than the growth-rate $-\alpha_i$, as the latter still depends heavily on the shear. This can be seen in figure 3.4: out of $m = 0$ to 2, the $m = 0$ growth-rate and wavenumber are respectively the least and most affected by non-parallel effects.

The 3D modes ($m \neq 0$) vanish within the jet core and so do not directly feel the effects of the jet diameter, aside from its effect on the curvature of the shear layer, with which they scale. These modes are increasingly affected by non-parallel effects: it happens that the $m = 1$ mode is the first to be independent of nozzle-diameter and as such does better than the $m = 2$ mode. Conversely, the 2D mode (zero spanwise wavenumber) in a planar mixing-layer or a flat-plate boundary layer would be the least affected by non-parallel effects as it has no special additional length-scale. This can be seen, *e.g.*, in the results of Bertolotti *et al.* (1992) who studied the Blasius boundary layer.

The PSE predictions for this case can be described as excellent. Note however the departure of amplitude predictions from the microphone data starting at $x/D \approx 4$ (depending on frequency), where disturbances have saturated. This is also due to acoustic contamination, briefly touched on above in relation to the phase-angle predictions in figure 3.8. This is the topic of the next section.

[3] This can also be seen on physical grounds: if $m \neq 0$ modes had a presence at the axis the solution $\hat{p}(r)\exp(im\theta)$ would be discontinuous as $r \to 0$.

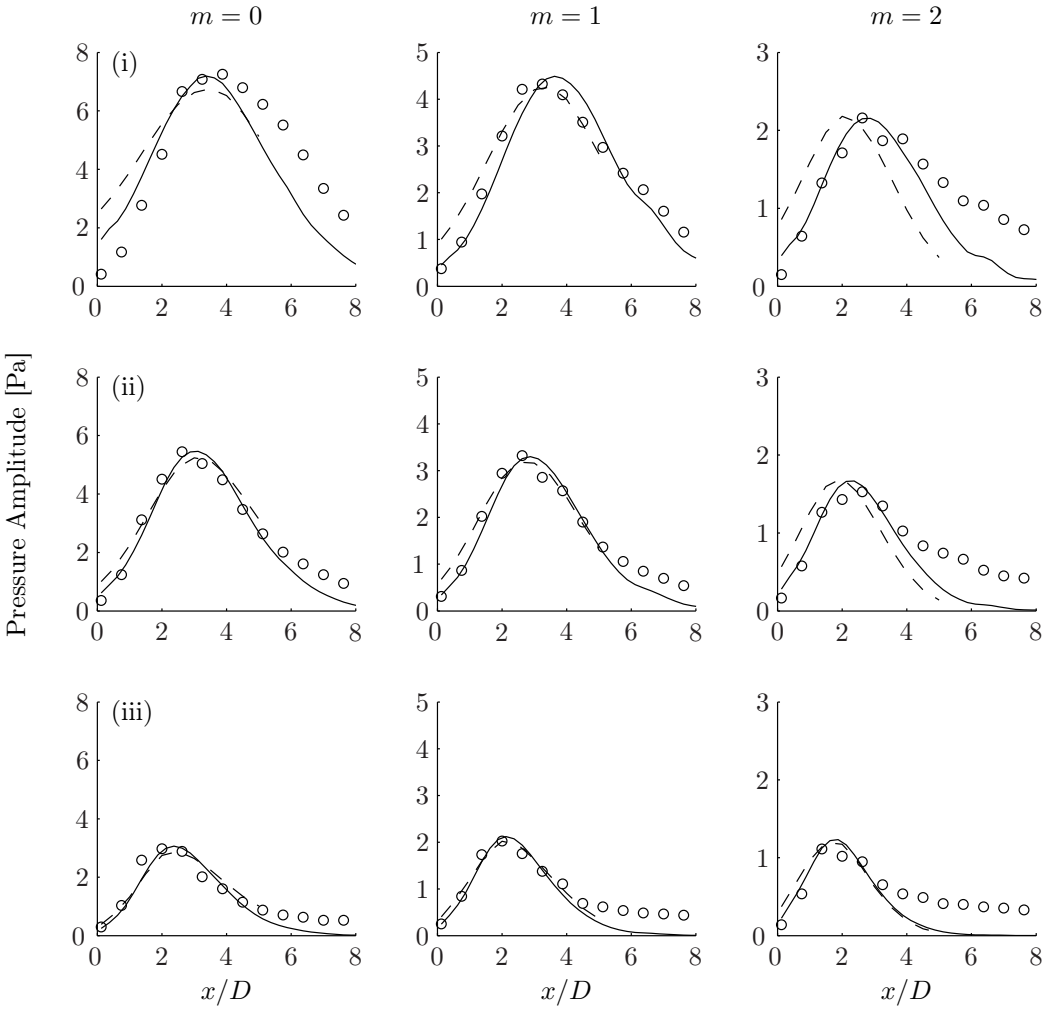

Figure 3.9: Pressure amplitude along the microphone array for the cold $M_\infty = 0.5$ jet. Predictions of (– – –) LST and (——) PSE compared with (∘) measurements, at frequencies (i) $St = 0.25$; (ii) $St = 0.35$; (iii) $St = 0.5$. Note m-dependence of ordinate.

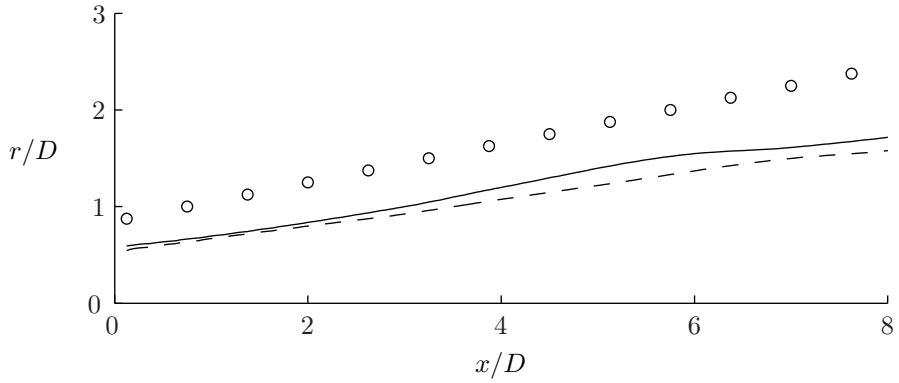

Figure 3.10: Contours of $\overline{u}_x/U_{jet} = 0.01$ for the cold (——) $M_\infty = 0.5$ and (- - -) 0.9 jets, along with (○) microphone positions.

3.4 The Nature and Treatment of The Pressure Measurements

We wish to evaluate the degree to which the hydrodynamic pressure field is consistent with instabilities evolving in the turbulent flow. To this end we need a good model for the evolution of instabilities and a way to decompose the measurements by their character: hydrodynamic or acoustic. Neither task is trivial and the latter is discussed below.

3.4.1 Composition and Complexity of the Measured Data

The microphone array was designed such as to place the microphones in the linear hydrodynamic regime (see figure 3.1) where pressure fluctuations are largely hydrodynamic. However, the extent and location of this regime varies with the flow condition, while the cone-angle of the array is fixed. This is illustrated in figure 3.10, where the contours of $\overline{u}_x/U_{jet} = 0.01$ for two different jets can be seen to align differently with the array. Microphone placement is particularly difficult for the higher speed jets as fluctuations in the near field scale with M_∞^2, while far field fluctuations scale as M_∞^4. This narrows the radial extent of the hydrodynamic regime and means more microphones will be situated in the acoustic regime. Since measurements are difficult and the resulting data non-perfect, a post-processing technique is needed.

Acoustic disturbances in the region where $\overline{u}_x \ll U_{jet}$ have sonic phase-speeds and propagate isotropically from their source. Hydrodynamic disturbances on the other hand have subsonic phase-

speeds (in subsonic and mildly supersonic flows) and the amplitude of their acoustic radiation is biased towards the flow direction. It thus seems natural to decompose the pressure measurements on the basis of phase-speed and/or directivity. Tinney & Jordan (2008) performed an experiment where the near field pressure of three co-axial subsonic jets was measured with a microphone array similar to the one in the current experiments, but with a significantly higher spatial resolution (48 microphones on a line array along with a movable ring carrying 15 microphones) and extent. Tinney & Jordan Fourier transform their data in time and azimuthal angle, and also in the streamwise coordinate, obtaining a wavenumber spectra α_r. Using this estimate of α_r, they propose to decompose measurements P into two components on the basis of phase-speed $c_p = \omega/\alpha_r$,

$$P = P\{c_p < a_\infty\} + P\{c_p \geq a_\infty\}, \tag{3.9}$$

Such a decomposition is shown in figure 3.11, for the hot $M_\infty = 0.9$ jet of this study. This figure shows contours of measured and decomposed pressure for the 13 microphones, as a function of time. The subsonic and supersonic components respectively have the expected slopes $dx/dt = 0.6\,U_{jet}$ (the convective velocity), and a_∞.

While this decomposition is capable of producing qualitatively accurate results, it is less fit in quantitative terms (*i.e.*, for comparing LST or PSE predictions to the hydrodynamic component $P\{c_p < a_\infty\}$). This is due to the limited streamwise resolution and, more importantly, the limited streamwise extent of the microphone array (truncation of the source region spawns high wavenumbers, essentially due to Gibbs phenomena).

An alternative approach is to examine two-point correlations in the measurements. The microphone data consists of a very large number of instantaneous zero-mean pressure measurements $P(x, r, \theta, t)$, each of which can be considered to be a convolution of the fluctuation field within the jet (George *et al.*, 1984). In particular the measurements can be triply-decomposed (Hussain & Reynolds, 1970) as

$$P = \overline{P} + P' + P'' \tag{3.10}$$

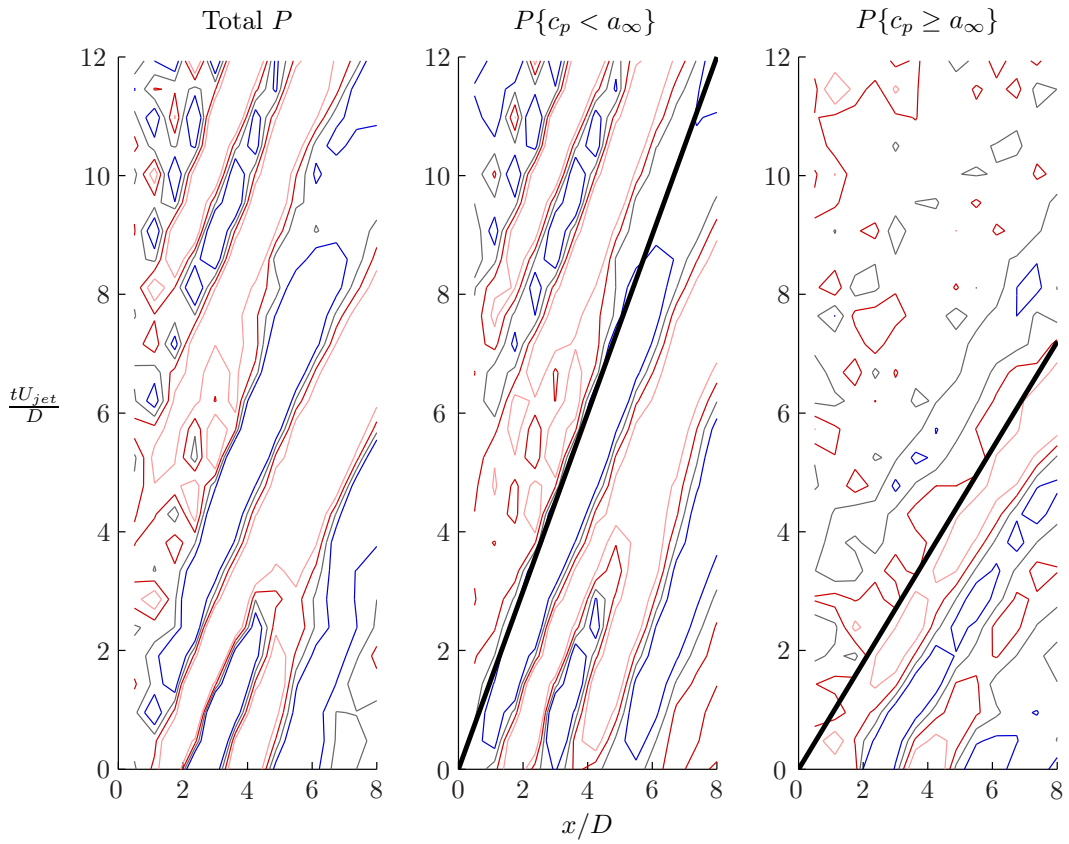

Figure 3.11: Instantaneous snapshots of $m = 0$ perturbation pressure and its Fourier-decomposition by phase-speed c_p. From left: total, subsonic, and supersonic pressure. The heavy lines in the subsonic and supersonic plots respectively have reciprocal slopes $dx/dt = 0.6U_{jet}$ (the convective velocity), and $dx/dt = a_\infty$ (ambient speed of sound). This data is taken from measurements of the hot $M_\infty = 0.9$ jet.

where $\overline{P} = 0$ is the time-average; P' is the phase-average[4], and P'' is the remainder. P' and P'' then respectively represent the coherent and incoherent components of the signal.

The triple-decomposition in equation (3.10) is a more general version of the (double) decomposition in equation (2.22), repeated here:

$$\mathbf{q} = \overline{\mathbf{q}} + \mathbf{q}'. \tag{3.11}$$

This we used to linearize the governing equations and subsequently assumed coherence upon the fluctuations by modeling them as waves. The question now becomes, how can we filter P'' from the measurements P, so that we may compare P' to the prediction p'?

The excitation of convected instabilities in unforced flows is a random process. The resultant instabilities thus have random amplitude and phase. Via forcing, these instabilities can be organized or phase-locked such that they appear in a relatively orderly manner at any given location and time. The phase-average can then easily be computed, with the forcing mechanism providing the phase (or lag) about which to average. In unforced flow the phase-average will be zero however, as instantaneously spatially-coherent structures will not appear in a time-coherent manner at a fixed location (they have random phase). In terms of the triple decomposition this means that the entire fluctuating energy is lumped into the remainder P''. The microphone data in figure 3.9 is essentially the Fourier transform of P''.

Over a large number of realizations however, fluctuations in unforced flows will occur in a "typical" manner, *i.e.*, an average spatial distribution of energy may converge. This is certainly the case in statistically stationary flows, by definition. The challenge is to separate this energy into those associated with P' and P''. The POD, described in section 2.4, provides an optimal mechanism by which a set of measurements may be separated into uncorrelated components and, as such, suits the problem at hand.

[4]The phase-average is a time-average where the wave is sampled not continuously but at fixed intervals τ, corresponding to the period of the wave of interest.

3.4.2 Filtering via the POD

Our application of the POD to the microphone data differs slightly from that described in section 2.4 in that we perform the POD in frequency-space rather than in time. Thus, instead of doing a POD of the set of instantaneous snapshots $P(x, r, \theta, t)$, we divide these series into ensembles, frequency-transforming each[5] and then perform the POD on this set.

We briefly outline the POD procedure here; refer back to section 2.4 for a more complete treatment. For clarity of presentation we omit the subscript pair $m\omega$ from all variables in what follows. The cross-spectral density tensor is defined as

$$R_{ij}^k = \widetilde{P}_k^{i*} \cdot \widetilde{P}_k^j, \tag{3.12}$$

where i and j range from 1 through N_{ring}, and $\widetilde{P}_k^j$ is the transformed measurement in ensemble k, evaluated at $x = x_j$. We then form the ensemble-averaged cross-spectral density tensor,

$$R = \langle R^k \rangle = \frac{1}{N_{ens}} \sum_{k=1}^{N_{ens}} R^k \tag{3.13}$$

and solve the eigenvalue problem

$$R\,\boldsymbol{x} = \lambda \boldsymbol{x}. \tag{3.14}$$

By construction, R is Hermitian and positive definite so that $\lambda_j \geq 0$ and eigenvectors corresponding to different eigenvalues are orthonormal. The λ_j are ordered such that $\lambda_{j+1} \leq \lambda_j$. A faster rate of decay of the λ_j series indicates a higher correlation or coherence in the data. This is because the POD-modes $\boldsymbol{x}_i$ are uncorrelated, which follows from their orthonormality: $\langle \boldsymbol{x}_i, \boldsymbol{x}_j \rangle = \delta_{ij}$, where δ_{ij} is the Kronecker-delta.

The cross-spectral density tensor R can be reconstructed from the POD-modes,

$$R_{ij} = \sum_{n=1}^{N_{ring}} \lambda_n \boldsymbol{x}_i(n)^* \, \boldsymbol{x}_j(n). \tag{3.15}$$

[5]The measurements $\widetilde{P}_{m\omega}$ reported in figures 3.8 and 3.9 are based on the ensemble-average of this set.

This decomposition allows the POD-filtering of the measured data $\widetilde{P}$, where only the highest-energy mode is retained,

$$\mathrm{POD}(\widetilde{P}) = \sqrt{\lambda_1}\,\boldsymbol{x}_1. \tag{3.16}$$

The application of the POD to the present data is discussed in the next section.

3.5 Comparisons with POD-Filtered Data

In the following sections we respectively denote measured and computed quantities with upper and lowercase letters. For readability we suspend the subscript $m\omega$.

3.5.1 The Cold $M_\infty = 0.5$ Jet

Figures 3.12 and 3.13 respectively show the evolution of pressure amplitude and phase along the microphone array for the cold $M_\infty = 0.5$ jet. Included in these figures are the ensemble-averaged data $\langle\widetilde{P}\rangle$, the POD-filtered data $\mathrm{POD}(\widetilde{P})$, and the scaled PSE-prediction $\widetilde{p}$. As was noted in section 3.3.2, the PSE-predictions match the ensemble-average well up to saturation of the peak the two diverge, presumably due to acoustic contamination of the measurements, and increasingly so with larger m or ω. The acoustic character of the contamination is most readily seen in the phase-angle measurements in figure 3.13. The phase-speed is inversely proportional to the slope of these curves. In some cases, such as at frequency $St = 0.35$, the phase-angle measurement is nearly horizontal, indicating infinite phase-speed. It is of course not the case that these fluctuations propagate with such speed but rather that they propagate near-normally to the array, hitting several microphones simultaneously. A wave front traveling in parallel to the array would be measured as traveling at the ambient speed of sound.

We now turn our attention to the POD-filtered measurements. The effectiveness of the filtering is striking in some cases, such as at $St = 0.35$. The POD-filtered phase-angle follows the PSE-predictions near-exactly, and similarly for the amplitude. Also impressive is the broad range of frequencies and azimuthal modes over which the predictions largely capture the POD-filtered evo-

lution, even at frequencies as high as $St = 0.65$. This frequency is considerably removed from that at the peak.

Particularly interesting is the broad spatial range of match, even beyond the closure of the potential core (which occurs at $x/D \approx 6.4$ as can be seen in figure 2.5). This is partly counter-intuitive, as one would expect nonlinearities to become significant as disturbances grow to saturation. Recall that the mean flow $\overline{\mathbf{q}}(\mathbf{x})$ used in the solution of the PSE equations is obtained from PIV measurements of the turbulent flows in our study. Nonlinear phenomena such as vortex pairing are then implicitly accounted for through their imprint on the mean flow evolution. Their inclusion is only partial, though, as the interactions of large-scale fluctuations with each other and with fine-scale turbulence are not considered by the linear PSE. The wide spatial range of favourable match is thus interesting, as it indicates that nonlinear interactions are mostly important in terms of their impact on the mean flow evolution, at least at this flow condition and some of the considered frequencies.

Using mean flow from a DNS of a cold $Re = 2000$, $M_\infty = 2$ jet, Mohseni *et al.* (2002) solved the linearized Navier-Stokes (LNS) equations and compared the linear solution to the fluctuating component of the DNS. This is similar to the current approach, aside from the additional assumptions needed in reducing the LNS to the linear PSE. Mohseni *et al.* found that LNS fluctuations generally match the DNS in terms of directivity and peak Strouhal numbers. The LNS underpredicts growth-rates and sound-pressure levels however, with the exception of those near the peak frequency of the $m = 1$ mode. They thus conclude that nonlinear interactions must be accounted for in order to obtain accurate growth-rates.

The current results run somewhat counter to this and we hypothesize that the difference lies with the effects of compressibility, one of which is stabilization: growth-rates decay with increasing Mach number. It is likely that linear instabilities dominate low-amplitude dynamics to a lesser extent under such circumstances, the evolution proceeding via more subtle mechanisms such as modal interactions. Nonlinearities are thus increasingly important at higher Mach-numbers.

Something curious happens far downstream for $m = 2$ and $St = 0.65$, where the POD-filtered amplitude is seen to rise slightly after having decayed, and the corresponding phase-angle levels off,

much as the ensemble-average. This phenomena is more pronounced for the heated and higher-speed jets and is discussed in the next sections.

3.5.2 The Cold $M_\infty = 0.9$ and Hot $M_\infty = 0.5$ Jets

Figure 3.14 shows evolution of pressure amplitude and phase at $St = 0.35$ along the microphone array for the cold $M_\infty = 0.9$ jet. As for the cold $M_\infty = 0.5$ jet, the benefits of POD-filtering are considerable (compare figure 3.14 with part (ii) of figures 3.12 and 3.13). The relative improvement is greater for the higher-speed jet, though, as it is more contaminated. This is because hydrodynamic pressure scales as M_∞^2, while acoustic pressure scales as M_∞^4, increasing the acoustic proportion of the signal[6].

It is well known that heating has a destabilizing effect on free shear layers. This is illustrated in figure 3.15, where we compare growth-rates of the hot and cold $M_\infty = 0.5$ jets. All azimuthal modes are amplified with heating but none so much as the axisymmetric mode, whose maximum growth-rate is nearly doubled. This destabilization and m-dependence thereof can also be seen in the measurements of the two $M_\infty = 0.5$ jets in figures 3.12 and 3.15.

It has been shown (Monkewitz & Sohn, 1988; Lesshafft & Huerre, 2007) that sufficiently heated round jets are susceptible to absolute instability, where a disturbance grows exponentially in time while remaining fixed where it was generated (*i.e.*, it has zero phase-speed). We note however that absolute instability is precluded for the hot jets in this work, both due to their relatively low temperature ratio of $T_{jet}/T_\infty = 1.76$, and their high-speed.

Figure 3.16 shows evolution of pressure amplitude and phase at $St = 0.35$ along the microphone array for the hot $M_\infty = 0.5$ jet. The match between the PSE-prediction and the POD-filtered measurements is again remarkable, particularly given the higher level of acoustic contamination as compared with the cold $M_\infty = 0.5$ jet (compare figure 3.16 with part (ii) of figures 3.12 and 3.13). Note however the apparently mixed hydrodynamic-acoustic nature of the $m = 2$ POD-filtered pressure at this flow condition. The phase-angle prediction is very good past saturation, after which the

[6]The M_∞^2 scaling can be observed in the current measurements: the maximum amplitude of the $M_\infty = 0.5$ signal at $m = 0$, $St = 0.35$ is $\sim 6Pa \rightarrow (0.9/0.5)^2 \cdot 6 \approx 19.5Pa$, which compares well with the $\sim 20Pa$ recorded for the $M_\infty = 0.9$ jet in figure 3.14.

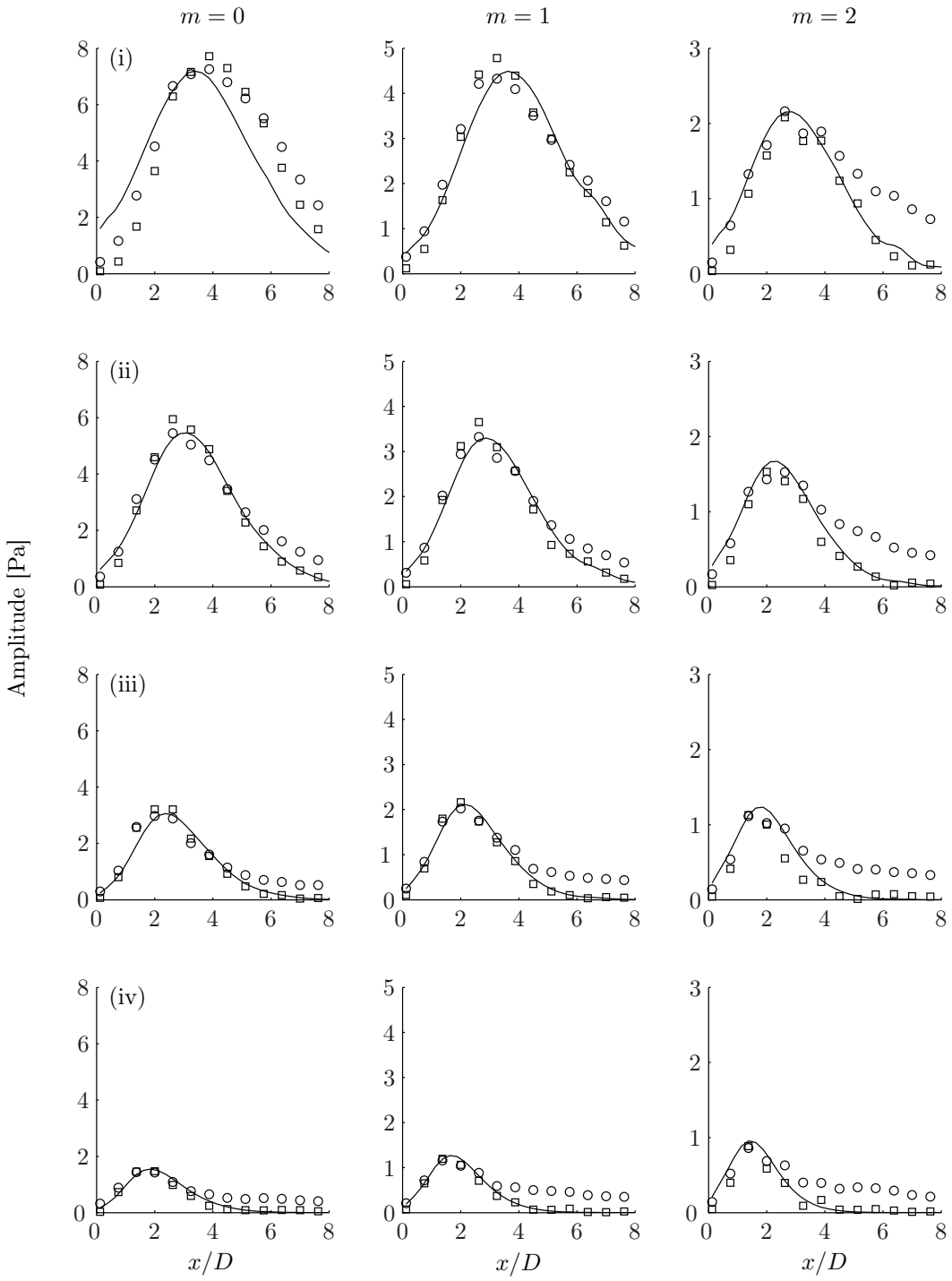

Figure 3.12: Pressure amplitude along the microphone array for the cold $M_\infty = 0.5$ jet: (○) ensemble-average; (□) first POD-mode; (——) PSE-predictions, at frequencies (i) $St = 0.25$; (ii) $St = 0.35$; (iii) $St = 0.5$; (iv) $St = 0.65$. Note m-dependence of ordinate.

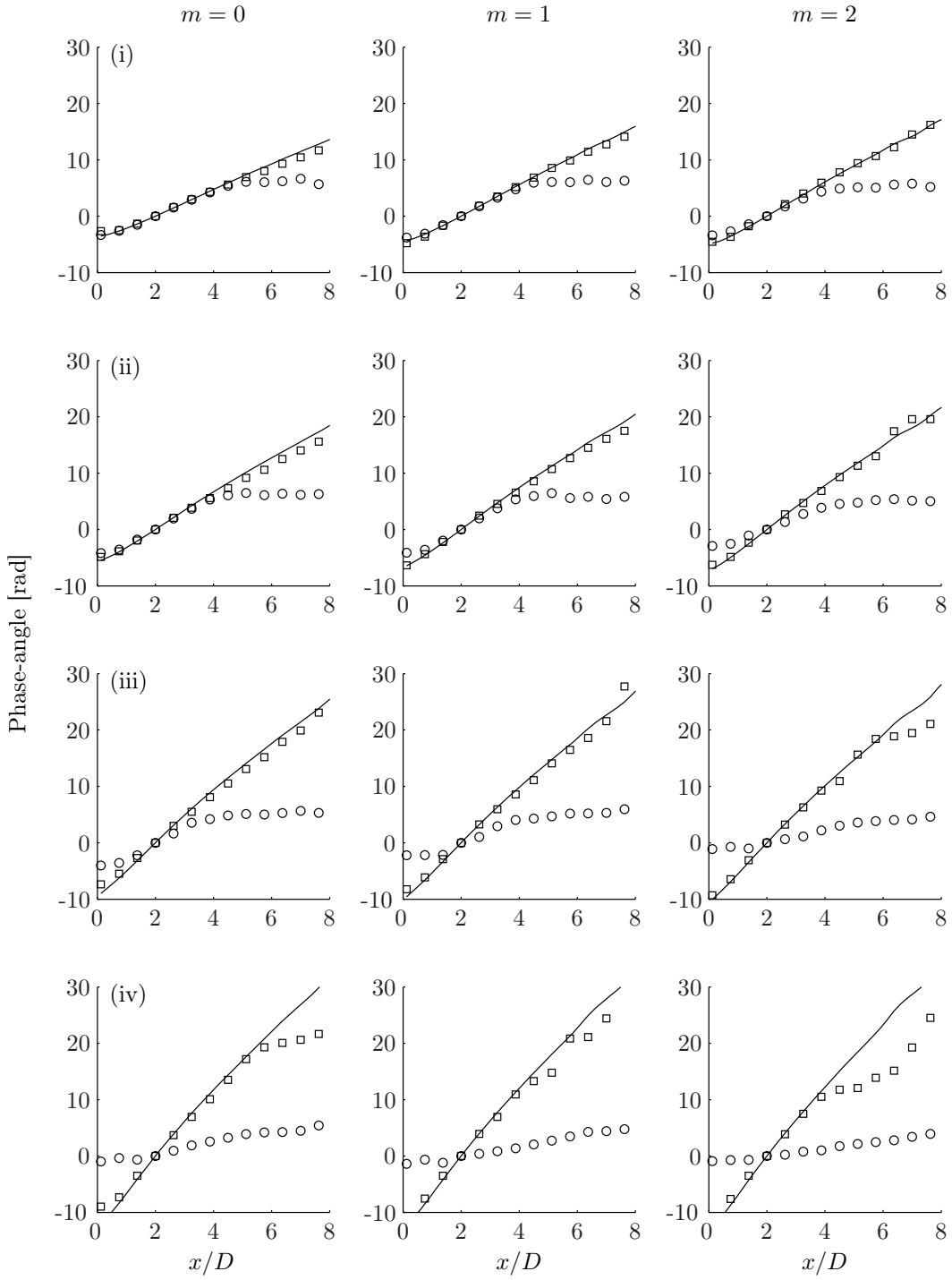

Figure 3.13: Phase-angle along the microphone array for the cold $M_\infty = 0.5$ jet: (○) ensemble-average; (□) first POD-mode; (——) PSE-predictions, at frequencies (i) $St = 0.25$; (ii) $St = 0.35$; (iii) $St = 0.5$; (iv) $St = 0.65$.

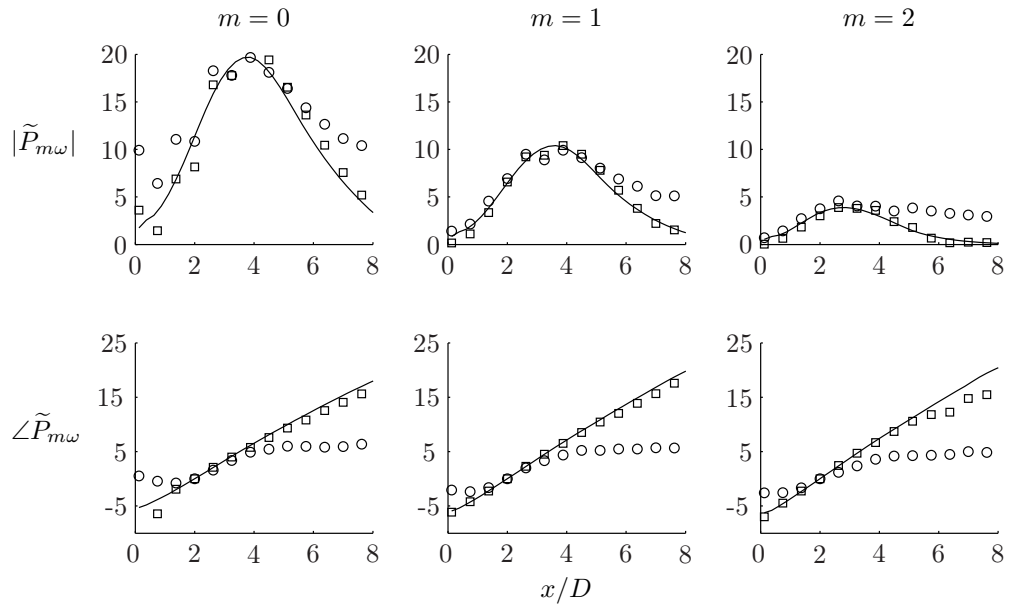

Figure 3.14: Pressure amplitude and phase-angle along the microphone array for the cold $M_\infty = 0.9$ jet: ○, measurements; □, first POD-mode; ——, PSE, at frequency $St = 0.35$.

POD-filtered phase levels off similarly to the ensemble-average. At the same streamwise location the POD-filtered amplitude grows slightly after having decayed earlier.

Comparing the increase in acoustic content between the cold $M_\infty = 0.5$ and 0.9 pair on one hand, and the cold and hot $M_\infty = 0.5$ pair on the other, it appears the heating induces even more acoustic content than the higher speed. The high-speed heated jet suffers maximally from this and is discussed in the next section.

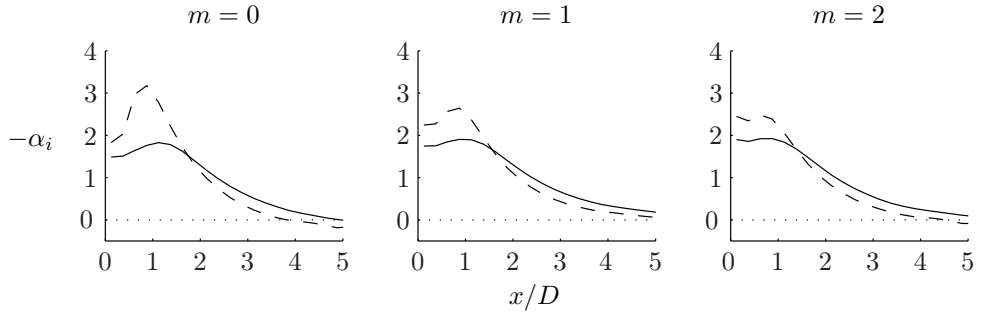

Figure 3.15: Growth-rates $-\alpha_i$ for the (——) cold and (- - -) hot $M_\infty = 0.5$ jets, at frequency $St = 0.35$.

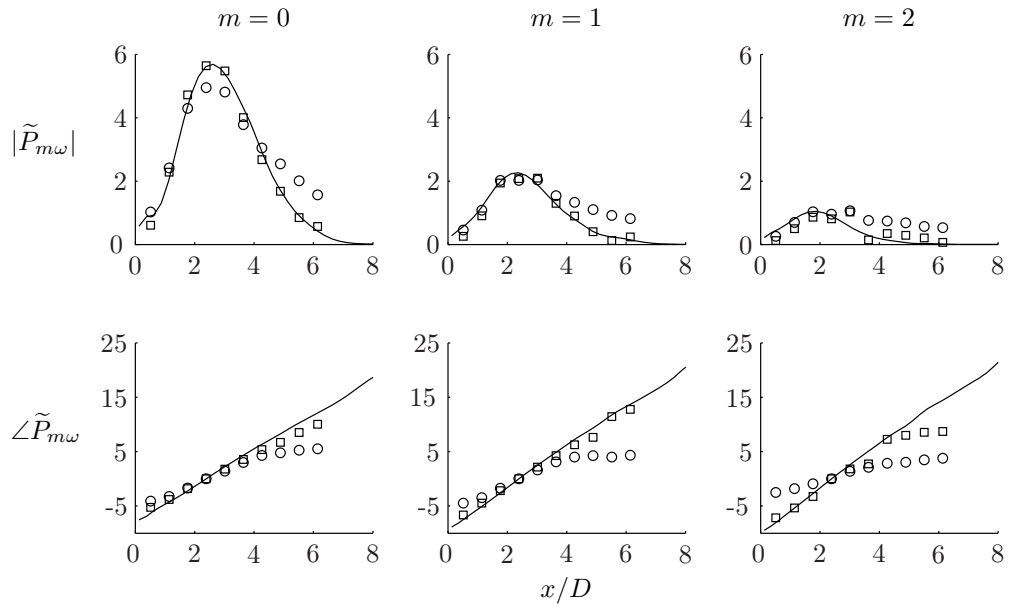

Figure 3.16: Pressure amplitude and phase-angle along the microphone array for the hot $M_\infty = 0.5$ jet: ○, measurements; □, first POD-mode; ——, PSE, at frequency $St = 0.35$.

3.5.3 The Hot $M_\infty = 0.9$ Jet

Here we look at the last remaining flow condition in table 2.1, the hot $M_\infty = 0.9$ jet. Figures 3.17 and 3.18 respectively show the evolution of pressure amplitude and phase along the microphone array. Nearly all of the frequencies and azimuthal modes for this jet suffer considerably from acoustic contamination of the signal. It is only the axisymmetric mode, and low frequencies of the $m = 1$ mode that are effectively filtered by the POD. The $m = 2$ POD-filtered mode appears mostly acoustic, even at the lowest frequency considered.

The POD separates a given set of measurements into uncorrelated components that can be ordered by their energy, represented by their respective eigenvalues λ_j (see section 3.4.2). In our application of the POD above we compared the PSE-predictions to the highest-energy POD-mode (which has energy λ_1), discarding all others. Thus when we say that high order modes are ineffectively filtered by the POD, we are saying that for these modes the acoustic component has comparable, or even greater energy (*e.g.*, for $m = 2$ at $St = 0.5$) than the hydrodynamic one. The energy separation is frequency dependent and comparable energies can be found at all flow conditions, even for the 'cleanest' flow in this study, the cold $M_\infty = 0.5$ jet (*e.g.*, $m = 2$ at $St = 0.65$

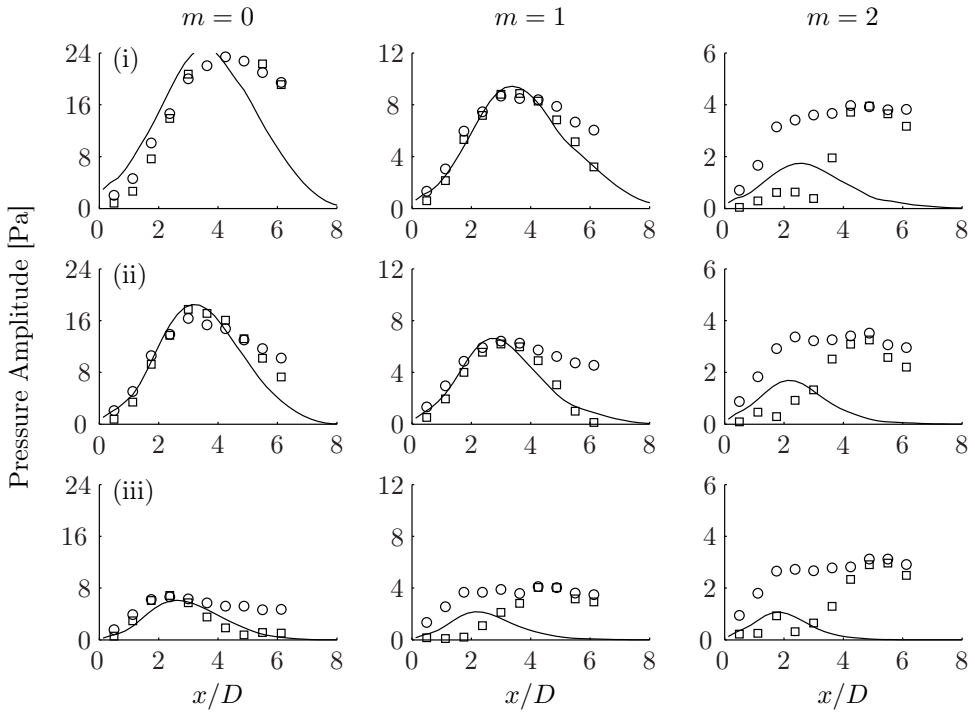

Figure 3.17: Pressure amplitude along the microphone array for the hot $M_\infty = 0.9$ jet: ○, measurements; □, first POD-mode; ——, PSE, at frequencies (i) $St = 0.25$; (ii) $St = 0.35$; (iii) $St = 0.5$.

in figure 3.12). In this regard there is nothing special about the hot high-speed jet, aside from the severity of contamination and the extended range of affected modes.

Figure 3.19 shows the POD energy-spectra of two extremal jets: cold $M_\infty = 0.5$ and hot $M_\infty = 0.9$. These spectra have been normalized by the total energy of each mode (m, ω),

$$||\widetilde{P}_{m\omega}||^2 = \sum_{k=1}^{N} \lambda_k. \tag{3.17}$$

The ratio $\lambda_j / \sum_{k=1}^{N} \lambda_k$ thus represents the fraction of energy contained in POD-mode j. The spectral-decay is consistent with the behavior already deduced in the comparisons above. At the lowest frequencies the two spectra behave similarly. With increasing frequency the two spectra diverge however, with the slower jet having faster spectral-decay in all cases. Fast spectral-decay indicates greater coherence in the data, while, in the other extreme, a randomly composed data-set has a nearly flat spectrum. The slower jet is thus in some sense simpler or more coherent than the

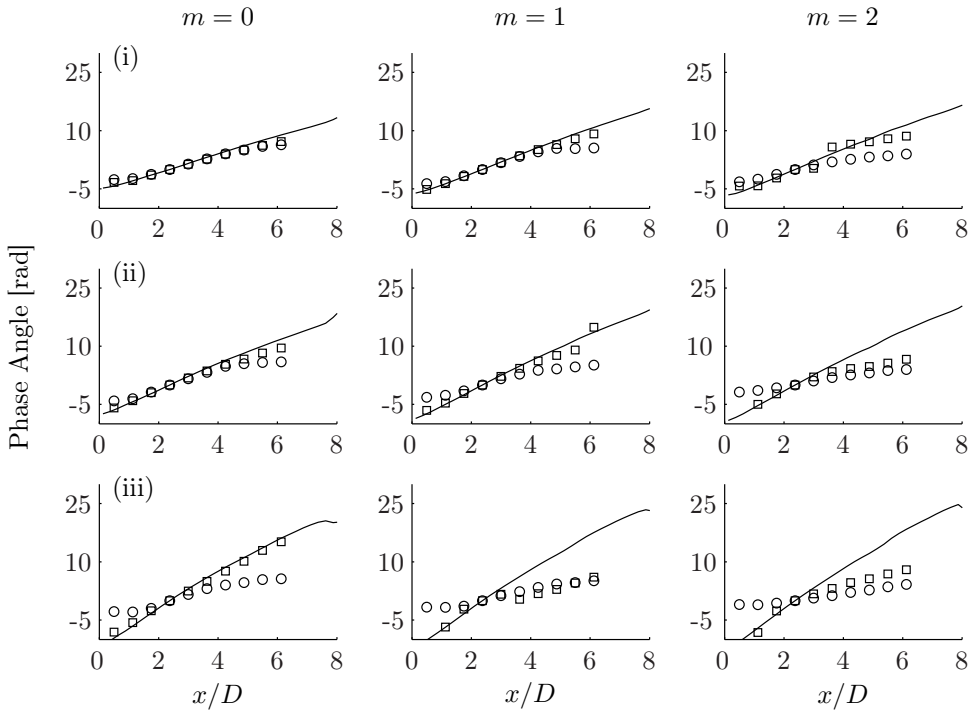

Figure 3.18: Pressure phase along the microphone array for the hot $M_\infty = 0.9$ jet: ∘, measurements; □, first POD-mode; ——, PSE, at frequencies (i) $St = 0.25$; (ii) $St = 0.35$; (iii) $St = 0.5$.

other.

Let us use the $m = 1$ mode of frequency $St = 0.5$ (plot (iii) in figure 3.19) as an example in what follows. The first POD-mode captures 75% of the slower jet's energy. After $j = 1$, the spectra is relatively flat; these trailing components represent low-energy noise. Now look back at the PSE-POD comparison in figure 3.12 (iii): the prediction is near-flawless. The first POD-mod of the higher-speed jet only contains 45% of the energy. To get up to 75% energy-content we need to the first three modes, after which the spectra levels out. The PSE-POD comparison in this case (figure 3.17 (iii)) was not favorable and in fact the first POD-mode looks nothing like the hydrodynamic component. Looking at the spectra for this case, one might thus conjecture that the hydrodynamic component is contained in the second or even third POD-mode. Figure 3.20 shows that this is indeed the case.

Figure 3.20 shows the pressure amplitude and phase-angle comparisons for the two jets under discussion, at $m = 1$ and $St = 0.5$. We omit the ensemble-average but rather show the first three POD-modes along with the PSE-prediction. The comparison between the PSE-prediction and the

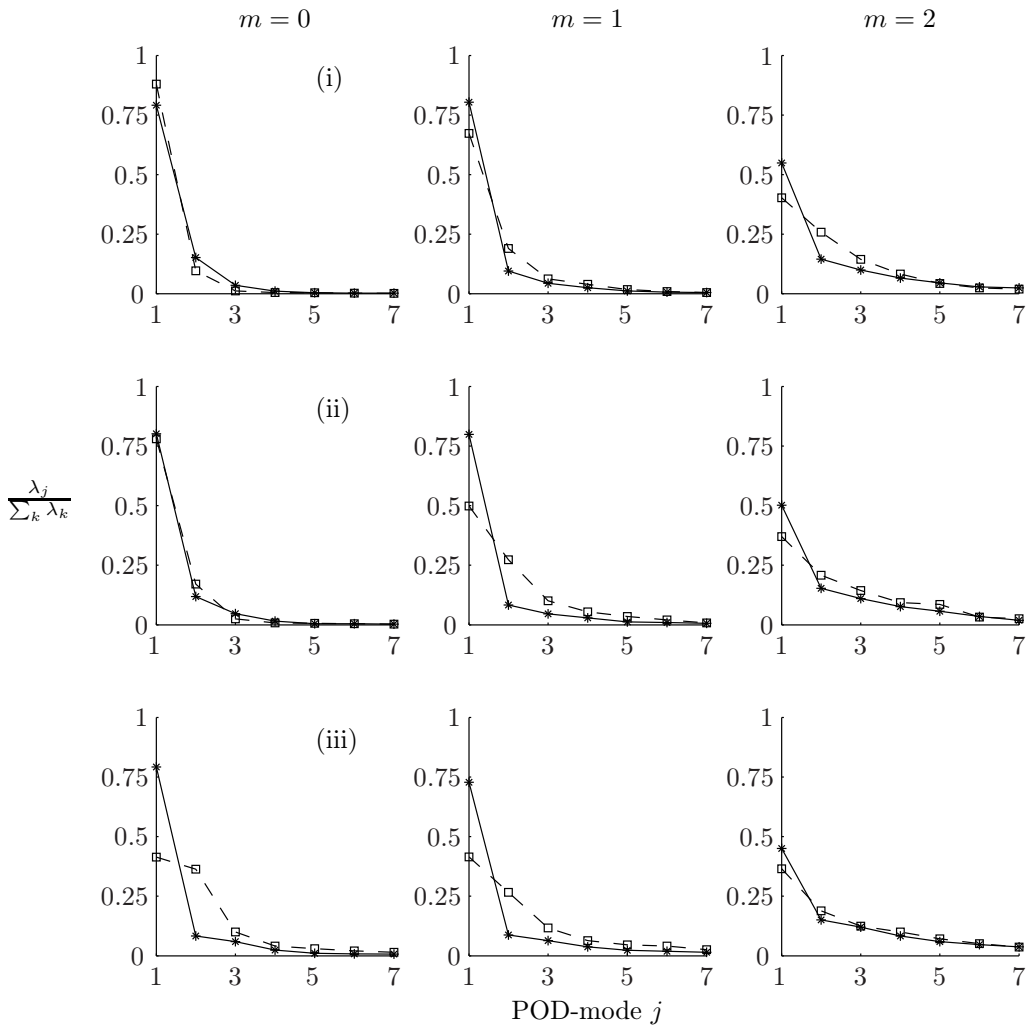

Figure 3.19: Normalized POD-spectra of the ($*$) cold $M_\infty = 0.5$ jet and ($\square$) hot $M_\infty = 0.9$ jet at frequencies (i) $St = 0.25$; (ii) $St = 0.35$; (iii) $St = 0.5$.

first POD-mode of the slower jet is excellent as we had indeed already seen in figure 3.12 (iii). The second and third POD-modes have some hydrodynamic qualities, such as growth and decay in a similar span as the first POD-mode, and a convective phase-speed (*i.e.*, slower than acoustic). But this is only the case in the growth-phase. After this point both modes are clearly acoustic, as judged by the phase-speed (low slope of the phase-angle curve).

Turning now to the higher-speed jet, we first note that while the first POD-mode is slightly hydrodynamic in the first two diameters, it is acoustic there after. This is interesting as this mode is the most energetic, having roughly 45% of total energy. As we had noted in (figure 3.17 (iii)), this mode does not compare well with the PSE-prediction. Remarkably, though, the second POD-mode does. In fact, the comparison with this mode is quite good, both in terms of amplitude and phase-angle. This mode has roughly 30% of the total energy but note however that it is indeed the most energetic past saturation. Thereafter, it takes on some acoustic qualities, such as higher phase-speed. The third POD-mode in this case seems acoustic throughout.

Apparent throughout the discussion above is the fact that POD-modes seem capable of being simultaneously hydrodynamic and acoustic. This can be deduced by the spatial properties of the eigenvectors $\boldsymbol{x}_j$ in equation (3.16). The most telling indicator is the slope of the phase-angle curve (phase-speed). This has spatial variance such that a single mode might be convective upstream and acoustic downstream. Recall that the POD breaks the data-set up into uncorrelated (orthogonal) pieces or modes, the POD-modes. Each POD-mode then represents a set of points which are consistently in phase (they are correlated). The above results then indicate a strong correlation between hydrodynamic waves and acoustic waves. But this is surprising as one would think that hydrodynamic-hydrodynamic and acoustic-acoustic correlations should dominate the high-energy modes, followed by trailing hydrodynamic-acoustic correlations. But this is not the case and indicates that the acoustic part of the instability wave has comparable energy with the non-radiating part for this flow condition.

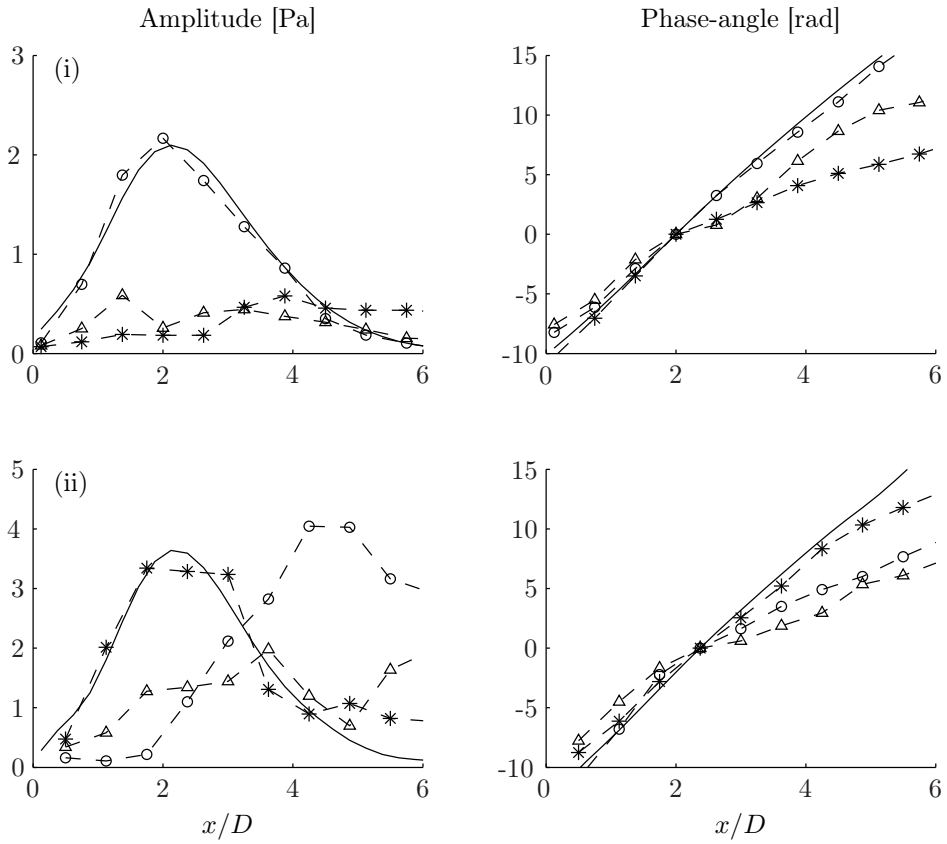

Figure 3.20: Pressure amplitude and phase-angle along the microphone array for the (i) cold $M_\infty = 0.5$ and (ii) hot $M_\infty = 0.9$ jets. Shown are the ($\circ$) first, ($*$) second, and ($\triangle$) third POD-modes, along with (——) PSE-predictions, at $m = 1$ and $St = 0.35$. PSE amplitudes of cold and hot jets chosen using first and second POD-modes, respectively.

3.6 Summary

In this chapter we investigated the linear dynamics of large-scale structures in the near-field of turbulent subsonic round jets. Using mean flows based on ensemble-averaged PIV measurements (Bridges & Wernet, 2003) we computed near-field fluctuations via the linear stability equations (LST) and the parabolized stability equations (PSE). We analyzed two pairs of hot and cold $M_\infty = 0.5$ and 0.9 jets, listed in table 2.1. We compared our predictions to near-field microphone measurements (Suzuki & Colonius, 2006) performed using the caged-array at NASA Glenn's SHJAR facility.

We found that LST underestimates growth-rates and overestimates wavenumbers. It thus predicts more stable and longer waves than is the case in actuality. This causes premature saturation as the neutral-point is shifted upstream. We showed that this is due to LST's negligence of history effects, rather than the omission of additional non-parallel shear-terms such as $\partial_x \overline{u}_x$. These have only a weak effect on the evolution. The locally-parallel flow assumption affects all azimuthal modes, particularly at sub-peak frequencies. The $m = 1$ mode performs the best and is less affected than $m = 0$ and 2. This non-monotonic m-dependence of the effects of the locally-parallel flow is curious. We hypothesized that the $m = 0$ mode is impacted due to its dependence on the nozzle-diameter D, resulting in longer wavelengths. The $m \neq 0$ modes are increasingly affected by non-parallel effects: it happens that the $m = 1$ mode is the first to be independent of nozzle-diameter and as such does better than the $m = 2$ mode. Conversely, the 2D mode (zero spanwise wavenumber) in a planar mixing-layer or a flat-plate boundary layer would be the least affected by non-parallel effects as it has no special additional length-scale. This can be seen, *e.g.*, in the results of Bertolotti *et al.* (1992) who studied the Blasius boundary layer.

Next we compared pressure predictions of LST to those of PSE for the cold $M_\infty = 0.5$ jet. The LST does well at and above the peak-frequency, but great improvements by the PSE are observed at lower frequencies, particularly for $m = 0$ and 2.

The microphone data is comprised of both hydrodynamic and acoustic pressure fluctuations. The POD allows the separation of the data into uncorrelated components. We performed this analysis

and compared PSE predictions to the most energetic POD-mode. The comparisons so obtained were greatly improved, particularly for the higher-speed and heated jets which had appeared the most contaminated. For the cold jets the PSE predictions match very well, even beyond the end of the potential core. Particularly interesting is the broad spatial range of match. This is partly counter-intuitive, as one would expect nonlinearities to become significant as disturbances grow to saturation. Recall that the we use ensemble-average PIV measurements in solving the PSE. Nonlinearities are thus implicitly included via their imprint on the mean flow evolution. Their inclusion is only partial, though, as the interactions of large-scale fluctuations with each other and with fine-scale turbulence are not considered by the linear PSE. Our results thus indicates that nonlinear interactions are mostly important in terms of their impact on the mean flow evolution, at least at this flow condition and some of the considered frequencies. We noted that this seems to run counter to the results of Mohseni *et al.* (2002) and hypothesized that the difference lies with the increased importance of modal interactions at higher speeds, due to stabilization of large-scale structures.

We observed POD-modes of mixed hydrodynamic and acoustic nature, indicating a significant correlation between hydrodynamic waves and acoustic waves. We hypothesized that the acoustic portion of these POD modes represents the Mach wave radiation of the large-scale structure. Otherwise, these components would not be consistently in phase (correlated) and could not "live" within the same POD-mode.

While there remain some discrepancies between data and PSE, particularly for the axisymmetric mode at the lowest frequencies, the PSE seems to provide an accurate representation of the streamwise evolution of pressure fluctuations well past the close of the potential core. It is possible, for example, that the inclusion of nonlinear effects will result in better agreement, and this is presently being pursued. It remains to compare the directly measured far-field sound by what would be implied by the near field fluctuations from PSE. PSE does not directly provide the acoustic far field (especially at subsonic speeds), but acoustic analogy and Kirchhoff-surface type approaches have been developed for this purpose (Balakumar, 1998; Reba *et al.*, 2010). In particular, Reba *et al.* (2010) have successfully developed a Kirchhoff-surface approach and applied it to predicting sound

from the same near-field microphone array data used in the present study.

Chapter 4

The Effects of Nozzle Serrations on the Linear Stability of Turbulent Jets

4.1 Introduction

Great strides have been made in jet noise reduction both via theory and experiment. Most significant of these was the advent of the turbofan engine in which a large proportion of the air flow bypasses the central turbojet to flow inside an outer duct at a much lower speed. This reduces the average exhaust speed required to produce a given thrust, significantly increasing fuel efficiency and retarding noise emission. More subtle approaches to noise reduction have also been pursued, most of which involve the manipulation of the thin boundary layer on the inside of the nozzle. This is commonly accomplished via the introduction of serrations into the nozzle lip.

The effects of nozzle serrations on the evolution and mean flow characteristics of mixing layers have been studied by various researchers. The serrations, shown in figure 4.1, generate streamwise vorticity, promoting the mixing of the jet fluid with the ambient and shortening the potential core (Bradbury & Khadem, 1975; Zaman *et al.*, 1993; Reeder & Samimy, 1996; Bohl & Foss, 1999). They also reduce noise at low frequencies and aft angles, but increase noise at high frequencies (Bridges & Brown, 2004; Callender *et al.*, 2005; Alkislar *et al.*, 2007). The noise penalty at higher frequencies is due to heightened near-nozzle turbulence levels that in turn correlate positively with the magnitude of streamwise vorticity (Foss & Zaman, 1999), as does the noise reduction at low frequencies.

Sound radiated at low frequencies and aft-angles is associated with large-scale coherent structures convecting within the jet (Moore, 1977; Troutt & McLaughlin, 1982; Laufer & Yen, 1983; Crighton & Huerre, 1990; Tam *et al.*, 1996; Goldstein, 2003). As the jet exits the nozzle, the boundary layer relaxes to a free shear layer, susceptible to Kelvin-Helmholtz instability. Such instabilities get exited by the chaotic fluctuations present at the exit and grow into large-scale coherent structures (Mattingly & Chang, 1974; Crighton & Gaster, 1976; Mankbadi & Liu, 1981). As they grow they roll up via subharmonic pairing, forming axisymmetric and helical rings (Crow & Champagne, 1971) that eventually loose their coherence via vortex instabilities (Widnall & Tsai, 1977) and nonlinear interactions. As discussed in section 1.3.3, large-scale coherent structures radiate sound during their growth phase (Mach-wave radiation) as well as during their decay and ultimate demise. It has been suggested that the breakdown of such structures may be the dominant source of sound at subsonic conditions (Hussain, 1983, 1986). It appears that the streamwise vorticity induced by the serrations interrupts these processes, perhaps by retarding the initial growth of large-scale structures.

The early development of large-scale coherent structures is largely linear. Several studies have shown the velocity and pressure fluctuations of forced jets to be well approximated by the eigenfunctions of the Rayleigh (inviscid Orr-Sommerfeld) equation (Mattingly & Chang, 1974; Zaman *et al.*, 1980; Petersen & Samet, 1988), where the spatial stability problem is solved. As discussed in section 3.1, disturbances in natural jets are correlated over shorter spatial and temporal length scales, making their unbiased detection challenging. This is further confounded at higher Reynolds numbers where the relative energy associated with large-scale coherent structures is diminished due to increased production of fine-scale turbulence. However, Suzuki & Colonius (2006) found good agreement near the most amplified frequency between pressure predictions of linear stability analysis and measurements from a near-field microphone array, indicating that energy transfer between coherent and incoherent motions has only minor effects on the former, even for natural jets. Using the parabolized stability equations to model instability waves and the proper orthogonal decomposition to filter the microphone data, Gudmundsson & Colonius (2010*a*) showed that the agreement obtained by Suzuki & Colonius can be extended even beyond the closure of the potential core. This is

discussed in detail in chapter 3.

It therefore seems reasonable to assume linear stability analysis can offer some understanding of the effects of serrations on coherent motions in the flow. Standard linear stability analysis considers, at each streamwise position, a one dimensional, two-point boundary value problem amenable to direct matrix solution or shooting algorithms. The Rayleigh equation (2.50), along with appropriate boundary conditions, is an example of such a boundary value problem. The serrated jet on the other hand is inhomogeneous in both coordinate directions normal to the stream. This is a technical difficulty, though, and not a theoretical one; in section 4.2 we show that the stability problem for the serrated jet is governed by a system of coupled Rayleigh-like ordinary differential equations.

Linear stability analysis of quasi-parallel flows assumes a negligible spread rate over typical fluctuation length-scales, so that cross sections of the jet are analyzed as if each one was a sample from a parallel mean flow. Quasi-parallel analysis can be considered to form the first term in an asymptotic expansion using the flow spread rate as the expansion parameter. The analysis can subsequently be refined by expanding the solution to higher order (*e.g.*, Tam & Morris, 1980). Figure 4.2 shows the momentum thickness θ/D, defined as

$$\frac{\theta}{D} = \int_0^\infty \frac{\overline{u}_x}{U_{jet}} \left(1 - \frac{\overline{u}_x}{U_{jet}}\right) r dr, \tag{4.1}$$

for the round and serrated jets included in this study ($M_\infty = 0.9$, $T_{jet}/T_\infty = 0.85$, and $Re = 1.6{\cdot}10^6$). The serrated jet has a higher spread rate initially, approaching that of the axisymmetric jet further downstream. The locally-parallel mean flow assumption is thus, a *priori*, somewhat more suspect for the serrated jet than the round jet. However, in light of the demonstrated success of such analysis for round jets, its application to the the serrated jet is certainly reasonable.

In section 4.2 we derive the linear stability problem for the serrated jet and discuss some of its properties. In section 4.3 we solve the stability problem for a pair of subsonic round and serrated jets, and investigate the resultant modes. In section 4.4 we compare our LST predictions to both unprocessed and POD-filtered microphone measurements. Finally, we summarize our findings in

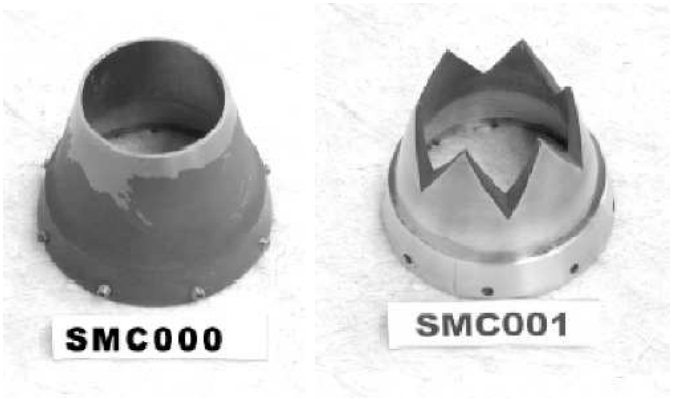

Figure 4.1: The (left) round and (right) serrated nozzles used in this study. The serrated nozzle was fabricated from a standard 2-inch diameter round nozzle, the same type as shown here. Serial numbers are as defined by Bridges & Wernet (2003).

section 4.5.

4.2 The Linear Stability Problem for The Serrated Jet

The serrated jet is inhomogeneous in both coordinate directions normal to the stream, shown in figure 4.3. This means that the associated stability problem is of higher dimension than that of the axisymmetric jet. Kawahara *et al.* (2003) solved the (temporal) linear stability problem for a corrugated vortex sheet near a wall, which can be considered to be the planar version of a serrated top-hat (vortex-sheet) jet profile. Here we formulate and solve the more general problem that includes finite shear-layer thickness.

The initial development in the below is similar to that in section 2.3.1 and is partially reproduced here for continuity. As for the round jet, we decompose the nonlinear flow $\mathbf{q} = (u_x, u_r, u_\theta, \rho, T, p)$[1] as

$$\mathbf{q} = \overline{\mathbf{q}} + \mathbf{q}'. \tag{4.2}$$

$\mathbf{q}'$ is a low-amplitude perturbation to the time-average $\overline{\mathbf{q}}$,

$$\overline{\mathbf{q}}(r,\theta) = (\overline{u}_x(r,\theta), 0, 0, \overline{\rho}(r,\theta), \overline{T}(r,\theta), \frac{1}{\gamma}), \tag{4.3}$$

[1]The three thermodynamic variables ρ, T and p are included here for completeness. Of course, any two of these determine the third.

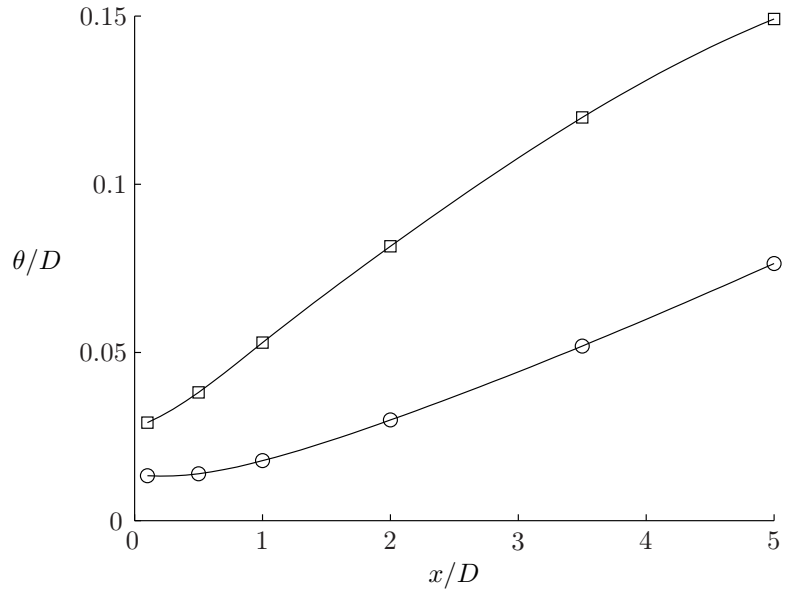

Figure 4.2: Momentum thickness of the (○) round jet and (□) (azimuthally-averaged) serrated jet.

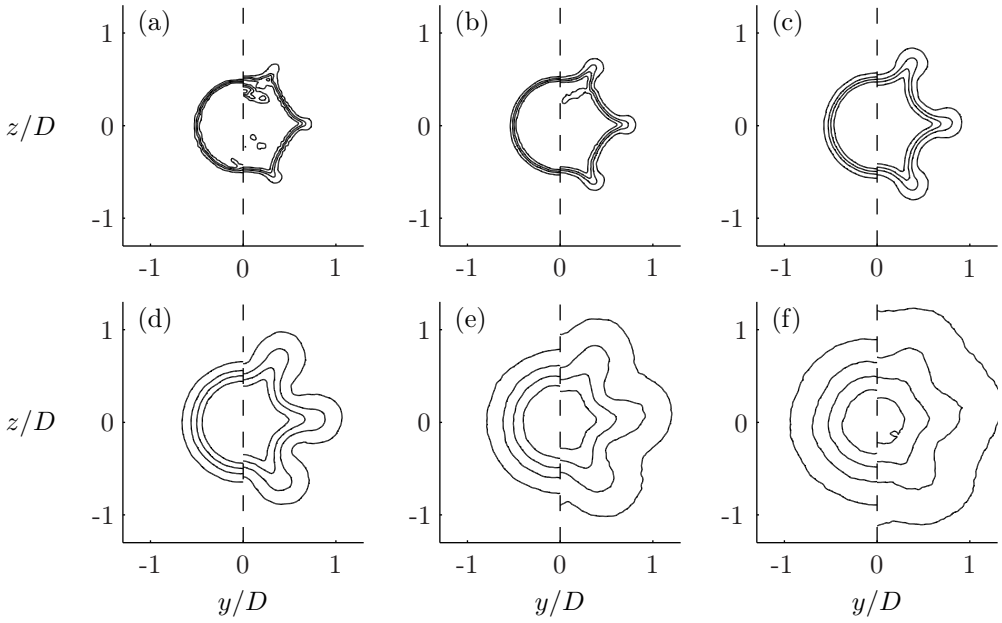

Figure 4.3: Ensemble-averaged PIV measurements of streamwise velocity $\overline{u}_x$ for the (left) round and (right) serrated nozzles. Cross-sections (a)-(f) are taken at axial stations $x/D = 0.1, 0.5, 1.0, 2.0, 3.5$ and 5.0, respectively. Contour levels are in even increments from 0.1 to $0.9U_{jet}$. $M_\infty = 0.9$, $T_{jet}/T_\infty = 0.85$, and $Re = 1.6 \cdot 10^6$ (SP7 in table 2.1).

where, in contrast to treatment for the round jet, we now include azimuthal inhomogeneities. For clarity of presentation we drop the prime on fluctuating variables in what follows, retaining the overline to denote the mean variable. Since the mean flow is homogeneous in the streamwise direction x and time t, it follows that the perturbations may be decomposed as

$$\mathbf{q}(\mathbf{x},t) = \widetilde{\mathbf{q}}(r,\theta)\, e^{i\alpha x}\, e^{-i\omega t}, \tag{4.4}$$

so that the solution $\mathbf{q}(\mathbf{x},t)$ is wavelike in x and t. α and ω are in general complex. α_r and ω_r denote wavenumber and frequency, respectively, while α_i and ω_i denote spatial and temporal growth rates, respectively.

There are two common approaches to the stability problem. In the temporal approach, we assume α is real and search for temporally unstable solutions (disturbances grow in time at a fixed location), while in the spatial approach, we assume ω is real and search for spatially unstable solutions (disturbances grow in the flow direction at a fixed time). The spatial approach is physically akin to a disturbance being excited at a fixed location, growing as it moves with the flow and is thus more relevant to the analysis of convectively unstable flows such the jet (Huerre & Monkewitz, 1990).

Substituting the decomposition in equation (4.4) into the linearized system of equations (2.37) - (2.42) and eliminating all variables but pressure, we obtain the partial differential equation governing linear (low amplitude) pressure perturbations

$$\frac{1}{r}\frac{\partial}{\partial r}\left(r\frac{\partial \widetilde{p}}{\partial r}\right) + \frac{1}{r^2}\frac{\partial^2 \widetilde{p}}{\partial \theta^2} - f\frac{\partial \widetilde{p}}{\partial r} - g\frac{1}{r^2}\frac{\partial \widetilde{p}}{\partial \theta} - h\,\widetilde{p} = 0, \tag{4.5}$$

where the f, g and h depend on the mean flow according to

$$f(r,\theta) = \frac{2\alpha}{\alpha\overline{u}_x - \omega}\frac{\partial \overline{u}_x}{\partial r} + \frac{1}{\overline{\rho}}\frac{\partial \overline{\rho}}{\partial r} \tag{4.6}$$

$$g(r,\theta) = \frac{2\alpha}{\alpha\overline{u}_x - \omega}\frac{\partial \overline{u}_x}{\partial \theta} + \frac{1}{\overline{\rho}}\frac{\partial \overline{\rho}}{\partial \theta} \tag{4.7}$$

$$h(r,\theta) = \alpha^2 - \overline{\rho}\left(\alpha\overline{u}_x - \omega\right)^2, \tag{4.8}$$

where we have ignored the (stabilizing) effects of viscosity. Taking the azimuthal Fourier-transform of equation (4.5) we obtain

$$\frac{1}{r}\frac{d}{dr}\left(r\frac{d\hat{p}_m}{dr}\right) - \frac{m^2}{r^2}\hat{p}_m - \sum_{n=-\infty}^{\infty}\left(\hat{f}_n\frac{d}{dr} + i(m-n)\,\frac{1}{r^2}\hat{g}_n + \hat{h}_n\right)\hat{p}_{m-n} = 0, \tag{4.9}$$

where

$$\hat{p}_m(r) = \frac{1}{2\pi}\int_0^{2\pi}\widetilde{p}(r,\theta)\,e^{-im\theta}\,d\theta, \tag{4.10}$$

and

$$\widetilde{p}(r,\theta) = \sum_m \hat{p}_m(r)\,e^{im\theta}, \tag{4.11}$$

and similarly for other variables.

The serrated jet of this study has $N_l = 6$ lobes. Figure 4.4 (a) shows the normalized kinetic energy-spectrum $||\hat{\overline{u}}_j||^2/||\hat{\overline{u}}_0||^2$, where $\hat{\overline{u}}_j$ is the j-th azimuthal Fourier-coefficient of $\overline{u}_x$,and the energy norm is defined as

$$||\hat{\overline{u}}_j||^2 = \int_0^{\infty}|\hat{\overline{u}}_j|^2\,rdr. \tag{4.12}$$

As expected the spectrum is dominated by the axisymmetric component, followed by $j = 6$ and 12. There is negligible energy in modes that are not multiples of six so we can neglect such terms with little error:

$$\overline{u}_x(r,\theta) = \sum_j \hat{\overline{u}}_j\,e^{ij\theta} \tag{4.13}$$

$$\approx \sum_j \hat{\overline{u}}_{6j}\,e^{i6j\theta}. \tag{4.14}$$

This is illustrated in figure 4.4 (b), showing contours of $\overline{u}_x$ at $x/D = 1$ for both the full expansion of equation (4.13) and the approximation in equation (4.14).

For general $\overline{u}_x(r,\theta)$ the system (4.9) of ODEs is potentially dense (large number of equations needed for convergence). For the serrated jet however it is sparse as the functions f, g and $h(r,\theta)$ in equations (4.6) through (4.8) inherit the symmetry of $\overline{u}_x$. This simplifies the convolutions in

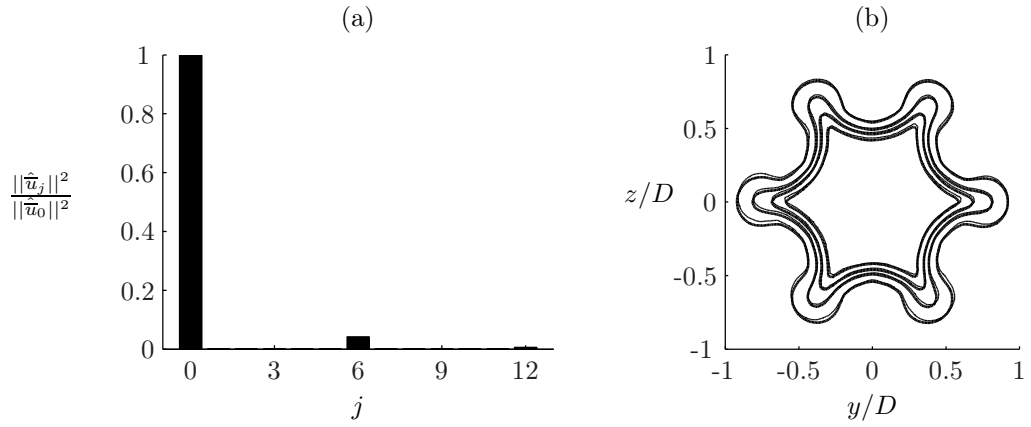

Figure 4.4: (a) Normalized kinetic energy-spectrum for the serrated-jet mean flow at $x/D = 1$. (b) Contours of (——) filtered and (——) unfiltered mean flow $\overline{u}_x$, where in filtering we retain only modes in multiples of 6. Contour levels are in even increments from 0.1 to $0.9U_{jet}$.

system (4.9) in that $\hat{f}_n(r) = 0$ if $n \neq kN_l$ where k is any integer; similarly for $\hat{g}_n(r)$ and $\hat{h}_n(r)$. Using this in system (4.9) and truncating the summation we obtain the *Rayleigh system for a serrated jet with N_l lobes:*

$$\frac{1}{r}\frac{d}{dr}\left(r\frac{d\hat{p}_m}{dr}\right) - \frac{m^2}{r^2}\hat{p}_m - \sum_{j=N}^{N}\left(\hat{f}_{N_l j}\frac{d}{dr} + i(m-N_l j)\,\frac{1}{r^2}\hat{g}_{N_l j} + \hat{h}_{N_l j}\right)\hat{p}_{m-N_l j} = 0, \tag{4.15}$$

where the summation limit N depends on the azimuthal complexity of the mean flow, starting with $N = 0$ for the round jet.

As is evident from the Rayleigh-system (4.15), the lobes of the serrated jet couple certain instability modes. As an example, consider the case where $m = 0$, and $N_l = 6$: $\hat{p}_0$ depends upon $\hat{p}_{-6}$, $\hat{p}_6$ and so forth. This is illustrated in table 4.1, which shows how the different azimuthal modes are coupled when $N_l = 6$.

The set of 1D-eigenfunctions $\{\hat{p}_{m-N_l j}\}_{j=-N}^{N}$, constituting the solution to the Rayleigh-system, combines to form a 2D-eigenfunction in r-θ space as

$$\widetilde{p}(r,\theta|m) = \sum_{j=-N}^{N}\hat{p}_{m-N_l j}(r)\,e^{i(m-N_l j)\theta}. \tag{4.16}$$

The m in $\widetilde{p}(r,\theta|m)$ is not meant to demarcate $\widetilde{p}(r,\theta|m)$ as being the m-th azimuthal component

Input m	Coupled modes							
0	...	-12	-6	0	6	12	...	
1	...	-11	-5	1	7	13	...	
2	...	-10	-4	2	8	14	...	
3	...	-9	-3	3	9	15	...	
4	...	-8	-2	4	10	16	...	c.c. of $m = -2$
5	...	-7	-1	5	11	17	...	c.c. of $m = -1$
⋮				⋮				⋮

Table 4.1: The coupling of serrated-jet azimuthal modes when $N_l = 6$. Note that the solution for $+m$ is the complex-conjugate (c.c.) of that for $-m$.

of the overall perturbation $\widetilde{p}(r,\theta)$ in equation (4.5), as is the case for round jets. For the serrated jet, m denotes the lowest-order azimuthal mode in the coupled set $\{\hat{p}_{m-N_l j}\}_{j=-N}^{N}$ that results from Fourier-transforming equation (4.5) at any of the azimuthal wavenumbers $\{m - N_l j\}_{j=-N}^{N}$. We use this terminology in what follows.

Given that the solution for $+m$ is the complex-conjugate of that for $-m$, we can deduce from table 4.1 that we need only consider $\widetilde{p}(r,\theta|m)$ for $m = 0$ through $m = 3$. We can then rewrite the decomposition of $\widetilde{p}$ in equation (4.11):

$$\begin{aligned} \widetilde{p}(r,\theta) &= \sum_k \hat{p}_k(r)\, e^{ik\theta} \\ &= \sum_{m=-3}^{3} \widetilde{p}(r,\theta|m), \end{aligned} \tag{4.17}$$

where we note that, for the round jet, $\widetilde{p}(r,\theta|m) = \hat{p}_m(r)\exp(im\theta)$.

It is well known that an axisymmetric shear layer with a single inflectional point has at most one unstable mode for each (m,ω) pair (Batchelor & Gill, 1962). While the azimuthal modes of the serrated jet are such that we only need to consider $m = 0$-3 (for $N_l = 6$), it is possible to have more than one unstable solution for each m, so that we obtain a series of coupled sets $\{\hat{p}^k_{m-N_l j}\}_{j=-N}^{N}$, where k denotes the set corresponding to eigenvalue α^k. This is indeed the case, as we shall see in section 4.3.

As $r \to 0$ and $r \to \infty$, the modes $\hat{p}_m$ of system (4.15) uncouple, each of them independently obeying the round-jet Rayleigh equation (2.50). We have already determined the boundary conditions

for this case and they are given by equations (2.52) and (2.53).

System (4.15), along with boundary conditions, equations (2.52) and (2.53), forms the two-point boundary value problem constituting the linear stability problem for the serrated jet. We solve this problem in the two ways described in section 2.3.1, via shooting and via a matrix value solver. Some of the details of these are respectively described in section A.1.3 and section A.2.

4.3 Effects of Nozzle Serrations on Stability Characteristics

4.3.1 The Experimental Jets

We solve the linear stability problem (LST) for the round and serrated jets at acoustic Mach number $M_\infty = 0.9$, temperature ratio $T_{jet}/T_\infty = 0.85$, and Reynolds number $Re = U_{jet}D/\nu_{jet} = 1.6 \cdot 10^6$. This corresponds to flow condition SP7 in table 2.1. The mean flow $\overline{u}_x$ is obtained from ensemble-averaged stereo-PIV measurements performed at NASA-Glenn's SHJAR facility. The PIV data is obtained on a Cartesian grid, giving the mean flow as a function of y and z (see coordinate system in figure 2.1). As described in the previous section, we require the mean flow $\overline{u}_x$ on a polar grid. We interpolate between the two systems using cubic splines, obtaining $\overline{u}_x(r, \theta)$ from $\overline{u}_x(y, z)$. Radial derivatives were then computed using fourth-order central differences while azimuthal derivatives were computed in Fourier-space. Refer to discussion in section 2.5.1 for more information on the data treatment.

4.3.2 The Eigensystems of the Two Jets

Figure 4.5 shows the eigenvalue spectra at cross-sections $x/D = 0.5$ and 2, at frequency $St = 0.35$. These results were obtained via the direct method (described in section A.2), which computes the entire spectrum of the Rayleigh operator. As a shorthand in the following discussion let us respectively refer to the unstable modes of the round and serrated jets as "r-modes" and "s-modes". However, when discussing a single jet at length we will drop the distinction.

First we note the number of unstable modes observed for the two jets. For the round jet there

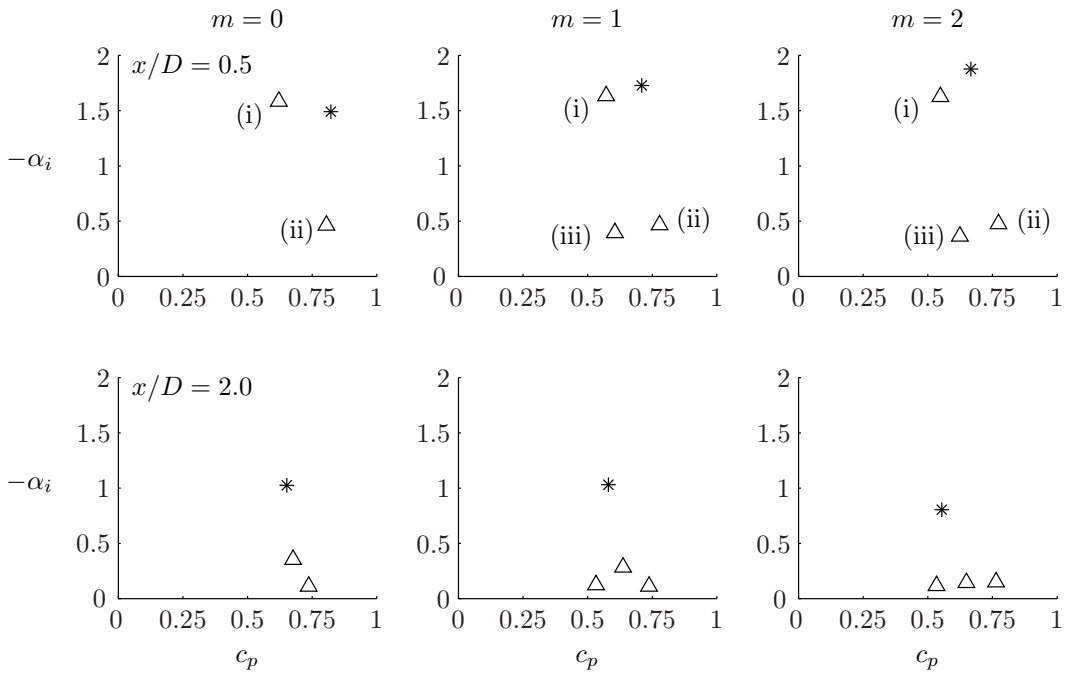

Figure 4.5: Eigenspectra of the ($*$) round and ($\triangle$) serrated jets at frequency $St = 0.35$. Eigenfunctions $\widetilde{p}(r, \theta|m)$ corresponding to modes (i)-(iii) are shown in figure 4.8.

is only a single unstable mode for each azimuthal wavenumber m and frequency St, as has been shown in the past (*e.g.*, Batchelor & Gill, 1962; Mattingly & Chang, 1974). This is not the case for the serrated jet, which has one additional mode for $m = 0$ (recall from the previous section that an s-mode with $m = 0$ is not necessarily axisymmetric; see equation (4.16)), and two additional modes for $m = 1$, 2, and 3 (not shown). $m = 4$ is coupled with $m = 2$ so that any statement about either one includes the other (see table 4.1).

Second, we note the growth-rates $-\alpha_i$ and phase-speeds $c_p = \omega/\alpha_r$ of the two sets of modes. Near the nozzle, the most unstable s-mode for $m = 0$ has a higher growth-rate than the r-mode but this is the only instance where this occurs, at this frequency. At $x/D = 2$ the s-modes are all considerably more stable than the r-mode. The most unstable s-modes have a lower phase-speed than the r-modes in all cases at $x/D = 0.5$, while the more stable s-modes generally straddle the phase-speed of the r-mode. At $x/D = 2$, however, the most unstable s-mode now has a higher phase-speed than the r-mode.

We thus see significant evolution in the stability characteristics of the serrated jet between $x/D =$

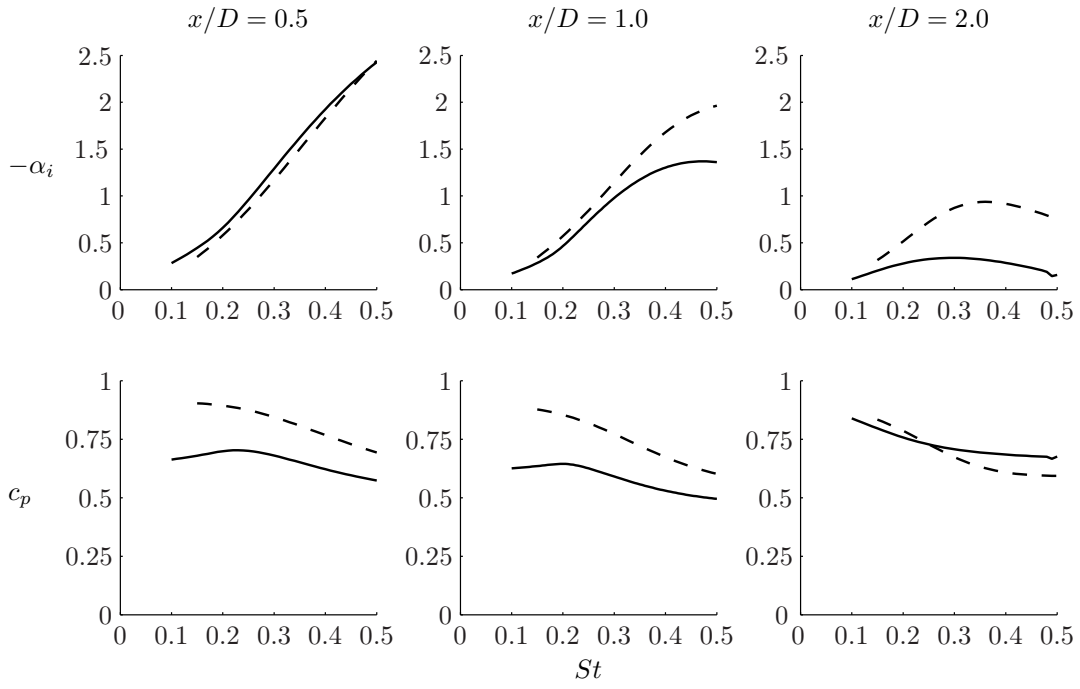

Figure 4.6: Growth-rates $-\alpha_i$ and phase-speeds $c_p = \omega/\alpha_r$ for the (- - -) r-mode and (——) the most unstable s-mode, at $m = 0$.

0.5 and 2. The s-modes decay more rapidly than the r-modes and their phase-speed changes as well. We might also ask how this changes as function of frequency. Figure 4.6 shows the growth-rates and phase-speeds of the most unstable s-mode, and the r-mode ,for $m = 0$ at $x/D = 0.5, 1$ and 2. These results are computed via the shooting method. The most unstable s-mode is again observed to have a higher growth-rate at $x/D = 0.5$, although a cross-over occurs at $St = 0.5$. At $x/D = 1$ the s-mode has a lower growth-rate at all frequencies of interest and decays even more rapidly thereafter. The s-mode has a lower phase-speeds than the r-mode, although a cross-over is observed at $x/D = 2$. The significance of the phase-speeds of the different modes is discussed in the next section.

In addition to noting the number of unstable modes and their relative coordinates in spectral-space, we are also interested in their respective eigenfunctions $\widetilde{p}(r, \theta|m)$, which represent the inverse transform (from (r, m) to (r, θ)) of the radial eigenfunctions $\{\hat{p}_{m-N\imath j}(r)\}_{j=-N}^{N}$, the solution of the Rayleigh-system. As there is more than one unstable s-mode, let us enumerate them by index k as $\widetilde{p}^k(r, \theta|m)$.

Figure 4.7 shows the eigenfunctions $\widetilde{p}(r, \theta|m)$ for the round jet at $x/D = 0.5$. Shown are azimuthal

modes $m = 0$-2, which have the expected monopole, dipole and quadrupole behavior, respectively. The s-modes at $x/D = 0.5$ in figure 4.5 are labeled (i)-(iii); their respective eigenfunctions are shown in figure 4.8. Let us first compare $\widetilde{p}^1(r, \theta|m)$ with the r-modes. First to note is the considerably more complex azimuthal structure of the s-modes. Away from the shear layer they are similar however. The s-mode for $m = 0$, for example, is axisymmetric near the axis and in the far field. Even within the shear layer the r- and s-modes are similar in that both are dominated by their respective m-type behavior (*e.g.*, $m = 1$ is a modified dipole). We can rewrite equation (4.16) as

$$\begin{aligned} \widetilde{p}(r, \theta|m) &= \sum_{j=-N}^{N} \hat{p}_{m-N_l j}(r)\, e^{i(m-N_l j)\theta} \\ &= \left(\sum_{j=-N}^{N} \hat{p}_{m-N_l j}(r)\, e^{-iN_l j\theta} \right) e^{im\theta}, \end{aligned} \tag{4.18}$$

while that for the round jet is simply

$$\widetilde{p}(r, \theta|m) = \hat{p}_m(r)\, e^{im\theta}. \tag{4.19}$$

This illustrates two things. First, we see more clearly how the serrated-jet eigenfunction in equation (4.16), rewritten as equation (4.18), is an extension of that for the round jet. Secondly, we see that the $j \neq 0$ components of the sum in equation (4.18) are mostly supported within the shear layer, decaying rapidly outside of it.

The remaining s-modes in figure 4.5 (ii-iii) are qualitatively similar, at least superficially. Differences can be noted from their contours, however. For example, mode (ii) decays radially at a lower rate, and (iii) at a higher rate than (i). There is another and more subtle difference between the modes: their orientation. In particular, mode (ii) seems rotated by 30° compared with mode (i). This is significant as the orientation is relative to the mean flow. This serves as a hint as to their respective origins, discussed in the next section.

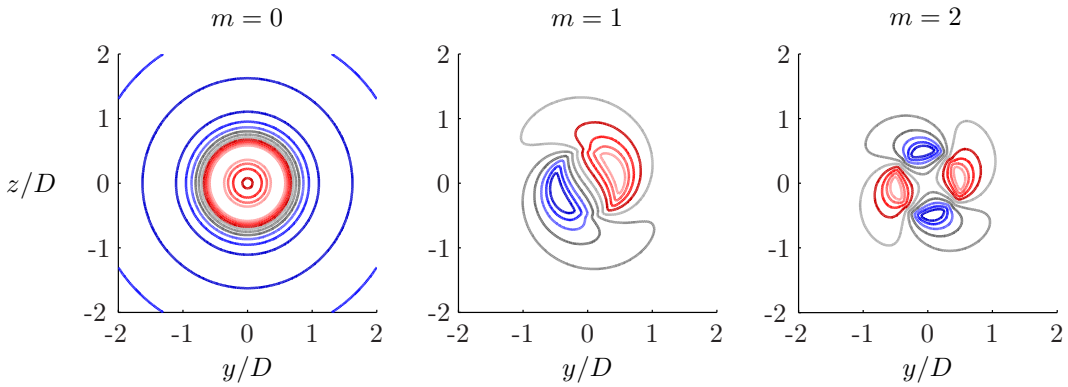

Figure 4.7: Eigenfunctions $\widetilde{p}(r, \theta|m)$ of the round jet at $x/D = 0.5$ and $St = 0.35$.

4.3.3 Comparison along Radial Slices

In this section we consider radial sections of the serrated-jet eigenfunctions $\widetilde{p}^k(r, \theta|m)$ in figure 4.8. From the contours we observed some differences in terms of radial decay-rates, azimuthal complexity (*i.e.*, the relative magnitude of the $j \neq 0$ components of the eigenfunction in equation (4.18)), and orientation. The orientation is significant as it is relative to the mean flow.

The mean flow of the serrated jet has two extremal radii θ_j, shown in figure 4.9 (a), along with the contours of the mean flow at $x/D = 0.5$. The $\theta_1 = 0°$ radius passes through the center of a lobe, coinciding with the azimuthal location of the maximal azimuthal shear $\partial_\theta \overline{u}_x$, and the minimal radial shear $\partial_r \overline{u}_x$. The $\theta_2 = 30°$ radius passes through the middle of the valley between two lobes and coincides with $\min_\theta \partial_\theta \overline{u}_x$ and $\max_\theta \partial_r \overline{u}_x$. Figure 4.9 (b) shows the mean flow evaluated along the two radial sections; the differing radial shear is apparent.

Figure 4.10 shows the amplitude of the s-modes $\widetilde{p}^k(r, \theta|m)$, evaluated along the two radii. The eigenfunctions have arbitrary normalization; here we have normalized the two sections such that the maximum of the two is unity. Their relative magnitude is then set by the Rayleigh-system.

The first observation we make is that the first mode $\widetilde{p}^1(r, \theta|m)$ peaks at θ_2 for all m, while the second and third modes peak at θ_1. The first and most unstable s-mode is thus principally associated with radial shear—azimuthal vorticity—and is akin to the r-mode. The higher s-modes are principally associated with azimuthal shear—streamwise vorticity—and no analogous r-mode

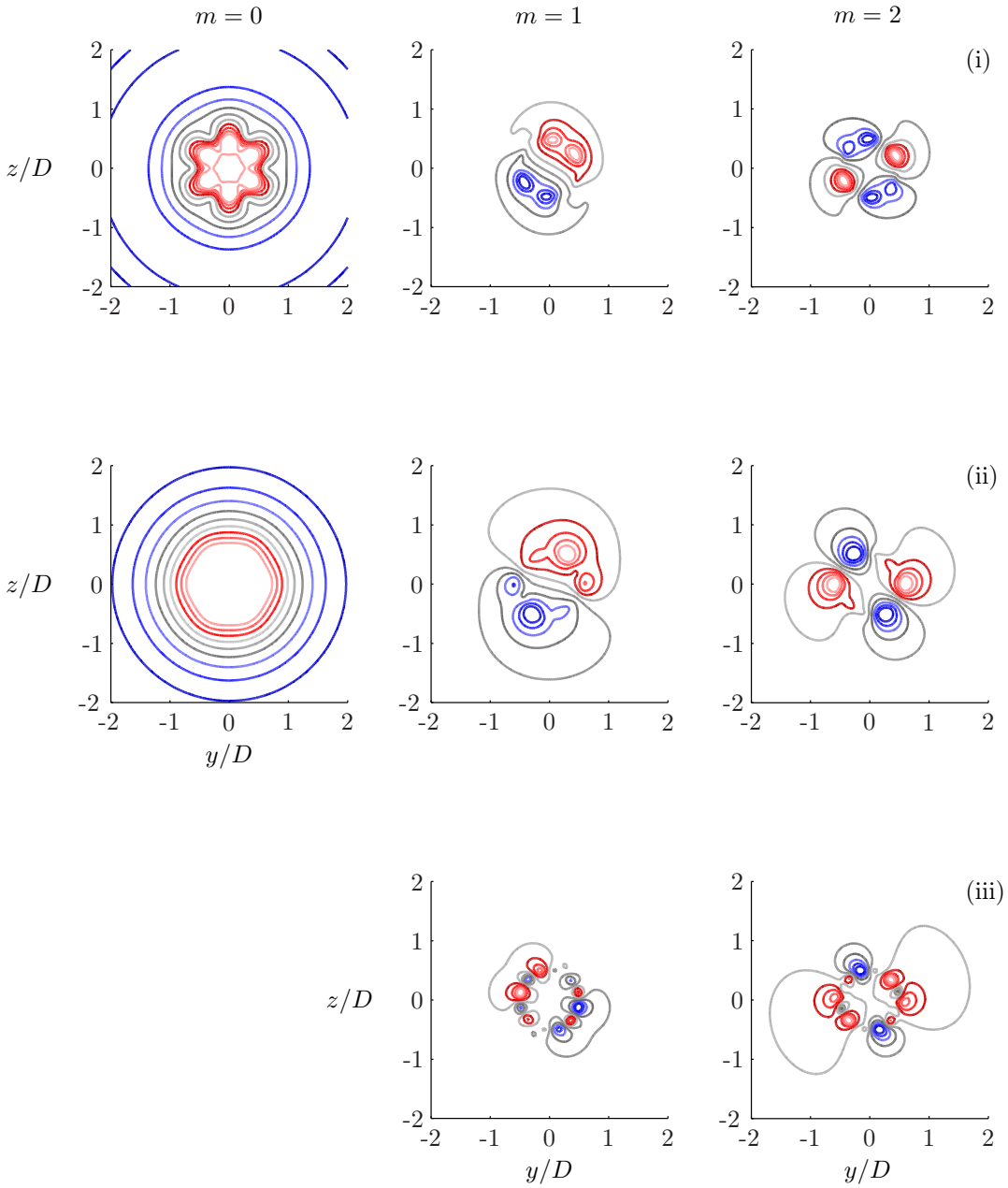

Figure 4.8: Eigenfunctions $\widetilde{p}(r, \theta|m)$ (from equation (4.16)) of the serrated jet at $x/D = 0.5$ and $St = 0.35$. Modes (i)-(iii) correspond respectively to numbered modes in figure 4.5.

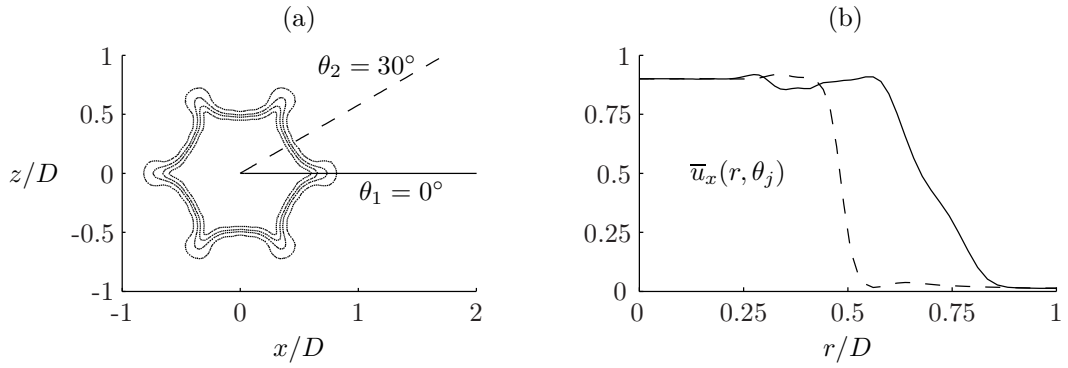

Figure 4.9: (a) Contours of the serrated-jet mean flow $\overline{u}_x$ at $x/D = 0.5$, overlaid with the two radii (——) $\theta_1 = 0°$ and (- - -) $\theta_2 = 30°$. (b) $\overline{u}_x$ evaluated along the two radii.

exists.

The second observation we make regards phase-speed. We focus on the s-mode for $m = 0$; analogous observations can be made for $m = 1$ and 2. Note the radial location of peak-pressure from figure 4.10. The second mode peaks at a larger radius than the first. Figure 4.11 shows the peak-locations in relation to the mean flow, along the two radial sections. At $\theta = 0°$ the dominant, streamwise-vorticity mode peaks where the mean flow is flowing at $\overline{u}_x \approx U_{jet}$. At $\theta = 30°$ the dominant, azimuthal-vorticity mode peaks at $\overline{u}_x \approx 0.4U_{jet}$. Remember that instability waves are convected with the flow. The convection speed is not constant, however, and varies as the mean flow varies with radial location. The phase-speed of a mode is thus a weighted average of the mean-flow velocity across the support of that mode, the weights being determined by the Rayleigh-equation. This is why the phase-speeds of the first and second modes are not $0.4U_{jet}$ and U_{jet}, respectively according to $\overline{u}_x$ where these modes peak. The $\overline{u}_x$ at peak-pressure will however weigh heavier than others, and serves as a proxy to phase-speed. This explains the lower phase-speed of the first s-mode as compared to the second. Figure 4.12 show analogous results for the round jet. The $m = 0$ mode peaks where $\overline{u}_x \approx 0.7U_{jet}$, explaining why it has a higher phase-speed than the first s-mode, and a lower phase-speed than the second s-mode. Additionally, the r-modes of $m = 0$, 1, and 2 have successively decreasing $\overline{u}_x$ at their respective peaks, again consistent with the spectral information in the previous section.

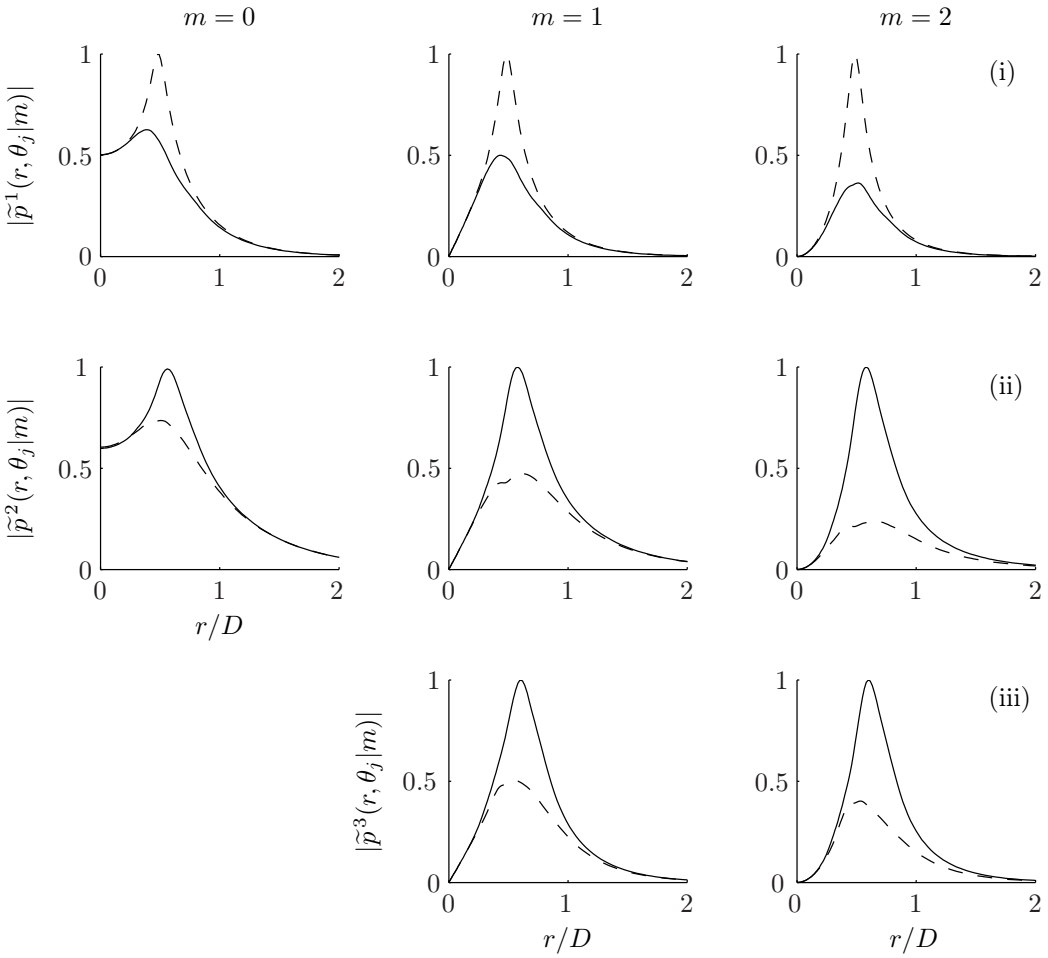

Figure 4.10: Serrated-jet eigenfunctions $\widetilde{p}(r, \theta|m)$ evaluated along the two radii (——) $\theta_1 = 0°$ and (– – –) $\theta_2 = 30°$. Modes (i)-(iii) correspond respectively to numbered modes in figure 4.5.

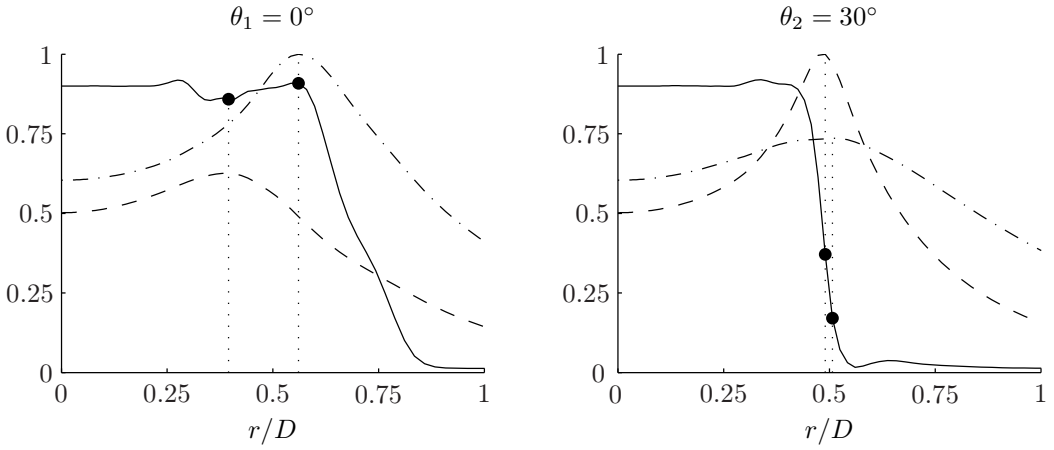

Figure 4.11: (——) Serrated-jet mean flow $\overline{u}_x$ and amplitude of eigenfunctions (– – –) $\widetilde{p}^1(r, \theta|m = 0)$ and (–·–·–) $\widetilde{p}^2(r, \theta|m = 0)$, evaluated along $\theta = 0°$ and 30°. Note (•) values of $\overline{u}_x$ where eigenfunctions peak. $x/D = 0.5$ and $St = 0.35$.

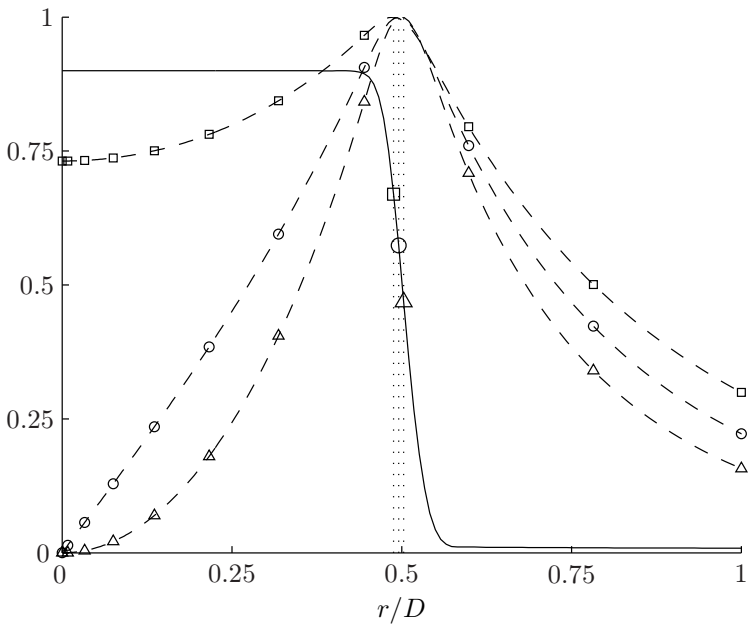

Figure 4.12: (——) Round-jet mean flow $\overline{u}_x$ and amplitude of eigenfunctions (□) $\widetilde{p}(r,\theta|m=0)$, (○) $\widetilde{p}(r,\theta|m=1)$, and (△) $\widetilde{p}(r,\theta|m=2)$. $x/D=0.5$ and $St=0.35$.

4.4 Comparison with Experiments

Here we compare the predictions of LST to pressure measurements made in the the facility described in section 2.5.2. These measurements are from the same set of data as used in chapter 3; please refer to section 3.1 for further details thereunto. LST amplitudes are determined via amplitude-matching, described in section 3.2.2.

4.4.1 Microphone Data

In comparing the LST predictions with the microphone measurements we are faced with the question of how to combine the azimuthal- and streamwise-vorticity modes to make up an instability wave. After all, the combined instability wave, the one in the data, will be the sum of all instabilities (and other fluctuations) within the data. As the streamwise-vorticity modes are associated with the azimuthal structure of the mean flow, they only persist up to roughly half the potential-core length. In addition, they have much lower growth rates than the azimuthal-vorticity modes, on which we focus.

Figures 4.13 and 4.14 respectively show the evolution of pressure amplitude and phase-angle for the two jets, at azimuthal wavenumbers $m = 0$ and frequencies $St = 0.25$, 0.35, and 0.50. Note the distinctive shape of the LST prediction for the serrated jet. Remaining flat up to roughly $x/D = 1$, it jumps somewhat abruptly to reach a peak shortly after $x/D = 2$, while the round jet prediction develops more smoothly. The reason for this lies with the geometry of the microphone array, as compared to the eigenfunctions. This is illustrated in figure 4.15, which shows the amplitude-contours of the eigenfunctions for the two jets, along with the microphone array.

The phase-angle predictions for the two jets are very similar and comparable to those described in chapter 3. Amplitude predictions are similarly comparable, although the data for serrated jet seems contaminated beyond that for the round jet. Both jets suffer acoustic contamination, particularly after saturation, but the serrated jet has an additional ring-to-ring zig-zag pattern. Similar observations can be made for the $m = 1$ mode, shown in figures 4.16 and 4.17.

Figure 4.18 shows contours of total-turbulence (root-mean-square of all velocity fluctuations from PIV) at $x/D = 2$ for the two jets, along with the microphone ring at the same location. Due to its higher spread-rate, the serrated jet is closer to the array, which explains the higher pressure-levels observed in the data. To minimize aliazing in the data, each ring is shifted azimuthally by 30° relative to the adjacent rings. The figure shows how this shift can place the microphones on one ring closer to the mean flow than those on the next, potentially explaining the zig-zag pattern observed in the data.

4.4.2 POD-Filtered Data

As in chapter 3 we perform a POD of the microphone data. Figure 4.19 shows the POD energy-spectra of two jets. These spectra have been normalized by the total energy of each mode (m, ω). The ratio $\lambda_j / \sum_{k=1}^{N} \lambda_k$ thus represents the fraction of energy contained in POD-mode j. The spectral-decay of the serrated jet is considerably slower than for the round jet, and increasingly so with higher frequency. Fast spectral-decay indicates greater coherence in the data, while, in the other extreme, a randomly composed data-set has a nearly flat spectrum. The round jet is thus in some

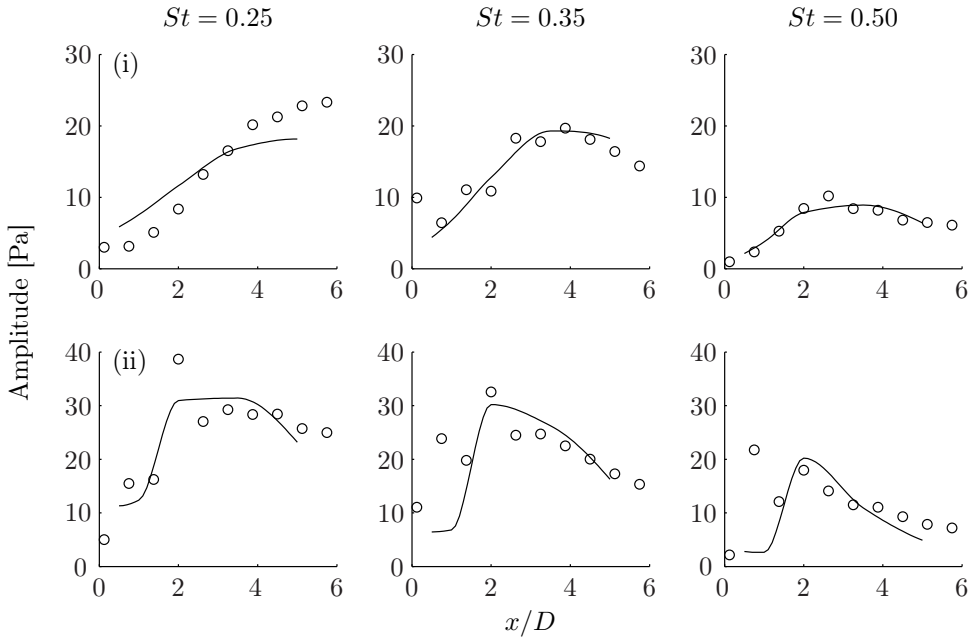

Figure 4.13: Pressure amplitude along the microphone array for the (i) round and (ii) serrated jets. Predictions of (——) LST compared with (○) measurements, at $m = 0$.

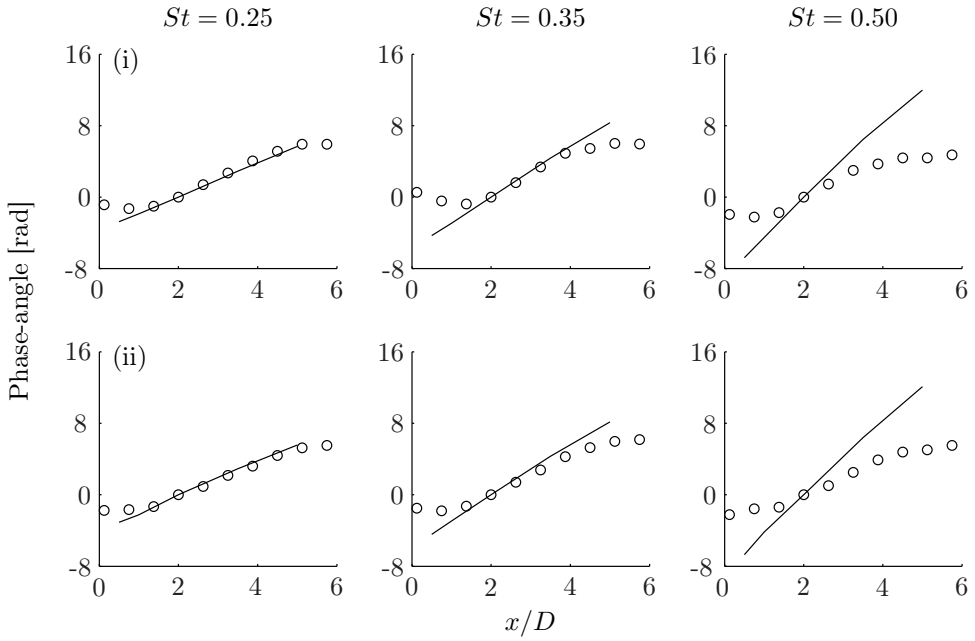

Figure 4.14: Pressure phase-angle along the microphone array for the (i) round and (ii) serrated jets. Predictions of (——) LST compared with (○) measurements, at $m = 0$.

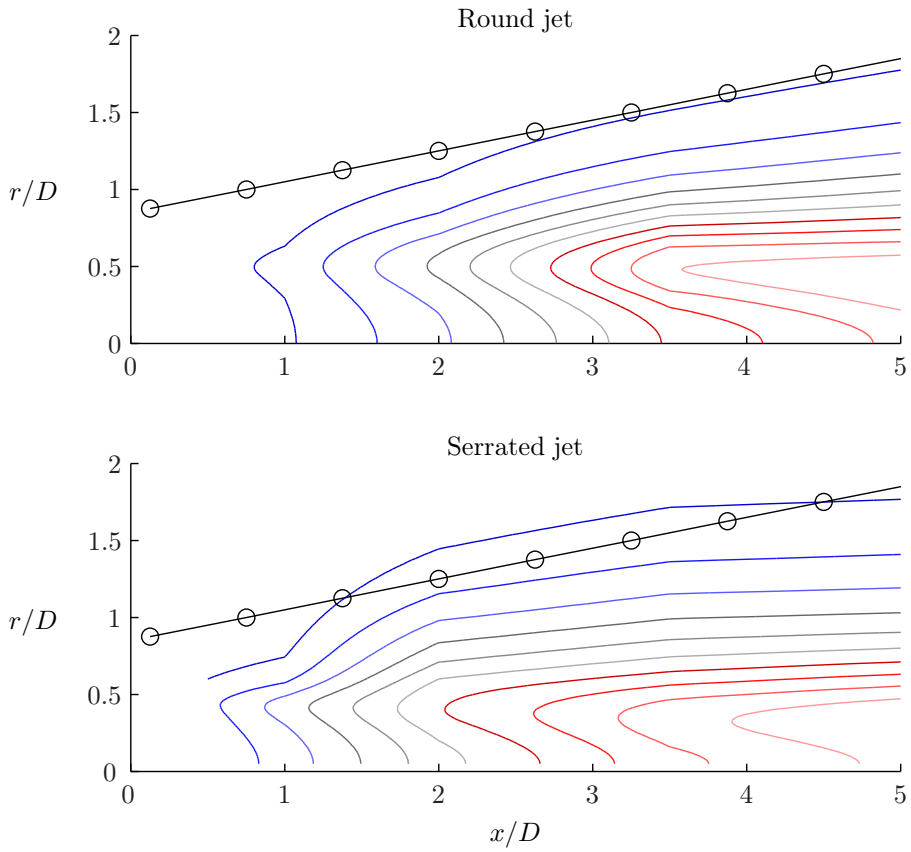

Figure 4.15: Contours of the LST eigenfunctions for the two jets, with the (○) microphone positions overlaid. $m = 0$ and $St = 0.35$.

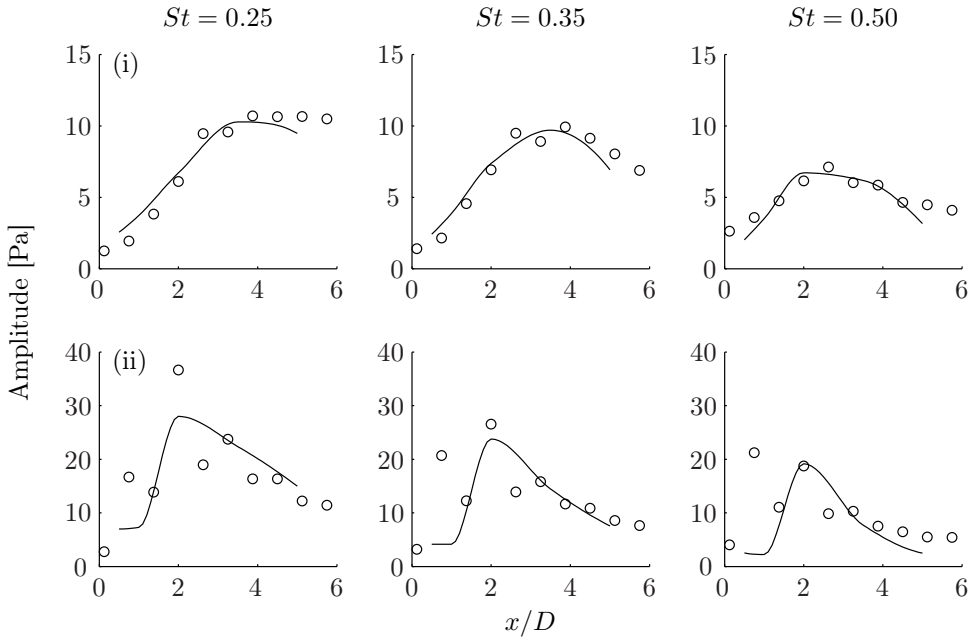

Figure 4.16: Pressure amplitude along the microphone array for the (i) round and (ii) serrated jets. Predictions of (——) LST compared with (○) measurements, at $m = 1$.

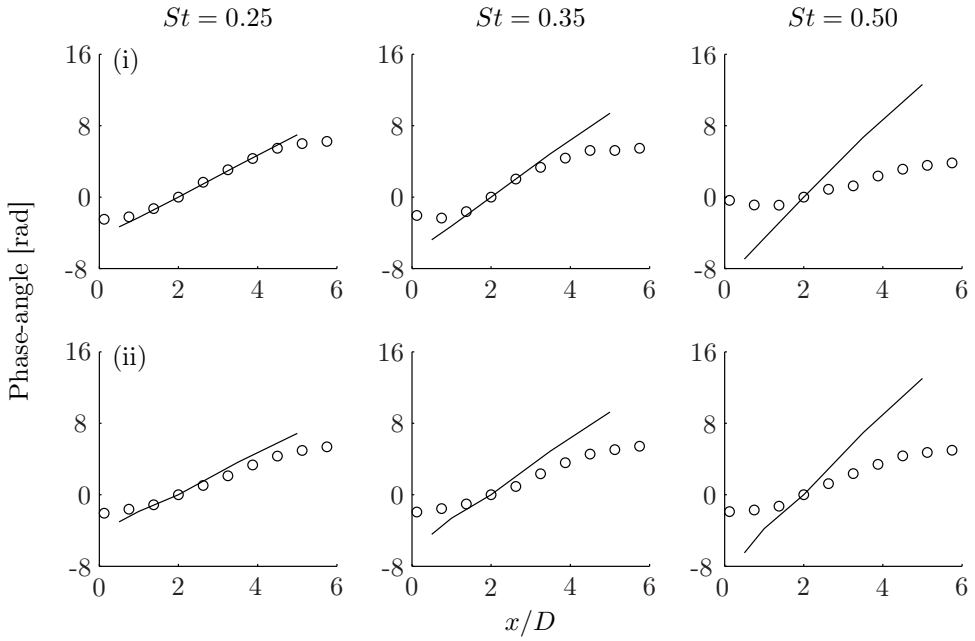

Figure 4.17: Pressure phase-angle along the microphone array for the (i) round and (ii) serrated jets. Predictions of (——) LST compared with (○) measurements, at $m = 1$.

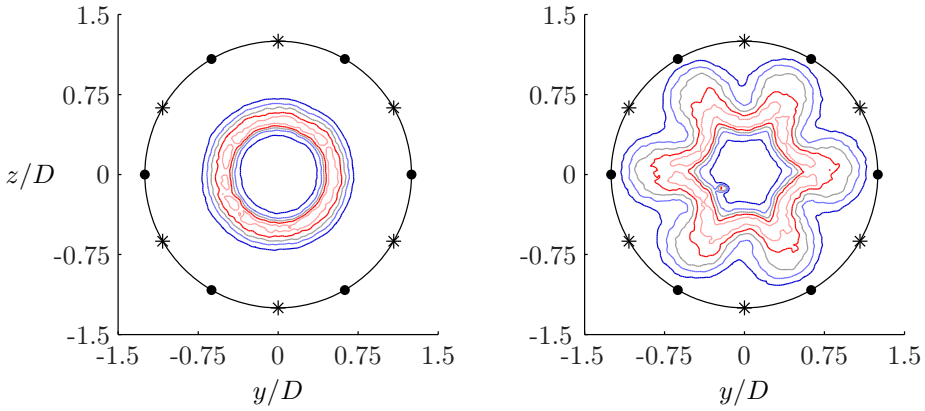

Figure 4.18: Amplitude-contours of total-turbulence levels for the (left) round and (right) serrated jets, along with the microphone ring at $x/D = 2$. The bullets on the ring denote its six microphones while the stars denote those on an adjacent ring.

sense simpler or more coherent than the other.

We now compare LST prediction to the POD-filtered measurements (see section 2.4), where only the highest-energy POD-mode is retained. Figures 4.20 and 4.21 respectively show the evolution of POD-filtered pressure amplitude and phase-angle for the two jets, at azimuthal wavenumbers $m = 0$ and frequencies $St = 0.25$, 0.35, and 0.50. Striking comparison improvements are obtained, particularly for the peak-frequency of the serrated jet ($St = 0.35$). Note that the prediction-jump around $x/D = 2$ for the serrated-jet, described in the previous section, is now visible as well in the filtered amplitude data. The phase-predictions for the two jets are both excellent.

Figures 4.22 and 4.23 show similar comparisons for $m = 1$. The improvement in comparisons is not as significant as for the $m = 0$ mode. Particularly curious are the large-amplitude jumps (or sharp peaks) for serrated jet, visible in figure 4.22 (ii). This phenomena also appears for the $m = 0$ mode but on a smaller scale. The phase-predictions are again excellent, indicating that the microphone data is again mostly comprised of instability waves. The jump is however not explained by our LST model and its origin is not clear. It is correlated with the instability waves in the flow (in the data, that is) however, and might be related to the collapse of the streamwise-vorticity modes.

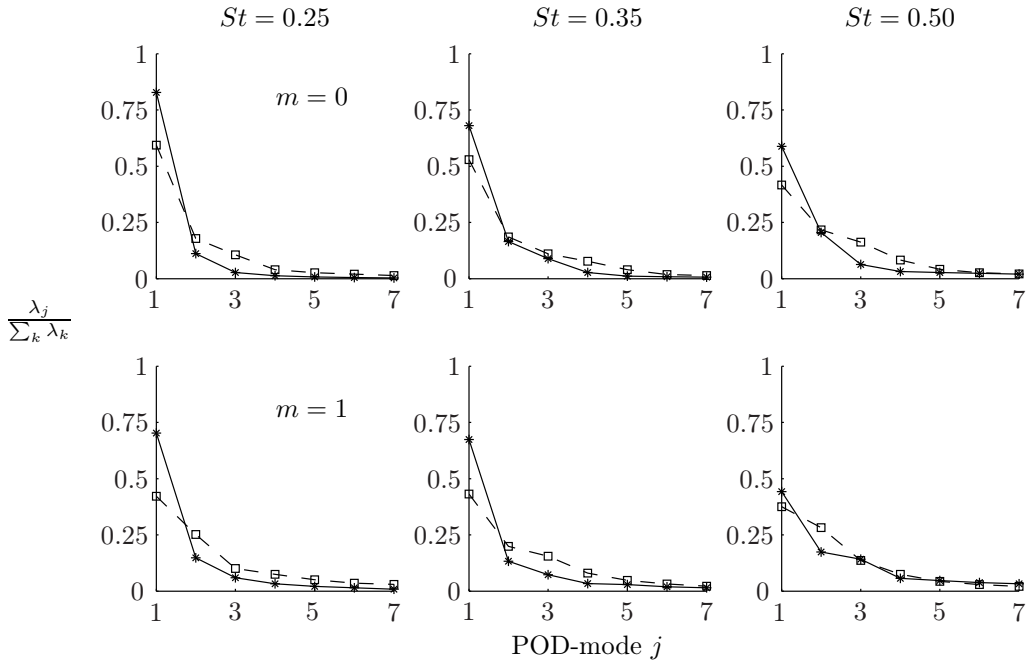

Figure 4.19: Normalized POD-spectra for the (∗) round and (□) serrated jets.

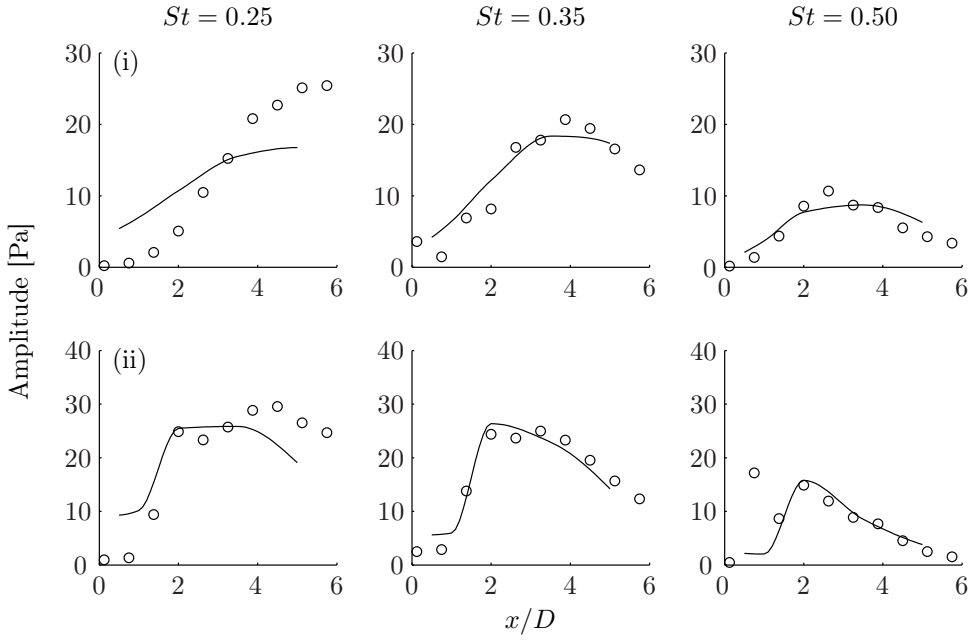

Figure 4.20: Pressure amplitude along the microphone array for the (i) round and (ii) serrated jets. Predictions of (——) LST compared with (∘) 1st POD-mode, at $m = 0$.

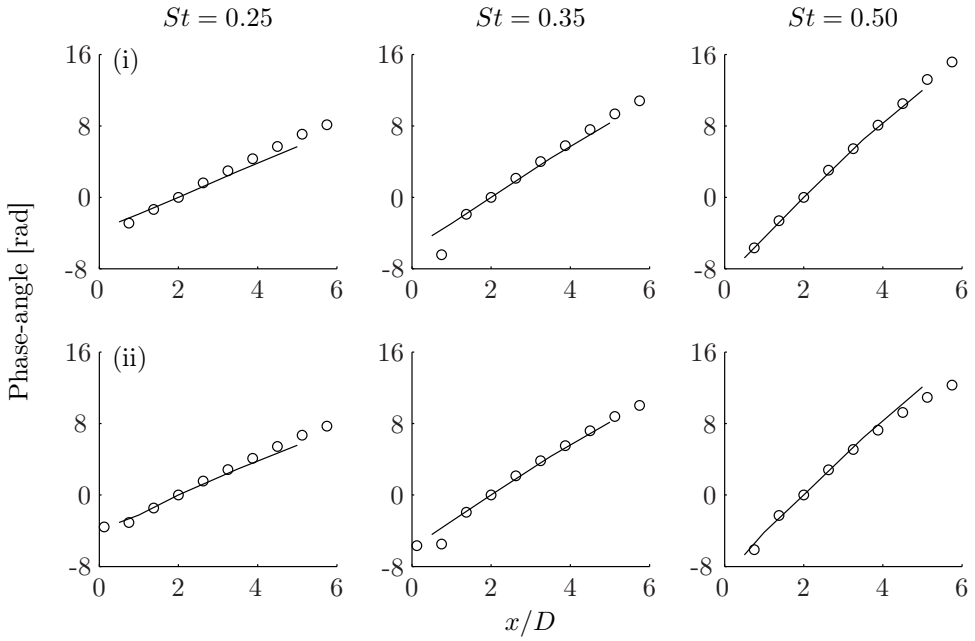

Figure 4.21: Pressure phase-angle along the microphone array for the (i) round and (ii) serrated jets. Predictions of (——) LST compared with (○) 1st POD-mode, at $m = 0$.

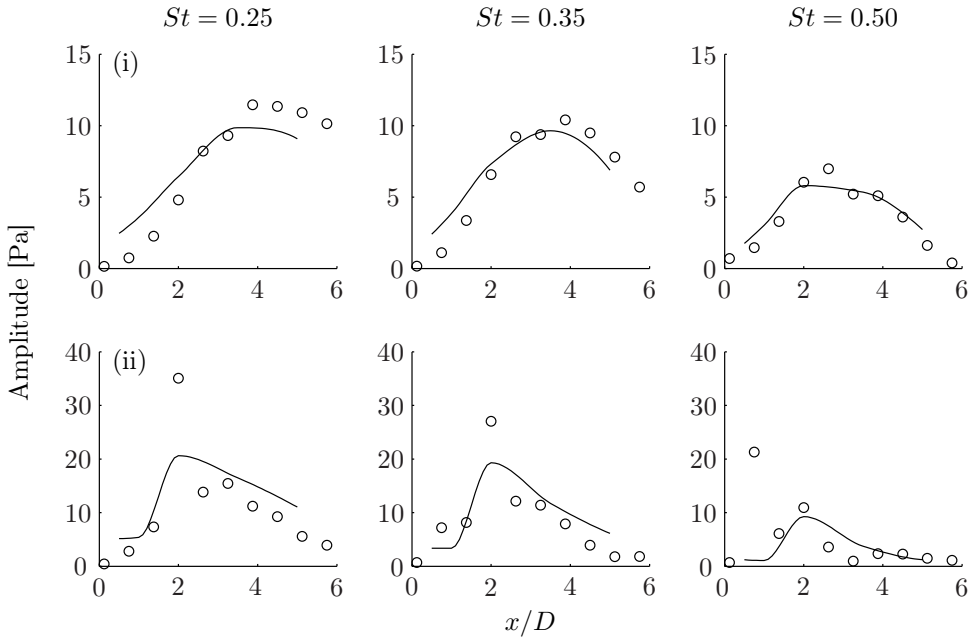

Figure 4.22: Pressure amplitude along the microphone array for the (i) round and (ii) serrated jets. Predictions of (——) LST compared with (○) 1st POD-mode, at $m = 1$.

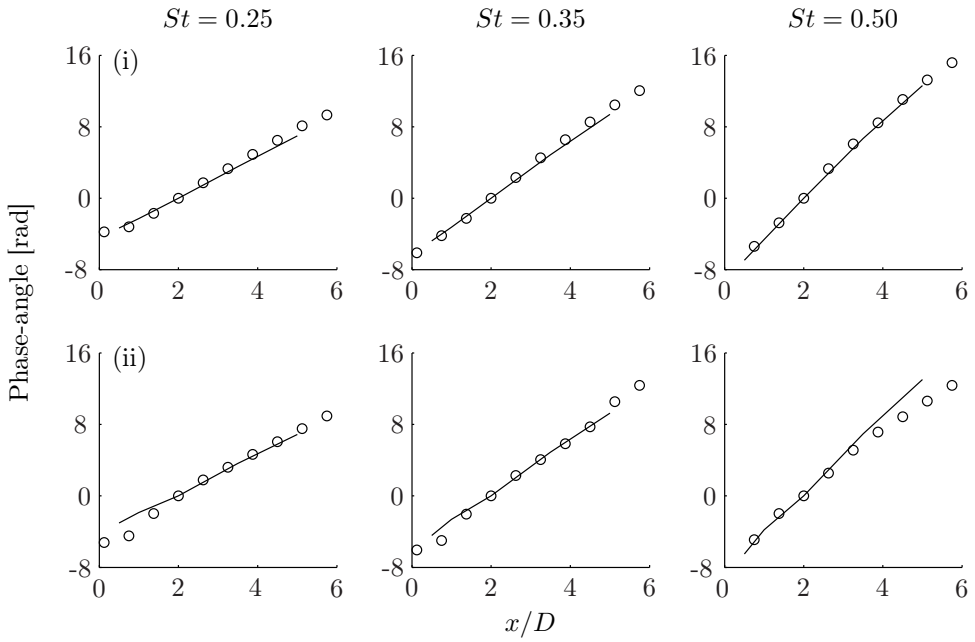

Figure 4.23: Pressure phase-angle along the microphone array for the (i) round and (ii) serrated jets. Predictions of (——) LST compared with (○) 1st POD-mode, at $m = 1$.

4.5 Summary

In this chapter we have investigated the linear dynamics of large-scale structures in the near-field of a pair of turbulent round and serrated jets. We extended the Rayleigh-equation to include azimuthal inhomogeneities. This results in a system of ordinary differential equations, the Rayleigh-system (4.15). We solve this system using both shooting and direct methods.

Using mean flows based on ensemble-averaged PIV measurements (Bridges & Wernet, 2003) we computed the stability characteristics of the two jets. We found that the serrated jet has more unstable modes than the round jet. In particular, new modes arise, associated with the azimuthal shear of the mean flow, thus corresponding to streamwise vorticity. The most unstable modes of the serrated jet are associated with the radial shear of the mean flow, corresponding to azimuthal vorticity. The streamwise-vorticity modes peaks are situated in the lobes of the serrated jet and therefore have higher phase-speed than the more unstable modes. Serrated-jet growth-rates are damped in nearly all cases.

We compared our LST predictions to near-field microphone measurements (Suzuki & Colonius,

2006) performed using the caged-array at NASA Glenn's SHJAR facility. We found the LST predictions to correspond reasonably well with the microphone measurements, particularly in terms of the phase-angle. As in the study described in chapter 3 we found the data to be contaminated by acoustic fluctuations, and this seems to affect the serrated jet more than the round jet.

As in section 3.5.3, we filtered the microphone data via the POD. The spectral-decay is considerably slower for the serrated jet than the round. This is indicative of the greater complexity or, alternatively, less coherence of the former than the latter. We compared LST predictions to the most energetic POD mode and found striking improvements for the $m = 0$ mode. Particularly impressive is the ability of the LST prediction to capture the rapid rise in amplitude (see $St = 0.35$ in figure 4.20 (ii)) that occurs do to the proximity of the array to the serrated jet (figure 4.15). The amplitude-comparison improvements for $m = 1$ are not as considerable, although the phase-prediction is excellent. The POD-filtered amplitude has a sharp peak or jump that is not reproduced by the prediction and remains unexplained. The jump is correlated with the instability waves in the flow (in the data, that is) however, and might be related to the collapse of the streamwise-vorticity modes, which are quickly stabilized.

The work in this chapter will be published in Gudmundsson & Colonius (2010*b*).

Chapter 5

Concluding Remarks

5.1 Summary

In this work we studied the linear dynamics of large-scale coherent structures in turbulent jets from round and serrated nozzles. Linear disturbances to the turbulent mean flows were modeled via linear stability analysis. Additionally, the more accurate Parabolized Stability Equations (PSE) were solved for the fluctuations of a round jet. We compared our predictions to near-field microphone measurements (Suzuki & Colonius, 2006) performed using the caged-array at NASA Glenn's SHJAR facility. By filtering out the uncorrelated fluctuations, via the proper orthogonal decomposition (POD), better agreement between data and theory was obtained.

The two sections below summarize the conclusions of chapter 3 and chapter 4.

5.1.1 Instability Wave Models of Large-Scale Pressure Fluctuations

In this chapter we investigated the linear dynamics of large-scale structures in the near-field of turbulent subsonic round jets. Using mean flows based on ensemble-averaged PIV measurements (Bridges & Wernet, 2003) we computed near-field fluctuations via the linear stability equations (LST) and the parabolized stability equations (PSE). We analyzed two pairs of hot and cold $M_\infty = 0.5$ and 0.9 jets, listed in table 2.1.

We found that LST underestimates growth-rates and overestimates wavenumbers. It thus predicts more stable and longer waves than is the case in actuality. This causes premature saturation

as the neutral-point is shifted upstream. We showed that this is due to LST's negligence of history effects, rather than the omission of additional non-parallel shear-terms such as $\partial_x \overline{u}_x$. These have only a weak effect on the evolution. The locally-parallel flow assumption affects all azimuthal modes, particularly at sub-peak frequencies. The $m = 1$ mode performs the best and is less affected than $m = 0$ and 2. This non-monotonic m-dependence of the effects of the locally-parallel flow is curious. We hypothesized that the $m = 0$ mode is impacted due to its dependence on the nozzle-diameter D, resulting in longer wavelengths. The $m \neq 0$ modes are increasingly affected by non-parallel effects: it happens that the $m = 1$ mode is the first to be independent of nozzle-diameter and as such does better than the $m = 2$ mode. Conversely, the 2D mode (zero spanwise wavenumber) in a planar mixing-layer or a flat-plate boundary layer would be the least affected by non-parallel effects as it has no special additional length-scale. This can be seen, *e.g.*, in the results of Bertolotti *et al.* (1992) who studied the Blasius boundary layer.

Next we compared pressure predictions of LST to those of PSE for the cold $M_\infty = 0.5$ jet. The LST does well at and above the peak-frequency, but great improvements by the PSE are observed at lower frequencies, particularly for $m = 0$ and 2.

We compared PSE predictions to the most energetic POD-mode. The comparisons so obtained were greatly improved, particularly for the higher-speed and heated jets which had appeared the most contaminated. For the cold jets the PSE predictions match very well, even beyond the end of the potential core. These results indicate that nonlinear interactions are mostly important in terms of their impact on mean flow evolution, at least at these flow conditions and some of the considered frequencies. We noted that this seems to run counter to the results of Mohseni *et al.* (2002) and hypothesized that the difference lies with the increased importance of modal interactions at higher speeds, due to stabilization of large-scale structures.

We observed POD-modes of mixed hydrodynamic and acoustic nature, indicating a significant correlation between hydrodynamic waves and acoustic waves. We hypothesized that the acoustic portion of these POD modes represents the Mach wave radiation of the large-scale structure. Otherwise, these components would not be consistently in phase (correlated) and could not "live" within

the same POD-mode.

The work described in chapter 3 will be published as Gudmundsson & Colonius (2010*a*).

5.1.2 The Effects of Nozzle Serrations on the Linear Stability of Turbulent Jets

In this chapter we investigated the linear dynamics of large-scale structures in the near-field of a pair of turbulent round and serrated jets. We extended the Rayleigh-equation to include azimuthal inhomogeneities. This results in a system of ordinary differential equations, the Rayleigh-system (4.15). We solve this system using both shooting and direct methods.

Using mean flows based on ensemble-averaged PIV measurements (Bridges & Wernet, 2003) we computed the stability characteristics of the two jets. We found that the serrated jet has more unstable modes than the round jet. In particular, new modes arise, associated with the azimuthal shear of the mean flow, thus corresponding to streamwise vorticity. The most unstable modes of the serrated jet are associated with the radial shear of the mean flow, corresponding to azimuthal vorticity. The streamwise-vorticity modes peaks are situated in the lobes of the serrated jet and therefore have higher phase-speed than the more unstable modes. Serrated-jet growth-rates are damped in nearly all cases.

We compared our LST predictions to near-field microphone measurements (Suzuki & Colonius, 2006) performed using the caged-array at NASA Glenn's SHJAR facility. We found the LST predictions to correspond reasonably well with the microphone measurements, particularly in terms of the phase-angle. As in the study described in chapter 3 we found the data to be contaminated by acoustic fluctuations, and this seems to affect the serrated jet more than the round jet.

We filtered the microphone data via the POD. The spectral-decay is considerably slower for the serrated jet than the round. This is indicative of the greater complexity or, alternatively, less coherence of the former than the latter. We compared LST predictions to the most energetic POD mode and found striking improvements for the $m = 0$ mode. Particularly impressive is the ability of the LST prediction to capture the rapid rise in amplitude (see $St = 0.35$ in figure 4.20 (ii)) that

occurs do to the proximity of the array to the serrated jet (figure 4.15). The amplitude-comparison improvements for $m = 1$ are not as considerable, although the phase-prediction is excellent. The POD-filtered amplitude has a sharp peak or jump that is not reproduced by the prediction and remains unexplained. The jump is correlated with the instability waves in the flow (in the data, that is) however, and might be related to the collapse of the streamwise-vorticity modes, which are quickly stabilized.

The work described in chapter 4 will be published as Gudmundsson & Colonius (2010*b*).

Appendix A

Solving the Rayleigh System

A.1 The Shooting Solution

A.1.1 The Round Jet

The Rayleigh equation (2.50), along with boundary conditions give in equations (2.52) and (2.53), prescribes the form of $\hat{p}(r)$ for the round jet. Given inputs ω, m, $\overline{u}_x$ and $\overline{\rho}$, and an initial guess for the eigenvalue α_0, the shooting procedure is as follows:

1. Generate $\hat{p}$ and its derivative at axis. Note that the Rayleigh equation has a regular singular point at $r = 0$ so we start the procedure at $0 < \epsilon \ll D$:

$$\hat{p}(\epsilon) = J_m(\beta\epsilon) \tag{A.1}$$

$$\frac{d\hat{p}}{dr}(\epsilon) = \beta J_{m-1}(\beta\epsilon) - \frac{m}{\epsilon} J_m(\beta\epsilon) \tag{A.2}$$

   where $\beta = \sqrt{\overline{\rho}(M_\infty \alpha - \omega)^2 - \alpha^2}$. Taking $\epsilon = 0.01D$ is in our experience sufficient to obtain a converged solution.

2. Integrate outwards to $r = R$, using the 4th-order Runge-Kutta (or any other suitable) algorithm. We find $R \approx 3D$ to be sufficiently large.

3. At $r = R$ the solution should be proportional to the Hankel function of the second kind:

$$\hat{p}(R) = H_m^2(\gamma R), \tag{A.3}$$

$$\frac{d\hat{p}}{dr}(R) = \gamma H_{m-1}^2(\gamma R) - \frac{m}{R} H_m^2(\gamma R), \tag{A.4}$$

where $\gamma = \sqrt{w^2 - \alpha^2}$. These relations can only be simultaneously satisfied if

$$G(\alpha) \equiv \left(\hat{p} \frac{dH_m^2}{dr} - \frac{d\hat{p}}{dr} H_m^2 \right)_{r=R} = 0. \tag{A.5}$$

The function $G(\alpha)$ is the dispersion relation and we will use Newton-Rhapson to find its roots. Given $G(\alpha_n)$, we expand $G(\alpha_{n+1})$ in a Taylor series as

$$G(\alpha_{n+1}) = G(\alpha_n) + \left. \frac{dG}{d\alpha} \right|_{\alpha_n} \Delta\alpha + O(\Delta\alpha^2). \tag{A.6}$$

If $G(\alpha_{n+1}) = 0$ (*i.e.*, we found the root) then

$$\alpha_{n+1} = \alpha_n - \left. \frac{G}{dG/d\alpha} \right|_{\alpha_n}. \tag{A.7}$$

We iterate upon this equation until $|\alpha_{n+1} - \alpha_n| < 10^{-9}$. The derivative $dG/d\alpha$ is evaluated by carrying out the α-derivative in equation (A.5). The linear system to be integrated is the enlarged to accommodate the α-derivative of $\hat{p}$.

A.1.2 The Critical Layer

The radial location r^* where $\alpha \overline{u}_x(r^*) - \omega = 0$ is referred to as the critical layer. It is a logarithmic singular point of the inviscid equations (Tam & Morris, 1980). With the inclusion of viscosity the discontinuity is smoothed out but a sharp layer remains. This layer serves as a source of various unstable modes, including a continuous spectrum.

We have to stay clear of this layer in our solution of the Rayleigh equation. We do this by

deforming the path of integration around the branch point as

$$\hat{r}(r) = r - i(\Delta - \mathrm{Im}(r^*) \exp\left(-\frac{(r - \mathrm{Re}(r^*)).^2}{\sigma^2}\right), \tag{A.8}$$

where we chose $\Delta = 0.05$ and $\sigma = 0.1$ (by trial and error).

The critical layer r^* in equation (A.8) depends on the solution $(\alpha, \hat{p})$. The r^*-estimate is thus updated on each pass through the steps in section A.1, and is obtained by the solution of

$$\alpha_n \overline{u}_x(r) - \omega = 0, \tag{A.9}$$

given the guess α_n. Note that this requires evaluating the mean flow $\overline{u}_x$ at complex-valued r. This is no issue when using analytical functions to approximate the mean flow as in equation (3.1). The root r^* can then be determined via the Newton-Rhapson method or any other suitable nonlinear-equation solver. If an analytical approximation is not available, as for the serrated jet, we can also fit a local polynomial to the data and evaluate this at the complex values of r needed. The latter case is ill-behaved as the polynomial-extrapolation off the real-axis is somewhat unpredictable.

Figure A.1 illustrates the solution $\alpha(\omega)$ so obtained, along with $r^*(\omega)$, for an analytical profile. Note that $\mathrm{Im}(\alpha) = \mathrm{Im}(r^*) = 0$ at the same frequency, as expected. Also note that we must always deform the path in the same direction (*i.e.*, we can't start deforming the path into the upper plane when $\mathrm{Im}(r^*)$ passes through zero) so as to remain on the same solution-branch. For very damped waves the deformation can become significant and comparable to the jet diameter. This is the reason why LST computations are terminated at $x/D = 5$ in figure 3.8.

A.1.3 The Serrated Jet

The shooting procedure for the serrated jet shares many similarities with that of the round jet, described in section A.1.

The essential difference is that α (in the spatial approach) is not the only unknown; the pressure amplitudes at the boundaries are unknown as well. For the round nozzle this is immaterial as the

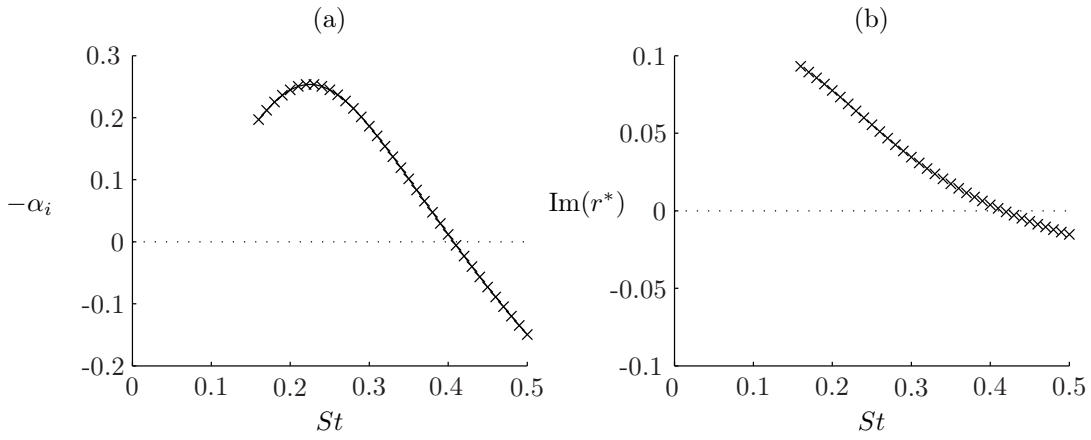

Figure A.1: (a) The growth rate $-\alpha_i$ and (b) imaginary-part of the critical layer r^* for the $M_\infty = 0.5$ jet at $x/D = 3.5$.

(one) governing equation is homogeneous. The boundary conditions for the serrated jet are the same as for the round jet, as there is no coupling far away from the shear layer, as well as near the axis. However, even if the individual modes in the Rayleigh-system (4.15) are homogeneous and uncoupled in the two radial extremes, their relative complex-valued pressure amplitudes are not arbitrary and are determined by their interaction within the shear layer. One of these amplitudes is arbitrary, as the system is homogeneous. For a system of size $2N + 1$ (where N is the summation limit in system (4.15)), we thus have $2N + 1$ unknowns; the $2N$ complex-amplitudes and the eigenvalue.

We enlarge the system to be integrated by creating the variable $\hat{p}_{2N+2} = \alpha$ and setting $d\hat{p}_{2N+2}/dr = 0$. We now supply a guess for the $2N$ relative pressure values along with the eigenvalue and put these values into a vector $\mathbf{v}$, say. This gives us a full set of initial conditions to start the integration. Once we reach the other boundary, we define a vector-valued function $\mathbf{G}(\mathbf{v})$ of size $2N + 1$, that is to be zeroed. Expanding in Taylor series,

$$\mathbf{G}(\mathbf{v} + \delta\mathbf{v}) = \mathbf{G}(\mathbf{v}) + J\delta\mathbf{v} + O(\delta\mathbf{v}^2), \tag{A.10}$$

where

$$J_{ij} = \frac{\partial \mathbf{G}_i}{\partial \mathbf{v}_j}. \tag{A.11}$$

Assuming $\mathbf{G}(\mathbf{v}+\delta\mathbf{v})=0$ (as if the root has been found), we solve

$$J\delta\mathbf{v} = -\mathbf{G}, \tag{A.12}$$

for $\delta\mathbf{v}$, and update $\mathbf{v}$ according to

$$\mathbf{v}^{n+1} = \mathbf{v}^n + \delta\mathbf{v}, \tag{A.13}$$

and iterate until convergence has been obtained.

The algorithm, in summary:

1. Guess values for $2N+1$ vector $\mathbf{v}$

2. Generate pressure/derivative values using boundary conditions:

$$\hat{p}_n(\epsilon) = J_n(\beta\epsilon) \tag{A.14}$$

$$\frac{d\hat{p}_n}{dr}(\epsilon) = \beta J_{m-1}(\epsilon) - \frac{m}{\epsilon}J_n(\beta\epsilon) \tag{A.15}$$

where $\beta = \sqrt{\overline{\rho}(M_\infty\,\alpha-\omega)^2-\alpha^2}$. We normalize these by their respective guess-values in $\mathbf{v}$:

$$\hat{p}_n(\epsilon) = \mathbf{v}_n \tag{A.16}$$

$$\frac{d\hat{p}_n}{dr}(\epsilon) = \mathbf{v}_n\left(\beta J_{m-1}(\epsilon) - \frac{m}{\epsilon}J_n(\beta\epsilon)\right)/J_n(\beta\epsilon), \tag{A.17}$$

and the extra variable is $\hat{p}_{2N+2} = \alpha = \mathbf{v}_{2N+1}$.

3. Integrate through jet towards $r = R$.

4. Construct vector $\mathbf{G}(\mathbf{v})$ (denote analytical boundary conditions by A):

$$\mathbf{G}_n = \hat{p}_n\frac{dA_n}{dr} - \frac{d\hat{p}_n}{dr}A_n, \quad n=1,\ldots,2N+1 \tag{A.18}$$

(A.19)

5. Calculate partial derivatives of $\mathbf{G}$:

$$J_{ij} = \frac{\partial \mathbf{G}_i}{\partial \mathbf{v}_j} = \frac{\mathbf{G}_i(\mathbf{v}_1, .., \mathbf{v}_j + \delta, \ldots, \mathbf{v}_{2N+1}) - \mathbf{G}_i(\mathbf{v}_1, .., \mathbf{v}_j, \ldots, \mathbf{v}_{2N+1})}{\delta}, \tag{A.20}$$

   where $\mathbf{G}_i(\mathbf{v}_1, .., \mathbf{v}_j + \delta, \ldots, \mathbf{v}_{2N+1})$ has to be calculated by integrating again (going through point 1-4).

6. Solve $J\delta\mathbf{v} = -\mathbf{G}$, and calculate $\mathbf{v}^{n+1} = \mathbf{v}^n + \delta\mathbf{v}$.

7. Go to 1 until converged.

A.2 The Direct Solution

Here we rearrange the Rayleigh equation (round: equation (2.50); serrated: equation (4.15)) to form the generalized nonlinear and cubic eigenvalue problem

$$(f_3\alpha^3 + f_2\alpha^2 + f_1\alpha^1 + f_0)\hat{p} = 0, \tag{A.21}$$

where the coefficients f_j for the two jets are given in the next sections.

We discretize equation (A.21) using Chebyshev-polynomials, with the same boundary conditions as before (equations (2.52) and (2.53). This results in the discreet version of the problem above:

$$(F_3\alpha^3 + F_2\alpha^2 + F_1\alpha^1 + F_0)p = 0, \tag{A.22}$$

where the F_j are matrices. To linearize the problem we rearrange it as follows:

$$\begin{bmatrix} 0 & I & 0 \\ 0 & 0 & I \\ -F_0 & -F_1 & -F_2 \end{bmatrix} \begin{bmatrix} p \\ \alpha p \\ \alpha^2 p \end{bmatrix} = \alpha \begin{bmatrix} 0 & I & 0 \\ 0 & 0 & I \\ 0 & 0 & F_3 \end{bmatrix} \begin{bmatrix} p \\ \alpha p \\ \alpha^2 p \end{bmatrix}, \tag{A.23}$$

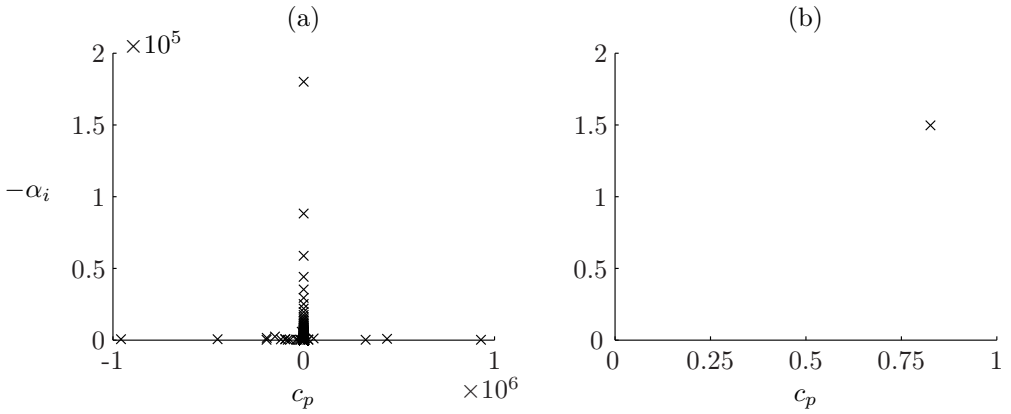

Figure A.2: (a) The unfiltered and (b) filtered eigenvalue spectra $\alpha = \alpha_r + i\alpha_i$ (abscissa shows phase-speed $c_p = \omega/\alpha_r$) for the cold $M_\infty = 0.9$ round jet at $x/D = 0.5$, $m = 0$ and $St = 0.35$.

or

$$Aq = \alpha Bq. \tag{A.24}$$

These matrices are singular where the mean flow $\overline{u}_x$ vanishes and so will have very large-amplitude (infinite, in theory) eigenvalues. This is illustrated in figure A.2 (a). To pick the physical eigenvalues out of the full spectra we examine the respective eigenvectors, accepting those that have the appropriate far-field behavior. The physical eigenvalues are shown in figure A.2 (b), where only a single unstable mode is found. This is appropriate as this test is for a round jet with a single inflection point.

A.2.1 The Round Jet

The coefficients f_j for the round jet follow:

$$f_3 = (\overline{\rho u}_x^2 - 1)\overline{u}_x, \tag{A.25}$$

$$f_2 = -(3\overline{\rho u}_x^2 - 1)\omega, \tag{A.26}$$

$$f_1 = \left(-\frac{d^2}{dr^2} - \left(\frac{1}{r} - \frac{\partial_r \overline{\rho}}{\overline{\rho}}\right)\frac{d}{dr} + \frac{m^2}{r^2} - \overline{\rho}\omega^2\right)\omega, \tag{A.27}$$

$$f_0 = \overline{u}_x \frac{d^2}{dr^2} + \left(\frac{\overline{u}_x}{r} - 2\partial_r \overline{u}_x - \overline{u}_x \frac{\partial_r \overline{\rho}}{\overline{\rho}}\right)\frac{d}{dr} - \left(\frac{m^2}{r^2} - 3\overline{\rho}\omega^2\right)\overline{u}_x. \tag{A.28}$$

A.2.2 The Serrated Jet

The coefficients f_j for the serrated jet follow. Note that these are given in (r, θ)-space:

$$f_3 = (\overline{\rho u}_x^2 - 1)\overline{u}_x, \tag{A.29}$$

$$f_2 = -(3\overline{\rho u}_x^2 - 1)\omega, \tag{A.30}$$

$$f_1 = \overline{u}_x \left(\frac{\partial^2}{\partial r^2} + \frac{1}{r^2}\frac{\partial^2}{\partial \theta^2} \right) - \left(2\partial_r \overline{u}_x + \overline{u}_x \left(\frac{1}{r} + \frac{\partial_r \overline{\rho}}{\overline{\rho}} \right) \right) \frac{\partial}{\partial r} \tag{A.31}$$

$$- \frac{1}{r^2} \left(2\partial_\theta \overline{u}_x + \overline{u}_x \frac{\partial_\theta \overline{\rho}}{\overline{\rho}} \right) \frac{\partial}{\partial \theta} + 3\overline{\rho}\omega^2 \overline{u}_x, \tag{A.32}$$

$$f_0 = -\left(-\frac{\partial^2}{\partial r^2} + \frac{1}{r^2}\frac{\partial^2}{\partial \theta^2} + \left(\frac{1}{r} - \frac{\partial_r \overline{\rho}}{\overline{\rho}} \right) \frac{\partial}{\partial r} - \frac{1}{r^2}\frac{\partial_\theta \overline{\rho}}{\overline{\rho}}\frac{\partial}{\partial \theta} \right) \omega - \overline{\rho}\omega^3. \tag{A.33}$$

Appendix B

The PSE Operators

Here we give the forms of the operators **A** through **E** in equation (2.60), repeated here:

$$\left(\mathbf{A}(\overline{\mathbf{q}},\alpha,\omega)+\mathbf{B}(\overline{\mathbf{q}})\right)\,\hat{\mathbf{q}}+\mathbf{C}(\overline{\mathbf{q}})\,\frac{\partial\hat{\mathbf{q}}}{\partial x}+\mathbf{D}(\overline{\mathbf{q}})\,\frac{\partial\hat{\mathbf{q}}}{\partial r}=\frac{1}{Re}\mathbf{E}(\overline{\mathbf{q}})\,\hat{\mathbf{q}}, \tag{B.1}$$

where α and ω respectively denote streamwise wavenumber/growth-rate and frequency, and $\overline{\mathbf{q}}$ is the mean flow, given by

$$\overline{\mathbf{q}}(\mathbf{x})=(\overline{u}_x(x,r),\overline{u}_r(x,r),0,\overline{\rho}(x,r),\overline{T}(x,r)). \tag{B.2}$$

For notational convenience, let us make the following definitions:

1. $\overline{u}=\overline{u}_x$, and $\overline{v}=\overline{u}_r$. Spatial derivatives in x and r are then denoted by a subscript, $\overline{u}_x=\partial_x\overline{u}$, $\overline{u}_r=\partial_r\overline{u}$, and so forth.

2. $\beta=\alpha\overline{u}-\omega$.

B.1 Operator A

$$\mathbf{A}=\begin{bmatrix}
\overline{\rho}\,\overline{u}_x & \overline{\rho}\,\overline{u}_r & 0 & 0 & 0\\
\overline{\rho}\,\overline{v}_x & \overline{\rho}\,\overline{v}_r & 0 & \overline{\rho}_r\,(\gamma-1)/\gamma & \overline{T}_r\,(\gamma-1)/\gamma\\
0 & 0 & \overline{\rho}\,\overline{v}/r & 0 & 0\\
\overline{\rho}\,\overline{T}_x & \overline{\rho}\,\overline{T}_r+1/r & 0 & \overline{\rho}(\gamma-1)(\overline{u}_x+\overline{v}_r+\overline{v}/r) & 0\\
\overline{\rho}_x & \overline{\rho}_r+\overline{\rho}/r & 0 & 0 & \overline{u}_x+\overline{v}_r+\overline{v}/r
\end{bmatrix} \tag{B.3}$$

B.2 Operator B

$$\mathbf{B} = \begin{bmatrix} i\overline{\rho}\,\beta & 0 & 0 & i\alpha\overline{\rho}\,(\gamma-1)/\gamma & i\alpha\overline{T}\,(\gamma-1)/\gamma \\ 0 & i\overline{\rho}\,\beta & 0 & 0 & \\ 0 & 0 & i\overline{\rho}\,\beta & im\overline{\rho}(\gamma-1)/\gamma & im\overline{T}(\gamma-1)/\gamma \\ i\alpha & 0 & im/r & i\overline{\rho}\,\beta & 0 \\ i\alpha\,\overline{\rho} & 0 & im\overline{\rho}\,/r & 0 & i\beta \end{bmatrix} \tag{B.4}$$

B.3 Operator C

$$\mathbf{C} = \begin{bmatrix} \overline{\rho}\,\overline{u} & 0 & 0 & 0 & 0 \\ 0 & \overline{\rho}\,\overline{u} & 0 & 0 & 0 \\ 0 & 0 & \overline{\rho}\,\overline{u} & 0 & 0 \\ 1 & 0 & 0 & \overline{\rho}\,\overline{u} & 0 \\ \overline{\rho} & 0 & 0 & 0 & \overline{u} \end{bmatrix} \tag{B.5}$$

B.4 Operator D

$$\mathbf{D} = \begin{bmatrix} \overline{\rho}\,\overline{v} & 0 & 0 & 0 & 0 \\ 0 & \overline{\rho}\,\overline{v} & 0 & \overline{\rho}\,(\gamma-1)/\gamma & \overline{\rho}\,(\gamma-1)/\gamma \\ 0 & 0 & \overline{\rho}\,\overline{v} & 0 & 0 \\ 0 & 1 & 0 & \overline{\rho}\,\overline{v} & 0 \\ 0 & \overline{\rho} & 0 & 0 & \overline{v} \end{bmatrix} \tag{B.6}$$

B.5 Operator E

The operator $\mathbf{E}$ is decomposed as

$$\mathbf{E} = \mathbf{E}_2 \frac{d^2}{dr^2} + \mathbf{E_1} \frac{d}{dr} + \mathbf{E_0}, \tag{B.7}$$

where, in addition to linearization we have applied the thin-shear layer approximation (retain only diagonal terms in the shear-stress).

$$\mathbf{E_2} = M_\infty \begin{bmatrix} 1 & 0 & 0 & 0 & 0 \\ 0 & 2/3 & 0 & 0 & \\ 0 & 0 & 1 & 0 & 0 \\ 0 & 0 & 0 & \gamma/(M_\infty Pr) & 0 \\ 0 & 0 & 0 & 0 & 0 \end{bmatrix}, \tag{B.8}$$

$$\mathbf{E_1} = M_\infty \begin{bmatrix} 1/r & 0 & 0 & 0 & 0 \\ 0 & 2/(3r) & 0 & 0 & \\ 0 & 0 & 0 & 0 & 0 \\ 2\gamma\overline{u}_r & 4\gamma(2\overline{v}_r/3 - \overline{v}/(6r)) & 0 & 0 & \gamma/(rM_\infty Pr) \\ 0 & 0 & 0 & 0 & 0 \end{bmatrix}, \tag{B.9}$$

and

$$\mathbf{E_0} = M_\infty \begin{bmatrix} 0 & 0 & 0 & 0 & 0 \\ 0 & 0 & 0 & 0 & 0 \\ 0 & 0 & 0 & 0 & 0 \\ 0 & -2M_\infty\gamma/(3r)\overline{v}_r & 0 & 0 & 0 \\ 0 & 0 & 0 & 0 & 0 \end{bmatrix}. \tag{B.10}$$

Bibliography

Alkislar, M. B., Krothapalli, A. & Butler, G. 2007 The effect of streamwise vortices on the aeroacoustics of a Mach 0.9 jet. *J. Fluid Mech.* **578**, 139–169.

Balakumar, P. 1998 Prediction of supersonic jet noise. *AIAA* (Paper 1998-1057).

Balasubramanian, K. & Sujith, R.I. 2008 Thermoacoustic instability in a Rijke tube: Non-normality and nonlinearity. *Phys. Fluids* **20**, 044103.

Batchelor, G. K. & Gill, A. E. 1962 Analysis of the stability of axisymmetric jets. *J. Fluid Mech.* **14(4)**, 529–551.

Bertolotti, F. P. & Herbert, T. 1991 Analysis of the Linear Stability of Compressible Boundary Layers using the PSE. *Theoret. Comput. Fluid Dyn.* **3**, 117–124.

Bertolotti, F. P., Herbert, T. & Spalart, P. R. 1992 Linear and Nonlinear Stability of the Blasius Boundary Layer. *J. Fluid Mech.* **242**, 441–474.

Bodony, D.J. & Lele, S.K. 2008 Current status of jet noise predictions using large-eddy simulation. *AIAA J.* **46** (2), 364.

Bodony, D. J. & Lele, S. K. 2005 Using large eddy simulation for jet noise prediction. *Phys. Fluids* **17**.

Bohl, D. G. & Foss, J.F. 1999 Near exit plane effects caused by primary and primary-plus secondary tabs. *AIAA J.* **37(2)**.

Bradbury, L. J. S. & Khadem, A. H. 1975 The distortion of a jet by tabs. *J. Fluid Mech.* **70(4)**, 801–813.

Bridges, J. & Brown, C. A. 2004 Parametric testing of chevrons on single flow hot jets. *AIAA* (Paper 2004-2824).

Bridges, J. & Hussain, F. 1992 Direct evaluation of aeroacoustic theory in a jet. *J. Fluid Mech.* **240**, 469–501.

Bridges, J. & Hussain, F. 1995 Effects of nozzle body on jet noise. *J. Sound Vib.* **188** (3), 407–418.

Bridges, J. & Wernet, M.P. 2003 Measurements of the aeroacoustic sound source in hot jets. *AIAA* (Paper 2003-3130).

Brown, G.L. & Roshko, A. 1974 On density effects and large structure in turbulent mixing layers. *J. Fluid Mech.* **64** (04), 775–816.

Callender, B., Gutmark, E. & Martens, S. 2005 Far-field acoustic investigation into chevron nozzle mechanisms and trends. *AIAA J.* **43(1)**, 87–95.

Chang, C. L., Malik, M. R., Erlebacher, G. & Hussaini, M. Y. 1993 Linear and Nonlinear PSE For Compressible Boundary Layers. *Tech. Rep.* ICASE 93-70.

Cheung, L.C. & Lele, S.K. 2009 Linear and nonlinear processes in two-dimensional mixing layer dynamics and sound radiation. *J. Fluid Mech.* **625**.

Colonius, T. & Lele, S.K. 2004 Computational aeroacoustics: progress on nonlinear problems of sound generation. *Prog. Aerospace Sci.* **40**, 345–416.

Crighton, D.G. 1972 The excess noise field of subsonic jets. *J. Fluid Mech.* **56**, 663–694.

Crighton, D.G. 1975 Basic principles of aerodynamic noise generation. *Prog. Aerospace Sci.* **16**, 31–96.

Crighton, DG & Gaster, M. 1976 Stability of slowly diverging jet flow. *J. Fluid Mech.* **77**, 397–413.

Crighton, D.G. & Huerre, P. 1990 Shear-layer pressure fluctuations and superdirective acoustic sources. *J. Fluid Mech.* **220**, 355–368.

Crow, S.C. & Champagne, F.H. 1971 Orderly structure in jet turbulence. *J. Fluid Mech.* **48** (3), 547–591.

Day, MJ, Mansour, NN & Reynolds, WC 2001 Nonlinear stability and structure of compressible reacting mixing layers. *J. Fluid Mech.* **446**, 375–408.

Drazin, P.G. & Reid, W.H. 1969 *Hydrodynamic Stability*. Cambridge University Press.

Ffowcs-Williams, J.E. 1963 The noise from turbulence convected at high speed. *Proc. R. Soc. Lond. A.* pp. 469–503.

Ffowcs-Williams, J.E. 1977 Aeroacoustics. *Annu. Rev. Fluid Mech.* **9** (1), 447–468.

Foss, J.K. & Zaman, K. B. M. Q. 1999 Large- and small-scale vortical motions in a shear layer perturbed by tabs. *J. Fluid Mech.* **382**, 307–329.

George, W.K., Beuther, P.D. & Arndt, R.E.A. 1984 Pressure spectra in turbulent free shear flows. *J. Fluid Mech.* **148**, 155–191.

Goldstein, M.E. 1984 Aeroacoustics of turbulent shear flows. *Annu. Rev. Fluid Mech.* **16** (1), 263–285.

Goldstein, M.E. 2003 A generalized acoustic analogy. *J. Fluid Mech.* **488**, 315–333.

Gudmundsson, K. & Colonius, T. 2009 Parabolized Stability Equation Models for Turbulent Jets and Their Radiated Sound. *AIAA* (Paper 2009-3380).

Gudmundsson, K. & Colonius, T. 2010*a* Instability Wave Models for the Near Field Fluctuations of Turbulent Jets. *J. Fluid Mech.* (in preparation).

Gudmundsson, K. & Colonius, T. 2010*b* The Effects of Nozzle Serrations on the Linear Stability of Turbulent Jets. *J. Fluid Mech.* (in preparation).

Herbert, T. 1994 Parabolized stability equations. *Tech. Rep.* AGARD-R-793. Von Karman Institute.

Ho, C.M. & Huerre, P. 1984 Perturbed free shear layers. *Annu. Rev. Fluid Mech.* **16** (1), 365–422.

Huerre, P. & Monkewitz, P. A. 1990 Local and global instabilities in spatially developing flows. *Annu. Rev. Fluid Mech.* **22**, 437–537.

Hussain, A.K.M.F. & Reynolds, W.C. 1970 The mechanics of an organized wave in turbulent shear flow. *J. Fluid Mech.* **41** (2), 241–258.

Hussain, A. K. M. F. 1983 Coherent structures—reality and myth. *Phys. Fluids* **26**, 2816–2850.

Hussain, F. 1986 Coherent structures and turbulence. *J. Fluid Mech.* **173**, 303–356.

Kawahara, G., Jimenez, J., Uhlmann, M. & Pinelli, A. 2003 Linear instability of a corrugated vortex sheet–a model for streak instability. *J. Fluid Mech.* **483**, 315–342.

Laufer, J. & Yen, T.A.C. 1983 Noise generation by a low-Mach-number jet. *J. Fluid Mech.* **134**, 1–31.

Lesshafft, L. & Huerre, P. 2007 Linear impulse response in hot round jets. *Phys. Fluids* **19**, 024102.

Li, F. & Malik, M. R. 1996 On the nature of the pse approximation. *Theoret. Comput. Fluid Dyn.* **8**, 253–273.

Li, F. & Malik, M. R. 1997 Spectral Analysis of Parabolized Stability Equations. *Computers and Fluids* **3**, 279–297.

Lighthill, M.J. 1952 On sound generated aerodynamically. I. General theory. *Proc. R. Soc. Lond. A.* **211** (1107), 564–587.

Lighthill, M.J. 1954 On sound generated aerodynamically. II. Turbulence as a source of sound. *Proc. R. Soc. Lond. A.* **222** (1148), 1–32.

Lilley, G.M. 1974 On the noise from jets. *AGARD CP-131* pp. 13–1.

Lilley, G.M. 1991 Jet noise classical theory and experiments. In *NASA. Langley Research Center, Aeroacoustics of Flight Vehicles: Theory and Practice. Volume 1: Noise Sources p 211-289 (SEE N92-10598 01-71)*, , vol. 1, pp. 211–289.

Lumley, J.L. 1967 The structure of inhomogeneous turbulent flows. *Atmospheric turbulence and radio wave propagation* pp. 166–178.

Malik, M .R. & Chang, C. L. 2000 Nonparallel and nonlinear stability of supersonic jet flow. *Computers and Fluids* **29**, 327–365.

Mankbadi, R. & Liu, J. T. C. 1981 A study of the interactions between large-scale coherent structures and fine-grained turbulence in a round jet. *Proc. Roy. Soc. London* **1443**, 541–602.

Mattingly, G. E. & Chang, C. C. 1974 Unstable waves on an axisymmetric jet column. *J. Fluid Mech.* **63(3)**, 541–560.

Möhring, W. 1978 On vortex sound at low Mach number. *J. Fluid Mech.* **85** (4), 685–691.

Mohseni, K., Colonius, T. & Freund, J.B. 2002 An evaluation of linear instability waves as sources of sound in a supersonic turbulent jet. *Phys. Fluids* **14**, 3593.

Mollo-Christensen, E. 1967 Jet noise and shear flow instability seen from an experimenter's viewpoint(similarity laws for jet noise and shear flow instability as suggested by experiments). *J. Applied Mech.* **89**.

Monkewitz, P. & Sohn, K. 1988 Absolute instability in hot jets. *AIAA journal* **26** (8), 911–916.

Moore, C.J. 1977 The role of shear-layer instability waves in jet exhaust noise. *J. Fluid Mech.* **80**, 321–367.

Petersen, R. A. & Samet, M. M. 1988 On the preferred mode of jet instability. *J. Fluid Mech.* **194**, 153–173.

Ray, P.K., Cheung, L.C. & Lele, S.K. 2009 On the growth and propagation of linear instability waves in compressible turbulent jets. *Physics of Fluids* **21**, 054106.

Reba, R., Narayanan, S. & Colonius, T. 2010 Wave-packet models for large-scale mixing noise. *Int. J. Aeroacoustics* (accepted for publication).

Reeder, M. F. & Samimy, M. 1996 The evolution of a jet with vortex-generating tabs: real-time visualization and quantitative measurements. *J. Fluid Mech.* **311**, 73–118.

Reynolds, A.J. 1962 Observations of a liquid-into-liquid jet. *J. Fluid Mech.* **14** (4), 552–556.

Rowley, C.W., Colonius, T. & Basu, A.J. 2002 On self-sustained oscillations in two-dimensional compressible flow over rectangular cavities. *J. Fluid Mech.* **455**, 315–346.

Suzuki, T. & Colonius, T. 2006 Instability waves in a subsonic round jet detected using a near-field phased microphone array. *J. Fluid Mech.* **565**, 197–226.

Tam, C.K.W. 1995 Supersonic jet noise. *Annu. Rev. Fluid Mech.* **27** (1), 17–43.

Tam, C.K.W. 1998 Jet noise: since 1952. *Theoret. and Comput. Fluid Dyn.* **10** (1), 393–405.

Tam, C.K.W. & Burton, D.E. 1984 Sound generated by instability waves of supersonic flows. Part 2. Axisymmetric jets. *J. Fluid Mech.* **138**, 273–295.

Tam, C.K.W., Golebiowski, M. & Seiner, JM 1996 On the two components of turbulent mixing noise from supersonic jets. *AIAA* (Paper 1996-1716).

Tam, C.K.W. & Morris, P.J. 1980 The radiation of sound by the instability waves of a compressible plane turbulent shear layer. *J. Fluid Mech.* **98** (Pt 2), 349–381.

Tanna, H.K. 1977 An experimental study of jet noise. Part I: Turbulent mixing noise. *J. Sound Vib.* **50** (3), 405–428.

Thompson, K.W. 1987 Time dependent boundary conditions for hyperbolic systems. *J. Comp. Phys.* **68**, 1–24.

Tinney, C.E. & Jordan, P. 2008 The near pressure field of co-axial subsonic jets. *J. Fluid Mech.* **611**, 175–204.

Troutt, T.R. & McLaughlin, D.K., D.K. 1982 Experiments on the flow and acoustic properties of a moderate reynolds number supersonic jet. *J. Fluid Mech.* **116**, 123–156.

Wang, M., Freund, J.B. & Lele, S.K. 2006 Computational prediction of flow-generated sound. *Annu. Rev. Fuid Mech.* **38**, 483–512.

Widnall, S.E. & Tsai, C.Y. 1977 The instability of the thin vortex ring of constant vorticity. *Phil. Trans. Roy. Soc. Lond. A* **287** (1344), 273–305.

Winant, C.D. & Browand, F.K. 1974 Vortex pairing: The mechanism of turbulent mixing-layer growth at moderate Reynolds number. *J. Fluid Mech.* **63** (2), 237–255.

Yen, C. C. & Messersmith, N. L. 1998 Application of parabolized stability equations to prediction of jet instabilities. *AIAA J.* **36**, 1541–1544.

Zaman, K. B. M. Q., Reeder, M. F. & Hussain, A. K. M. F. 1980 Vortex pairing in a circular jet under controlled excitation. Part 1. General jet response. *J. Fluid Mech.* **101(3)**, 449–491.

Zaman, K. B. M. Q., Reeder, M. F. & Samimy, M. 1993 Control of an axisymmetric jet using vortex generators. *Phys. Fluids* **6(2)**, 778–793.